Wesleyan University Physics Department

Experimental Studies of a UHF Driven PT Dimer

by

Mahboobeh Chitsazi

Faculty Advisor: Prof. Fred M. Ellis

A dissertation submitted to the
faculty of Wesleyan University
in partial fulfillment of the requirements for the
Degree of Doctor in Philosophy in Physics

Middletown, Connecticut August, 2018

To Masoud

For his advice, his patience, and his love.

Acknowledgment

I am so grateful for the opportunity to be able to express my thanks to some of the people who have touched my life and who have helped me along the way.

I’d like to begin by acknowledging my advisor and my mentor, professor Fred M. Ellis. Thank you for teaching me almost everything I know from Electronics and more importantly for teaching me how to be a better human being. Thanks for your immense knowledge, patience, continuous support and for always believing in me.

I would also like to thank the faculty of Physics department at Wesleyan University for their support over the past five years, especially my dissertation committee members; Prof. Tsampikos Kottos and Prof. Greg Voth; thank you for all your helpful comments and guidance. My gratitude also goes to two wonderful people at Wesleyan University’s graduate office, Cheryl Hagner and Barbara Schukoske.

Many thanks goes to my friends Nadeepa, Nooshin, Neda, Hamid, Hamed, Bonnie, Eleana, Stefan, Savannah, Ali, William, Wengang, Nimesh, and Nam who filled this five years with a lot of joy and good memories. Thank you for making it so wonderful. Especial thanks to my friends and labmates Joseph and Cameron for making working in the lab so much fun.

Last but not least, I would like to thank my family; My mom and dad, for their support and limitless love. My brothers, for always being there for me. And my wonderful sister Maryam, who gave me dreams to look forward to it; thanks for reading all those books before me and for being the inspiration of my life.

Contents

List of Figures

Chapter 0

Introduction

In 2010, a collaboration between professor Ellis and professor Kottos groups was started on studying one specific class of Non-Hermitian Hamiltonians known as Parity-Time (PT) symmetric systems in electronics framework. The first PT electronics system at frequency of 30 kHz was developed and studied during the same year [1]. The collaboration which was initiated for the purpose of fundamentally studying systems with PT symmetric Hamiltonians, later took a different course and continued in a more general and technological way to develop and study Non-Hermitian systems (not necessarily PT) and their applications.

Over the past several years, beside producing many publications [1-8], our group has developed several different apparatuses with a few big jumps in frequency. The two biggest jumps of frequencies are going 100 times larger from 30 kHz to 3 MHz, and then from 3 MHz to 300 MHz. My project, with the goal of design and developing an ultra high frequency PT electronics system, was started in 2014.

Non-Hermitian Hamiltonians H which commute with the PT symmetry operator might have a real spectrum depending on the parameter γ which controls the degree of Non-Hermiticity. For γs below the critical value γ_{PT}, the spectrum of the system is completely real. This parameter domain is termed as the exact PT phase regime. If the degree of Non-Hermiticity is above γ_{PT}, the spectrum of the system will be complex. This domain is known as the broken phase regime [9].

Physically, the simplest system with a PT symmetric Hamiltonian is a system consisting of two identical coupled oscillators which are located at different positions, one with gain and the other with the exact amount of dissipation. In electronics, a combination of two LC oscillators coupled capacitively or inductively, one with active conductance and the other with negative conductance, creates a circuit version of a PT system [10].

PT-symmetric systems have been studied in different areas of physics including mathematical physics and quantum field theories [9, 11, 12], optics [13-21], atomic [22], and solid state [23, 24]. PT-synthetic materials can show some intriguing properties. In such systems loss creates another degree of freedom whose manipulation results in very interesting and non-conventional properties. Examples of these properties include unidirectional invisibility [21], power oscillations and nonreciprocity of light propagation [13, 15, 17], absorption-enhanced transmission [14], loss-induced transparency [14], perfect absorbers [25, 26], chiral-symmetric lasers [27, 28], and hypersensitive sensors [29-32]. A new generation of on-chip isolators and circulators can be designed by considering these nonreciprocal effects in the nonlinear domain [16]. The realization of coherent perfect absorbers-lasers [20], and nonlinear switching structures [19], and the study of Bloch oscillations [18] are a few examples of advances in PT optics.

Active electronic circuits provide a conceptually simpler and experimentally more accessible framework to study PT symmetric systems. Various new concepts in PT-symmetric wave transport were initially experimented and demonstrated in this framework, including eigenmode analysis, PT-symmetric scattering in both the linear and nonlinear regime, and spatiotemporal dynamics of the stored energy in static circuit. Besides these advantages, the integrated circuitry architectures provided by the PT-circuitry approach affords novel avenues for reduced circuit loss and signal manipulation. Furthermore, it facilitates a direct link with recent technological problems in (nano)antenna theory and split-ring resonator metamaterial arrays.

Traditionally, the study and application of PT-symmetric systems have been focused on static (time-independent) potentials. Recently, however, time-dependent PT-symmetric systems have attracted a lot of attention [23, 24, 33-36] for two reasons. The first reason is fundamental. It is expected that new pathways in the PT research can lead to new exciting phenomena. Similarly, investigation of time-dependent Hermitian counterparts led to a surge in novel phenomena like dynamical localization [37], dynamical Anderson localization [38], and coherent destruction of tunneling [39]. The second reason on the other hand is technological. A driving scheme can be potentially used as a flexible experimental knob to realize new forms of reconfigurable synthetic matter [40, 41]. Using periodic driving schemes in PT symmetric systems can allow for the management of the spontaneous PT-symmetry breaking for arbitrary values of the gain and loss parameters. Driving scheme will give us another degree of freedom to control the instability of the system by changing the amplitude or frequency of the drive. Although theoretical studies have been advocating for this scenario, currently there is no experimental realization of a time dependent PT-symmetric setup.

The structure of this thesis is as follows.

The major PhD's research portion of this work consisted of the design and apparatus development of the ultra high frequency driven PT symmetric dimer. This major project is the subject of Chapters 1, 2, 3, and 5. Chapter 1 introduces the experimental set-up and lays the theoretical foundation for studying of the UHF driven PT symmetric dimer where the capacitive coupling between the oscillators is time-dependent. Chapter 2 summarizes the methods and experimental techniques used to acquire the data. Chapter 3 then completes this subject by presenting the experimental results obtained for a periodically driven PT symmetric system.

Chapter 4 presents "Lasing Death" phenomenon in electronics framework. Lasing death (LD) or lasing shutdown was first proposed in the framework of laser physics in [42]. By presenting the experimental system of two 3 MHz coupled RLC circuits with active nonlinear conductances, we demonstrate that amplification action can be tamed via asymmetric pumping. Under specific conditions we observe the counterintuitive phenomenon of stabilization of the system even when the overall gain provided is increased.

Chapter 5 talks about my ongoing project on "Encircling the Exceptional point" . The transition point γ_{PT} shows all the features of an exceptional point (EP) singularity where both eigenfunctions and eigenvalues merge. Its existence played an important role in many PT studies both experimentally and theoretically [43-47]. It is predicted that encircling the EPs can transfer the energy between different modes where this energy transfer is nonreciprocal and is independent of the initial state. This project was started a year ago, on the same experimental set-up as Chapter 1. This chapter reports the latest results as this is a work-in-progress project.

Chapter 1

The UHF Driven PT Symmetric Dimer

This chapter introduces the experimental set-up and lays the theoretical foundation for studying of ultra high frequency (UHF) driven PT symmetric dimer where the capacitive coupling between the oscillators is time dependent, see Figure 1.1b.

1.1 Theoretical consideration

The simplest and conceptually most straight forward PT symmetric system is illustrated in Figure. 1.1a. Two identical simple harmonic oscillators, in the electronic form of LC resonators are coupled capacitively or inductively with balanced gain and loss, which means the non-Hermitian dissipation on the left is paired with its negative resistance counterpart on the right.

Theoretically, for a driven PT symmetric system (Figure 1.1b), the driven capacitive coupling is given as $c = C_c/C = c_0 + \varepsilon \cos(\omega_m \tau)$ where the rescaled time $\tau =$

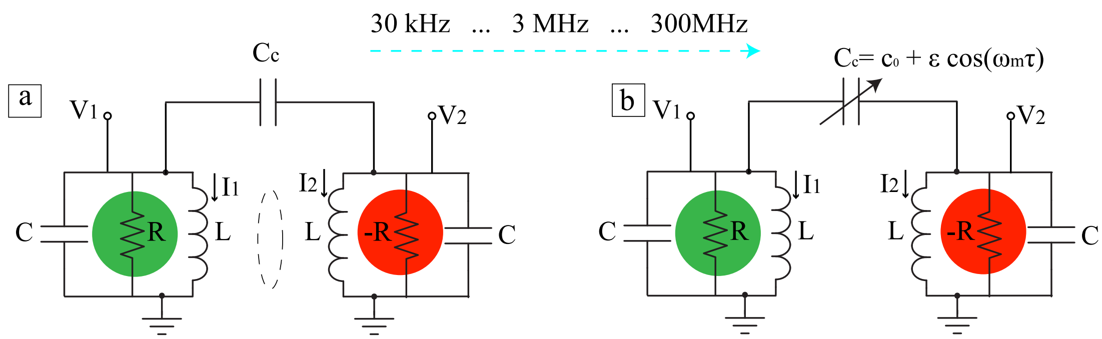

Figure 1.1: (a) Simplified schematic of the PT-symmetric electronic dimer. Both mutual inductance coupling and capacitive coupling are included for generality. (b) schematic of the driven PT-symmetric electronic dimer.

$\omega_0 t$ and $\omega_0 = 1/(LC)^{1/2}$. Using Kirchoff's laws, the dynamics for the voltages V_1 (V_2) of the gain (loss) side of the driven dimer is:

$$\frac{d^2}{d\tau^2}V + A\frac{d}{d\tau}V + BV = 0; \quad V \equiv (V_1, V_2)^T, \tag{1.1}$$

where

$$A = \frac{1}{\beta}\begin{bmatrix} -\gamma(1+c)+2\dot{c} & \gamma c - 2\dot{c} \\ -\gamma c - 2\dot{c} & \gamma(1+c)+2\dot{c} \end{bmatrix}$$
$$B = \frac{1}{\beta}\begin{bmatrix} 1+c+\ddot{c} & c-\ddot{c} \\ c-\ddot{c} & 1+c+\ddot{c} \end{bmatrix}. \tag{1.2}$$

$\beta = 1+2c$ and $\gamma = R^{-1}(L/C)^{1/2}$ are the rescaled gain and loss parameters which control the degree of Non-Hermiticity, and $\dot{c}$ ($\ddot{c}$) denotes the first (second) derivative of the scaled capacitive coupling c with respect to the scaled time. Equation (1.1) is invariant under joint parity P and time T operations, where T performs the operation τ to $-\tau$ and P is the Pauli matrix σ_x.

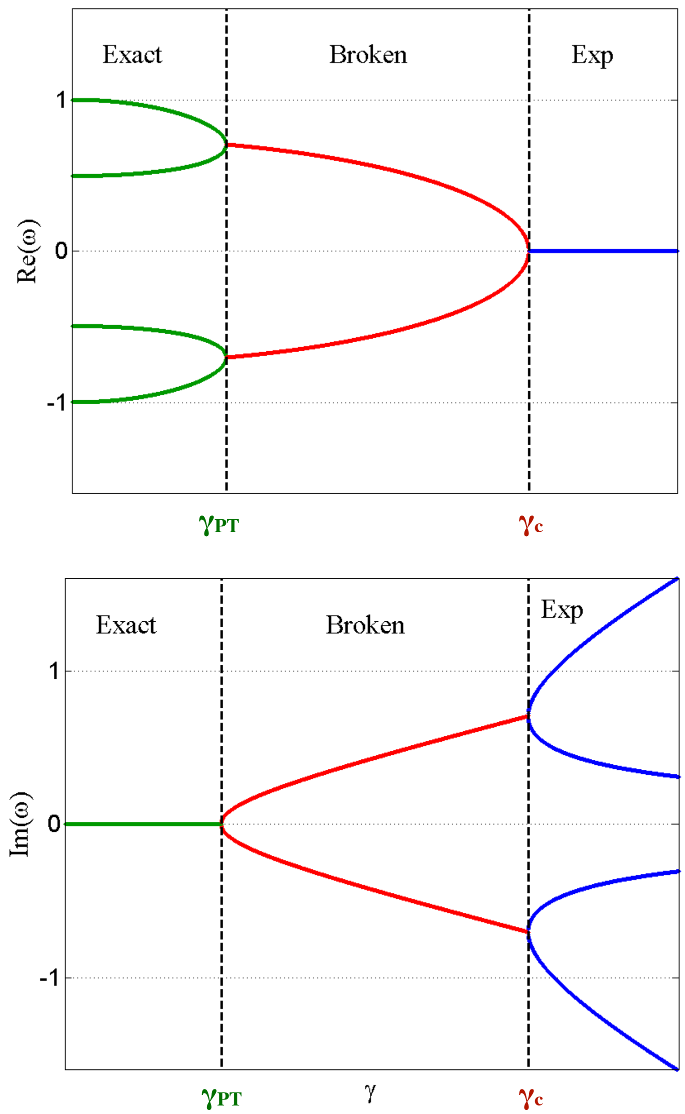

Figure 1.2: The spectrum of a static (undriven) PT symmetric system.

In the absence of driving, *i.e.*, $\varepsilon = 0$, and consequently $\dot{c} = \ddot{c} = 0$, the eigenfrequencies ω_α ($\alpha = 1, 2$) of systems of Equation (1.1) are given as

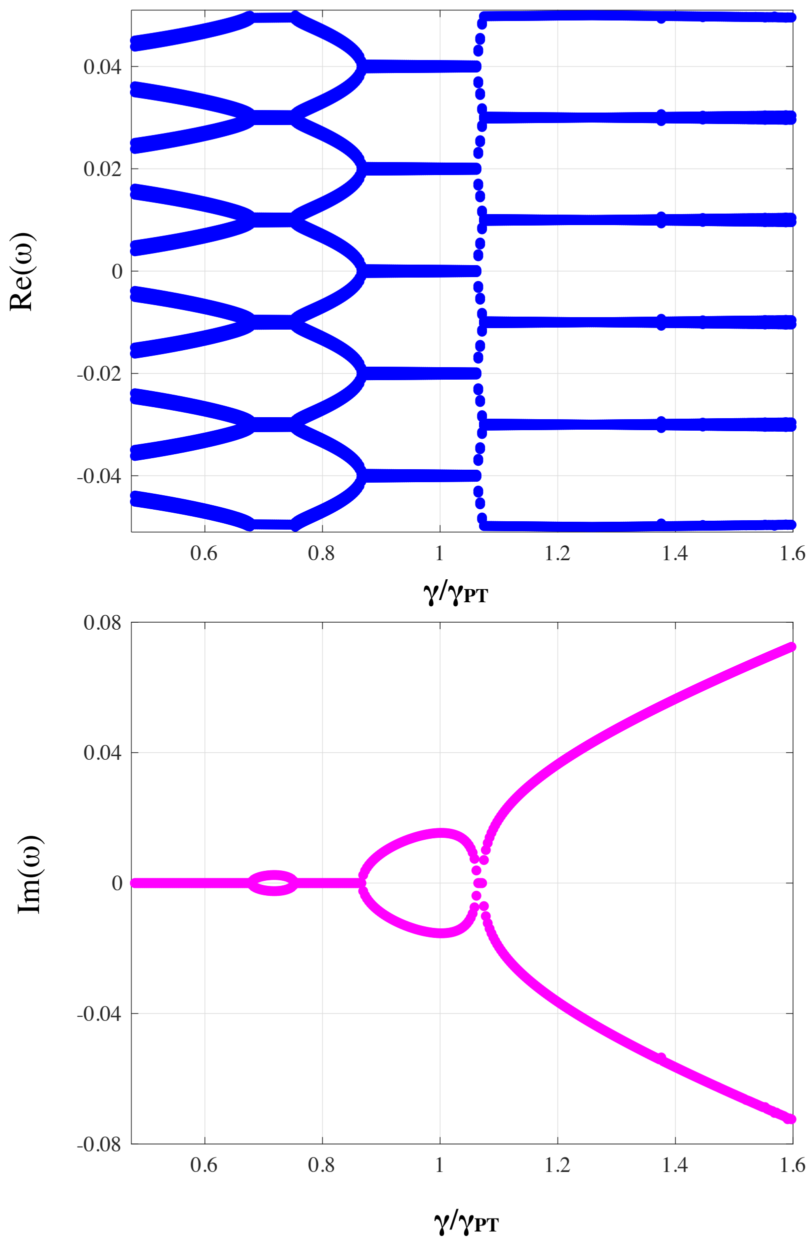

Figure 1.3: (numerical data) The spectrum of the driven PT symmetric system. Driven coupling is given as $c = c_0 + \varepsilon\cos(\omega_m\tau)$. $c_0 = 0.1$, $\varepsilon = 0.01$ and $\omega_m = 0.0198$.

$$\omega_\alpha = \frac{1}{2\sqrt{1+2c_0}}\left(\sqrt{\gamma_c^2-\gamma^2}+(-1)^\alpha\sqrt{\gamma_{PT}^2-\gamma^2}\right)$$

where $\gamma_{PT} = (1 + 2c_0)^{1/2} - 1$ for the spontaneous PT-symmetry breaking point and $\gamma_c = (1 + 2c_0)^{1/2} + 1$ for the upper critical point. Both of these points are determined by the strength of the (capacitance) coupling c_0 between the two elements of the dimer.

The spectrum of the undriven dimer is divided into two domains of exact ($\gamma < \gamma_{PT}$) and broken ($\gamma > \gamma_{PT}$) *PT*-symmetry phase (Figure 1.2). For γs below the critical value γ_{PT}, the spectrum of the system is completely real. This parameter domain is termed as the exact PT phase regime. For γs above γ_{PT} and below γ_c, the spectrum of the system will be complex with one real and non-zero imaginary parts. This domain is known as the broken phase regime. For γs above γ_c, the spectrum of the system will be completely imaginary.

To study the effect of driving on PT systems, one approach is analyzing V_1 and V_2. The dynamics for the voltages V_1 and V_2 can be obtained by solving Equations (1.1) and (1.2). The numerical solutions for V_1 and V_2 will be analyzed to calculate the real and imaginary parts of the eigenfrequencies. Another approach is to move to a Floquet picture. Details about the Floquet picture of a driven case can be found in [8].

The spectrum of a driven PT-symmetric system, obtained by using the Floquet theorem is shown in Figure 1.3. The spectrum supports a sequence of spontaneous PT-symmetry broken domains bounded by exceptional point degeneracies. The extra energy imposed on the system by the periodic drive, will create several localized islands of instabilities (extra gain) in the spectrum of a driven system. The position and size of these instability islands can be controlled through the amplitude and frequency of the driving and can be achieved, in principle, for arbitrary values of the gain or loss parameter. In Chapter 3, the new features in the spectrum of the driven PT system are discussed in detail.

1.2 Experimental set-up

Here I provide an experimental platform where periodically driven PT-symmetric systems can be investigated. The simplest version of the set-up is shown in Figure. 1.1b. It consists of two coupled 235 MHz LC resonators with balanced gain and loss.

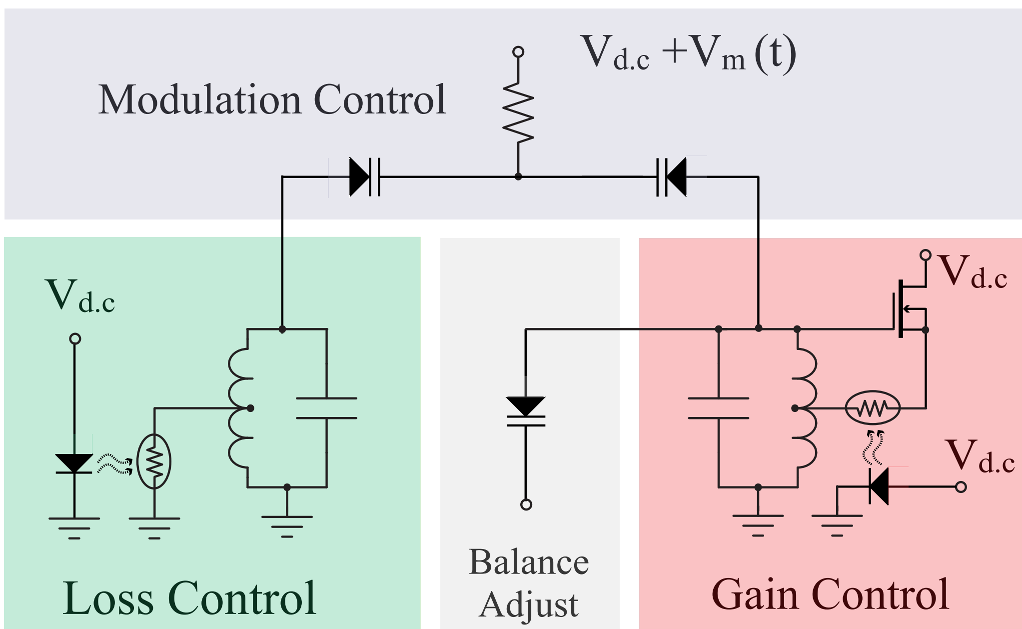

Figure 1.4: Schematic diagram of the experimental set-up. Gain side, loss side, modulationn network, and balance adjust are the four main blocks of the system. Gain side consists of LC resonator, MOSFET, and gain control network, Loss side is formed by LC resonator and loss control network. Balance adjust which is actually located in the gain side has the duty of balancing the frequencies of individual oscillators for each gain/loss parameter. The coupling network provides the Modulated coupling.

The capacitance that couples the two resonators is parametrically driven with a network of varactor diodes.

Figure 1.4 shows the schematic diagram of the experimental set-up, which is divided into the four main blocks (shown with different colors) to highlight more details. A natural frequency of $\omega_0/2\pi = 235$ MHz was chosen as the frequency of the LC oscillator. Gain and loss (corresponding to effective parallel resistances $\mp$ R) are directly implemented via Perkin-Elmer V90N3 photocells connecting the center turn of each inductor either directly to ground (loss side) or to a BF998 MOSFET following the LC node (gain side). Thus, as both photocells experience the same voltage drop, the loss side photocell extracts its current from the tap point while the gain side photocell injects its current into the tap point. The photocells are coupled to computer driven LEDs through 1 cm light pipes for RF isolation. As the gain of the MOSFET is changed, its capacitance shifts slightly, unbalancing the resonators. A BB135 varactor diode is used to compensate for these changes. In what fallows, each block will be explained individually in detail.

1.2.1 Gain side

Gain side consists of three main parts as it is shown in Figure 1.5: LC oscillator, MOSFET and optical isolator (the combination of photoresistor and LED). The last two parts together provide the gain control network.

1.2.1.1 LC Resonator

The main and hermitian part of the gain side is the LC resonator. A natural frequency of $\omega_0/2\pi$ = 230MHz was chosen as the highest frequency convenient for a simple implementation of electronic gain and loss. The L = 31.1 nH inductor is the two- turns of 1.5 mm diameter Cu wire with its hot ends supported by the parallel capacitor C = 10 pF. However, the effective capacitance of the gain side is C_{eff} = 15.4 pF. The combination of 31.1 nH inductor and C_{eff} = 15.4 pF provides a resonator which oscillates at frequency of 230 MHz.

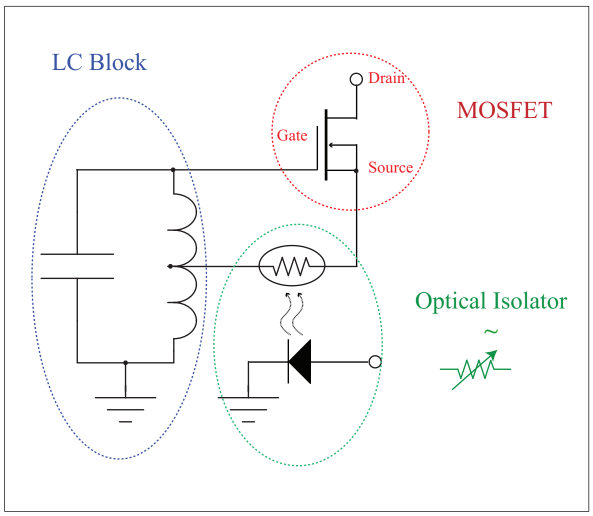

Figure 1.5: Main parts of the gain side are shown here. LC block provides the oscillatory part and combination of MOSFET and optical isolator provides the gain control network.

Extra capacitances added to the main 10 pF parallel capacitor, comes from several sources. In this system, all pieces are built and set up on a two-sided copper board base. Also, there is another vertical two-sided copper board between the gain and loss sides. This wall, isolates gain and loss sides from each other, so that no mutual coupling can occur between inductors, and no light can leak from one side to another.

A piece of copper tape attached to the copper board with a Kapton tape in between creates a capacitor. Since the copper board is kept at zero potential, this combination makes a capacitor connected to the ground. A piece of copper tape with a dimension of 1.5x2 mm is attached to the copper board in this way, makes an extra capacitance of 1.5 to 2 pF connected to ground (the stickiness of both copper and Kapton tapes is temperature dependent. So, at different temperatures the dielectric gap between the copper board and Copper tape is different). Two pieces of copper tapes with about the same dimensions are used at the connection points; one of them is used at the connection point of the LC node and coupling network, and another one at the connection point of the LC and tuning varactor.

Another major cause for having extra capacitances in the gain side, is the input capacitance of the MOSFET 1st gate. In the next section, I will discuss this issue in detail.

1.2.1.2 MOSFET

To maintain gain, a high impedance amplifier with a minimum capacitance is required. The impedance needs to be high to avoid any extra large dissipation from the system. On the other hand, the capacitance should be low since any extra capacitances will shift the LC frequency down. A BFF998 MOSFET was chosen as the device which can provide the high gain, low capacitance at the frequency of 250 MHz. Several other transistors such as 2N5486 FET were chosen and tested during the developing process. Although some of them did not have some of the BFF998 drawbacks such as having a γ dependent input capacitance, none could provide

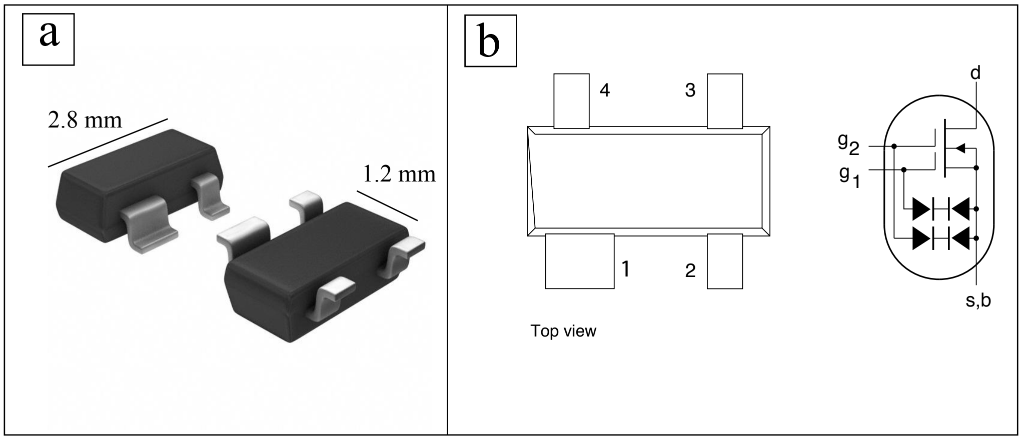

Figure 1.6: surface mounts BFF998 and dimensions (a). the top view and circuit diagram inside the device (b) g_1 and g_2 denote first and second gates, d denotes drain and s refers to the source. Figure is taken from manufacture's data sheet.

enough gain to get to the PT point at 230 MHz frequency. Figure 1.6a, b show the BFF998 surface mounts MOSFET, top view, dimensions, the circuit diagram inside the device and the pins.

A common-drain amplifier, known as a source follower, is one of the three basic field effect transistor (FET) amplifier configurations. It is mostly used as a voltage buffer. In this circuit, input is the gate terminal of the transistor, the source serves as the output, and the drain is common to both input and output (Figure 1.7a).

In the source follower topology, the voltage gain of the device defined as $A_v = V_{out} / V_{in}$ will be $A_v = g_m R_s / (g_m R_s + 1)$, where g_m is the transconductance of the device. For $g_m R_s >> 1$, A_v will be very close to 1; it means that for this configuration the source voltage follows the gate voltage.

Figure 1.7b shows the Hartley oscillator common drain scheme, where gate is connected to the LC node and source is connected to the middle of the inductor (tap

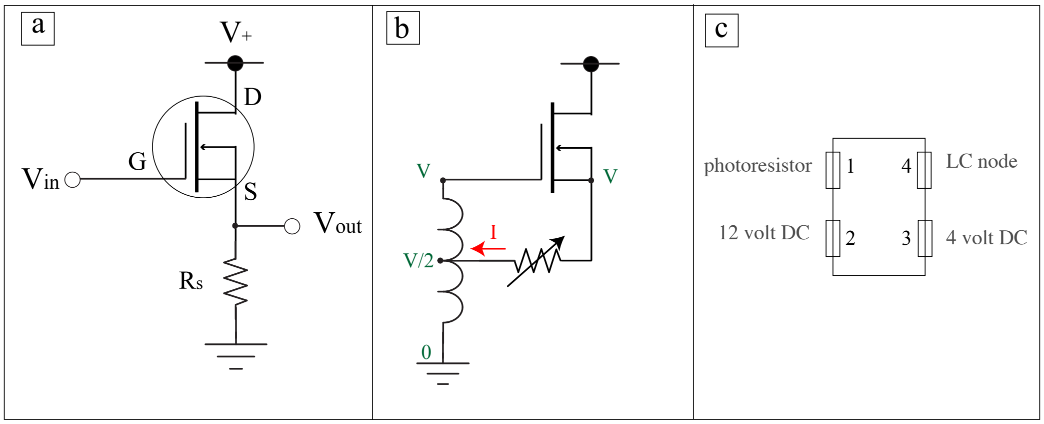

Figure 1.7: A common-drain amplifier, also known as a source follower (a). Hardly oscillator common drain scheme. BF998 MOSFET following the LC node. Thus tuning resistor (photo resistor) experiences the voltage drop, the photocell injects its current into the tap point (b). Schematic diagram of MOSFET embedded in the gain side (c).

point) via a feedback resistor. Since the inductor is directly connected to ground, its middle has the voltage which is half of the voltage at LC node. Therefore, by Ohm's law, there will be a current from the source to the tap point. Ohm's law then defines the value of this injected current. Having different resistor values provides different current values and different gain parameters.

Figure 1.7c shows the circuit digram of BFF998 which is embedded in the gain side. To get the maximum gain, the drain and gate2 need to be supplied with 12 and 4 Volt voltages, respectively. Table 1.1 shows some of the characteristics of BF998, such as its low power dissipation of 200 mW and its input capacitance at gate 1 which is 2.1 pF. BFF998 has some drawbacks at this frequency, which will be discussed in Tuning and Balancing section.

PARAMETER	SYMBOL	MAX.	UNIT
Drain-Source voltage	V_{DS}	12	V
Drain current	I_D	30	mA
total power	P_{tot}	200	mW
Input capacitance at gate1	C_{ig1}	2.1	pF

Table 1.1: BFF998 characteristics. Data is taken from manufacture's data sheet.

1.2.1.3 Optical Isolator

Exploring the parameter space of the dimer requires controlling resistances on both the gain and loss sides. To set different gain values γ, a very sensitive and wide-rage tuning resistor is required. An optical isolator consisting of a light-emitting diode enclosed with a light-sensitive photoresistor is a suitable choice for our application. The light-emitting LED controls the resistance of the photoresistor. This allows a resistance to be controlled by a current without any coupling between the control resistor circuits.

1.2.1.3.1 Photocell

A Perkin-Elmer V90N3 light-sensitive photoresistor is a suitable choice for our application. This photoresistor with the minimum resistance of 1 MΩ in the dark can provide the desirable resistance range. Figure 1.8 shows a A Perkin-Elmer V90N3 photocell and its dimensions.

The resistance of photoresistor is approximately inversely proportional to the level of light in the medium

$$R = \frac{\beta}{L_l^{\lambda}} \tag{1.4},$$

where L_l is the level of light in the medium, β and λ are two constants which will be determined during the calibration and fitting processes. While working with the photocells, some deviations from the manufacture's specification data sheet was observed. These deviations have not been reported in any of the low frequency experiments previously done in our lab. One such deviation is having a lower impedance in the dark. The dark impedance is a very important feature for us, because it can considerably increase the natural loss of the resonator.

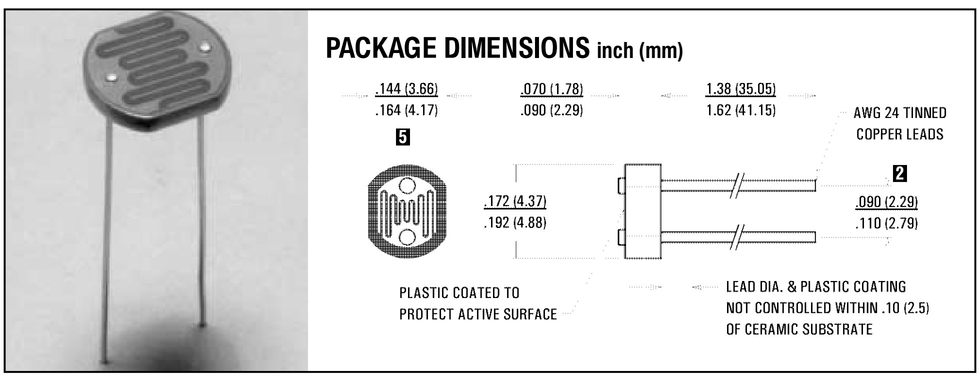

Figure 1.8: A Perkin-Elmer V90N3 light-sensitive photoresistor. Figure is taken from manufacture's data sheet.

Photocells are built to be used in low frequency systems, and all of the characteristic features mentioned in the data sheet are measured in low frequency conditions (less than 1 kHz). However, in this project we will use photocells at ultra high frequency domain. Therefore, we needed to determine some of their features at higher frequencies.

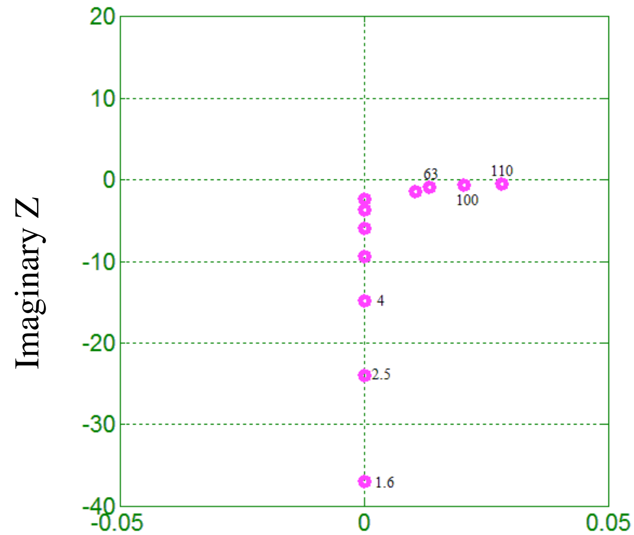

Figure 1.9: The impedance of V90N3 photo resistor is measured by HP 4193A vector impedance meter at different frequencies. Each circle shows the real and imaginary part of impedance. The number is written on each circle represents the frequency of the system in MHz.

The impedance of V90N3 photo resistor is measured by HP 4193A vector impedance meter at several different frequencies in the lab light level. The maximum frequency which can be applied to the photocell vector impedance meter is 110 MHz. The vector analyzer gives us the photocell impedance at each frequency by providing a vector with amplitude and phase angle. The real and imaginary parts of the impedance can be determined with these two numbers. Figure 1.9 shows the complex impedance of the V90N3 photo resistor at several frequencies between 1.6 to 110 MHz.

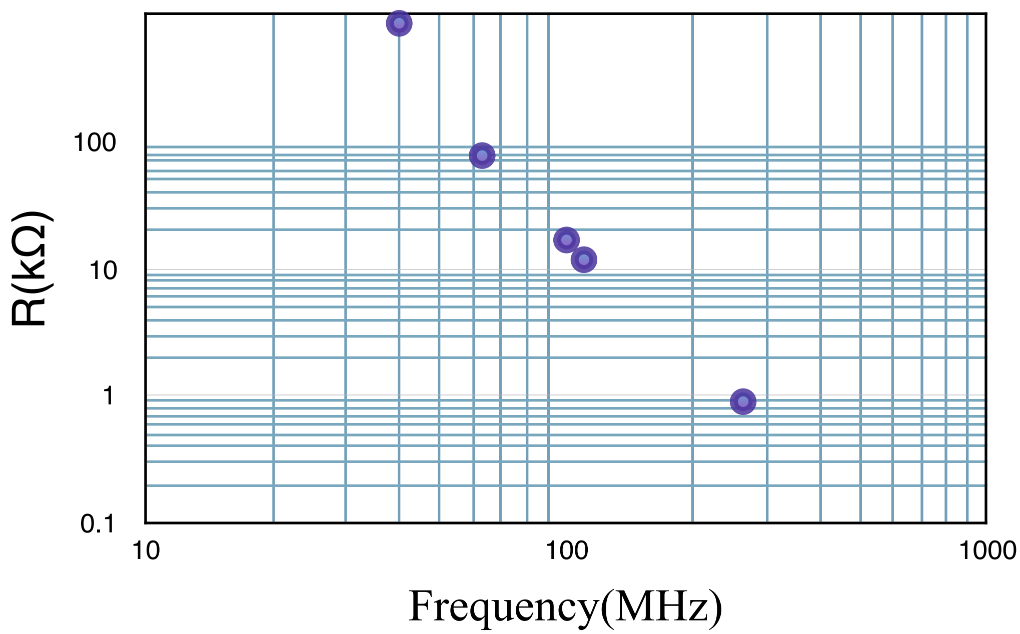

Figure 1.10: The resistance of V90N3 photo resistor in our lab in the dark, at different frequencies.

Photocells can be analyzed as a resistor and capacitor in a parallel configuration. This parallel combination has a complex impedance. The real and imaginary parts of impedance are used to measure the resistance and capacitance of the configuration. Table 1.2 shows the photocell capacitance which are obtained by analyzing data shown in Figure 1.9.

Frequency(Mhz)	40	63	100	110
Capacitance (pF)	1.3744	1.3754	1.4034	1.4021

Table 1.2 Capacitance of the V90N3 photo resistor at 4 different frequencies.

Figure 1.10 shows the resistance part of parallel configuration at different frequencies. It shows the photocell resistance in our lab in the dark (the temperature and the background light are the same in all measurements). The first four data points in Figure 1.10 are measured by the vector impedance meter, and the fifth one is the result of analysis of the LC resonator working at 230 MHz frequency with and without the photocell.

The above results show that although the capacitance of V90N3 photo resistor changes by ~ %2 at different frequencies (it stays at about 1.4 pF), its resistance will change by orders of magnitude when frequency changes from 1 to 230 MHz. At frequency of 230 MHz, even in the dark the photoresistor will add a considerable amount of loss to the system.

1.1.1.3.2 LED

A Mini half-watt LED diode from OVS5MxBCR4 Series with amber color completes the set of the optical isolator. The LED's top view and its dimensions are shown in Figure 1.11.

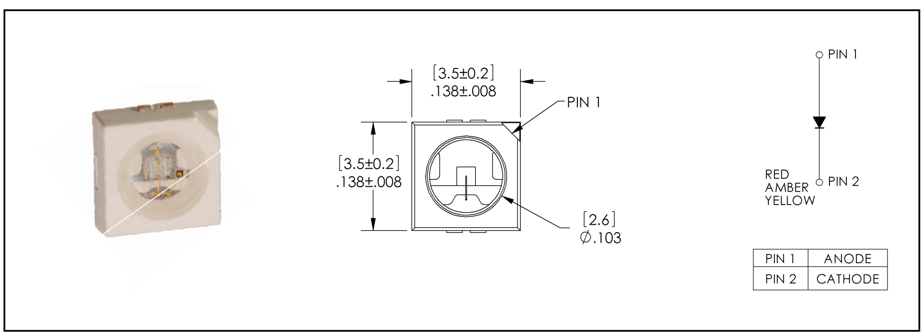

Figure 1.11: Top view of the Mini half-watt LED diode, dimensions and schematic. Dimension are in inches (mm). Figure is taken from manufacture's data sheet.

Current through the LED diode is determined by the Shockley diode equation

$$I = I_0(exp\frac{V}{V_f} - 1) \quad (1.5),$$

where V_f is forward voltage and I_0 is saturation current. Figure 1.12 shows current through the LED versus the voltage applied by the SR510 lock-in amplifier. Current first goes through a 1000 + 160 Ω series resistance (160 Ω resistor is embedded inside the dimer box, while 1 kΩ resistor which is outside the box can be replaced by other values). The forward voltage vs forward current through the amber LED diode given by data sheet is shown in the inset of Figure 1.12, there is a linear relation between

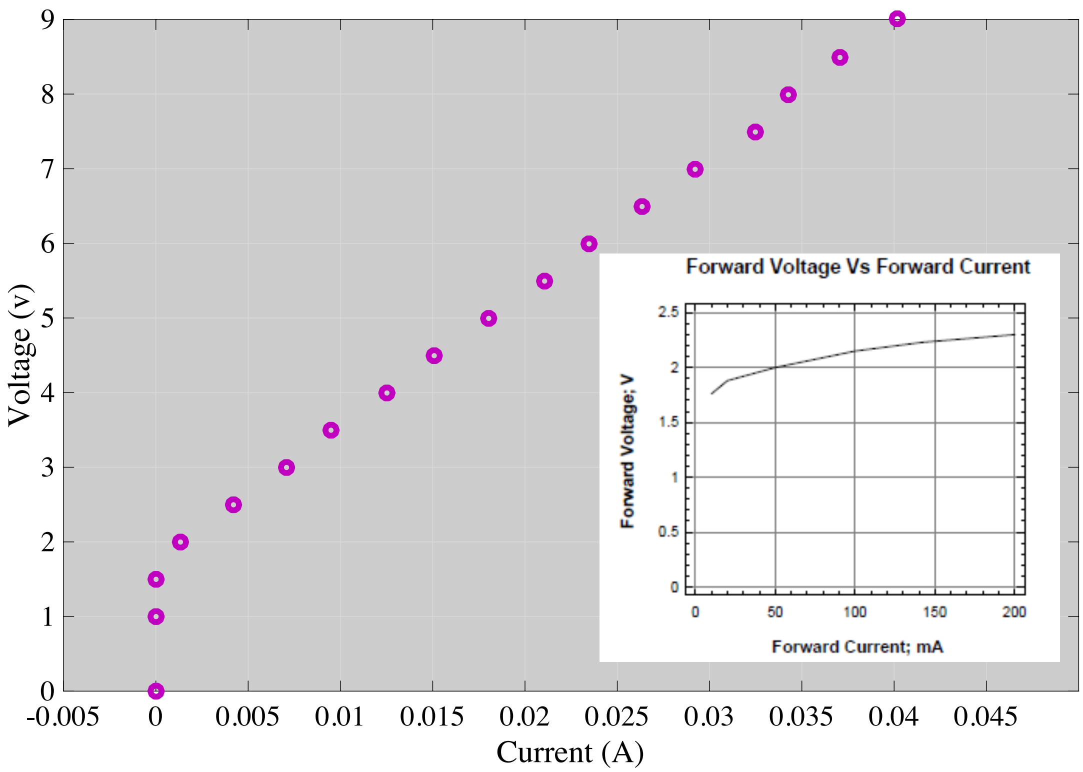

Figure1.12: (Measured data) Current through amber LED vs lock-in amplifier voltage. White background subfigure is taken from the manufacture's data sheet.

voltage and current from 5 to 40 mA in both Figure 1.12 and its inset (There is no series resistance for the data shown in Figure 1.12 inset).

Level of light (L_l) is nothing but the number of photons in the medium. The parameter behind the number of photons emitted from the LED is the current through the diode. Therefore, the level of light is defined as

$$L_l = \alpha I \tag{1.6},$$

here I is the current through the diode and α is a constant that needs to be determined.

1.1.1.3.3 Computer controlled gain

The defining characterization of an optical isolator is the behavior of its photocell conductance g (g = 1/R) versus its LED current. These should have an approximately linear relationship, since the diode's light intensity is proportional to the current, and photocell conductance depends on the number of photons emitted from the diode. Figure 1.13a shows the characterization of the optical isolator, where the photocell conductance is plotted against the current through the LED. Figure 1.13b shows the photoresistor resistance against the voltage applied by computer controlled DAC (Digital to Analog Convertor). This voltage is applied and controlled by a computer program.

The γ parameter is defined as $\gamma = Z_0/R$ in PT Electronics systems, where R (-R) is parallel to LC oscillator and Z_0 is the characteristic impedance of the LC. $Z_0 = (L/C)^{1/2}$ is 40 in our system. However, for The Hartley gain configuration where R (photoresistor) is not parallel to the LC oscillator anymore (Figure 1.7b), the equivalent γ in gain side will be

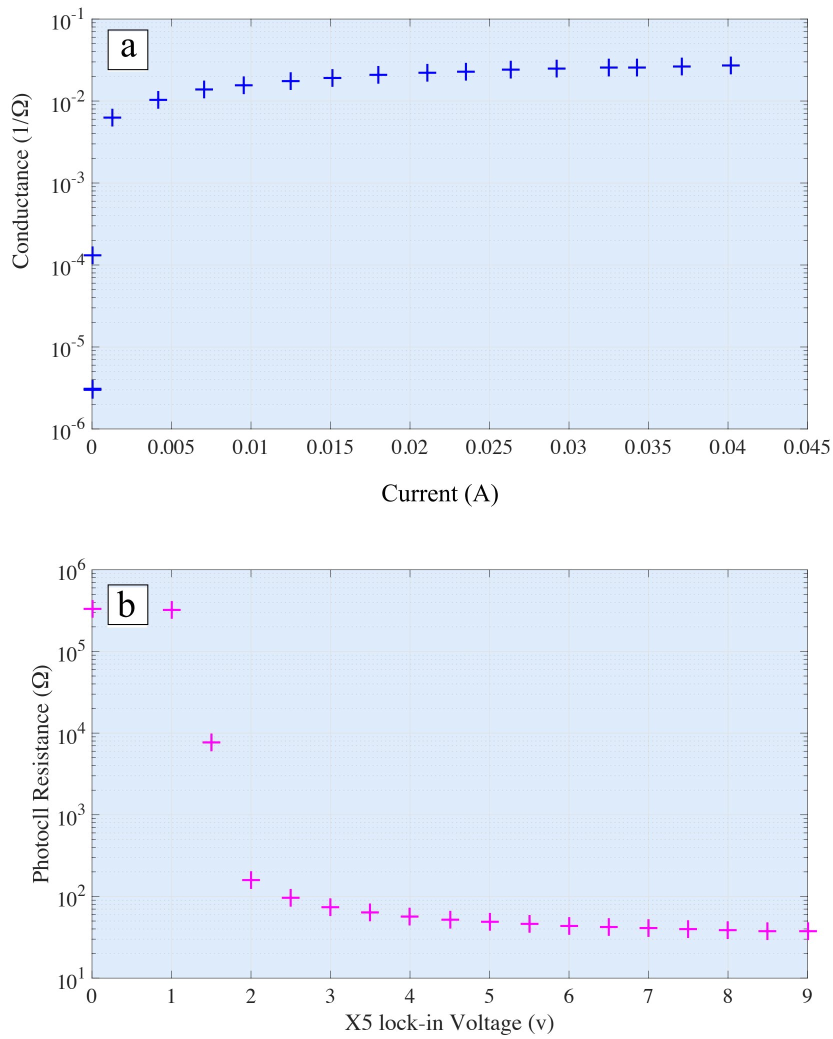

Figure 1.13: (Measured data) (a) photocell conductance g (g = 1/R) versus LED current. (b) photocell resistance (R) versus voltage applied on LED diode by computer. (logarithmic y axis)

$$\gamma = \gamma_0 - \frac{Z_0}{4(R + 131)} \qquad (1.7),$$

by the Kirchhoff law. Here γ_0 is the natural loss of the LC oscillator which is $\gamma_0 = 0.008$ in gain side. γ_0 is found by using the phase-comparison method (please see the Phase Comparison section). Finally, voltage across the LED is determined by

$$V = V_{DAC} - IR_s \tag{1.8}$$

R_s is the series resistance with diode. Gain side LED is running by DAC in the SR510 lock-in amplifier. Current first goes through the 1160 Ω series resistance. Figure 1.14 shows the DAC voltage versus the γ parameter in gain side. In this figure, experimental data obtained by using the phase-comparison method are fitted with the function derived by using equations (1.4)-(1.8). Using phase-comparison method for oscillators with gain has some restrictions, however it can be done after applying some modifications, see section 2.3.

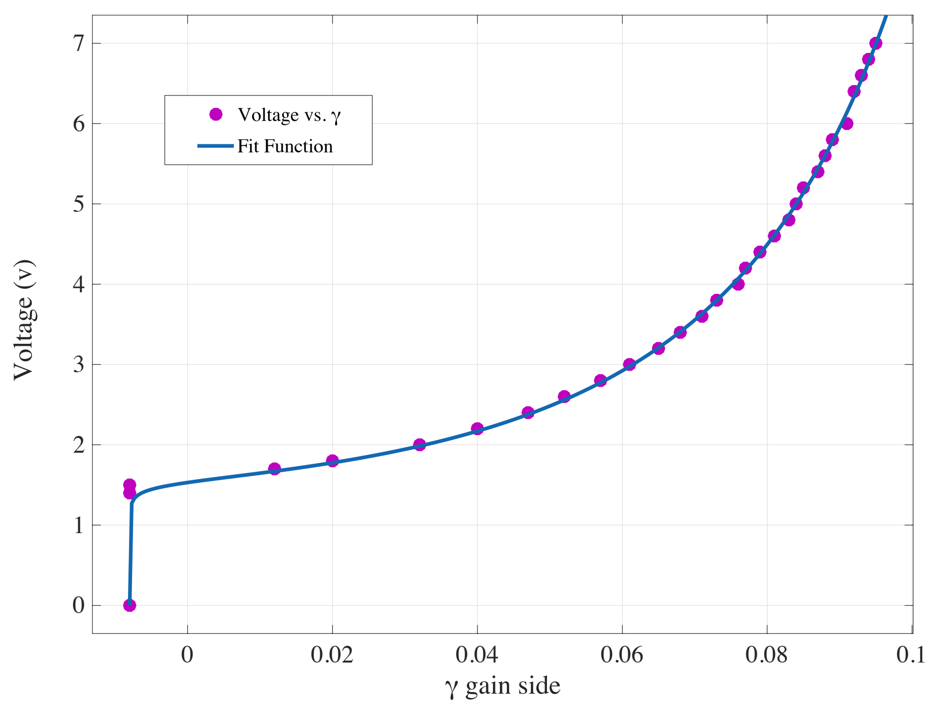

Figure 1.14: DAC voltage vs γ parameter in the gain side.

1.1.1.3.3 Practical Consideration

There are some points to be considered while using the optical isolator:

- There must be a suitable distance between the LED and the photocell to avoid the RF effects of the light emitting diode on the LC resonator. In this system, LED is located 1.1 cm away from the photoresistor. However to maximize the effect of light steps on photoresistor, a 1 cm light pipe is used to direct the light from LED to photoresistor.

- Calibration needs to be done at least 48 hours after using soldering on any piece of the system. The very high temperature of soldering iron (~ 100 ^{0} C) affects the behavior of different elements in the system, such as the operation of photoresistors, thickness of copper and Kaptan tapes and etc.

- Setting very small γs (less than DAC = 2 Volts in the gain side) should be avoided. Applying very small voltages (very large Rs), causes undesirable time relaxation.

- The photoresistor equilibrium time has a direct relation with the light steps. Going from one γ to another with a large step (ΔDAC in the unit of Volts) might need hours to equilibrate, while ΔDAC in the order of 0.001Volts will equilibrate in less than a seconds [10].

- The gain control network (optical isolator) needs to be calibrated over days-long timescale. Optical isolators are restrained to days-long drifting.

1.1.2 Loss side

The schematic diagram of loss side is shown in Figure 1.15. It has two main components: LC resonator and optical isolator that are explained in detail in the following subsections.

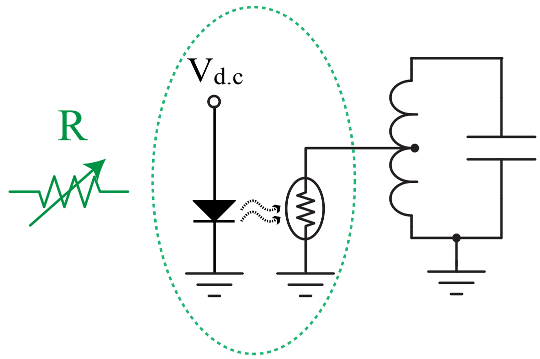

Figure 1.15 Schematic digram of Loss side.

1.1.2.1 LC Resonator

The oscillatory part of loss side is also provided by an LC resonator. To satisfy the symmetry, it is necessary to build it as similar as possible to its pair in the gain side. The L = 31.1 nH inductor is the two-turns of 1.5 mm diameter Cu wire with its hot ends supported by the parallel C = 10 pF. In building the inductor pairs in the loss and gain side, I tried to make the same length, radius and orientation. The natural frequency of the loss side is also chosen to be $\omega_0/2\pi = 230$MHz.

Although there is no need for MOSFET in the loss side, for both space and electronics symmetry purposes, loss side was also originally built by embedding a BF998 MOSFET, as it is shown in Figure 1.16. The goal was to have all the MOSFET effects in both sides, such as the gate input capacitance of 2.1 pF. However, later because of the complications that having BF998 MOSFET added to the system (they will be discussed in detail in tuning and balancing sections) , it was removed from the loss side. One might think that even if MOSFET adds any complications, it will add them to both sides and that even might be helpful during the calibration and balancing process. However, since MOSFETs are added to gain and loss sides in different ways (please see the circuit diagrams related to MOSFETs in both gain and loss side), the rate and direction of those complications are not the same.

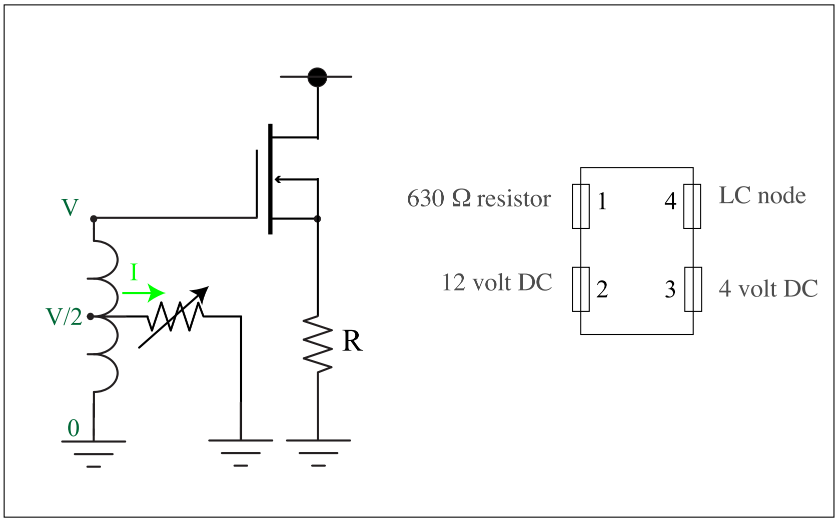

Fig 1.16: To satisfy symmetry, loss side was also built by embedding a BF998 MOSFET, but later because of all the complications MOSFET adds to the system it was removed from loss side.

After removing the MOSFET from loss side, to compensate for the extra capacitances that the MOSFET in gain side added to the system, copper tape capacitances (they are discussed in details in gain side) were made longer in this side. So, the effective capacitance of loss side is also C_{eff} = 15.4 pF.

1.1.1.3 Optical Isolator

Again for space and electronics symmetry purposes, the photoresistor connects the middle of the inductor to the ground, the comparison is shown in Figure 1.17. By

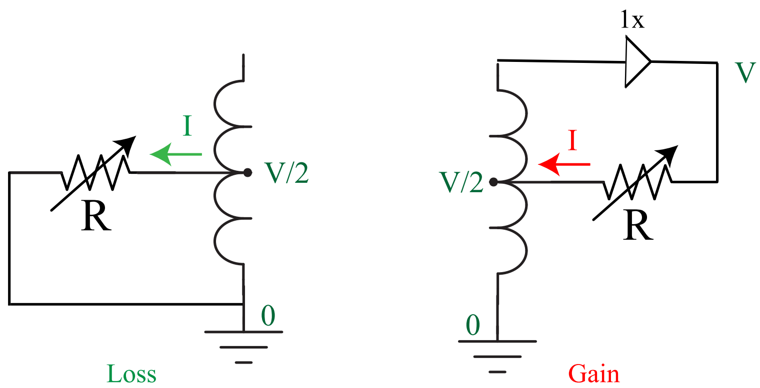

Figure 1.17: Comparison between having gain and dissipation in the gain and loss sides. Since Hartley scheme is used in gain side, dissipating piece in the loss side also connects the tab point to ground.

Ohm's low, currents leaving and entering the inductors in left and right side will have the same V/2R value.

Dissipation in loss side is provided by using a set of LED and photocell similar to gain side which are related according to equation (1.4). Gain and loss are isolated from each other except for coupling, and the level of light in one medium has no effect on the other one. β, λ, and α in Equations (1.4) and (1.6) should be determined again for the loss side, despite having an LED, photocell, and 1.1-centimeter light pump (guides the light) that are similar to their counterparts in the gain side. This is because any small changes such as the orientation of photocell or LED can affect these three constants.

The γ parameter in loss side will be (Figure 1.17)

$$\gamma = \gamma_0 + \frac{Z_0}{4R} \qquad (1.9),$$

where γ_0 is the natural loss of LC oscillator. In the loss side, $\gamma_0 = 0.01$ is found by using the phase comparison method (please see section 2.3 for further details).

Voltage across the LED is determined by

$$V = V_{DAC} - IR_s \tag{1.10}$$

R_s is the series resistance with diode. Loss side LED is running by DAC2 in the 7265 DSP lock-in amplifier. There is an internal 1 kΩ series resistance in the lock-in amplifier. In our set-up, current also goes through another 160 Ω, so the total series resistance in the loss side is 1160 Ω.

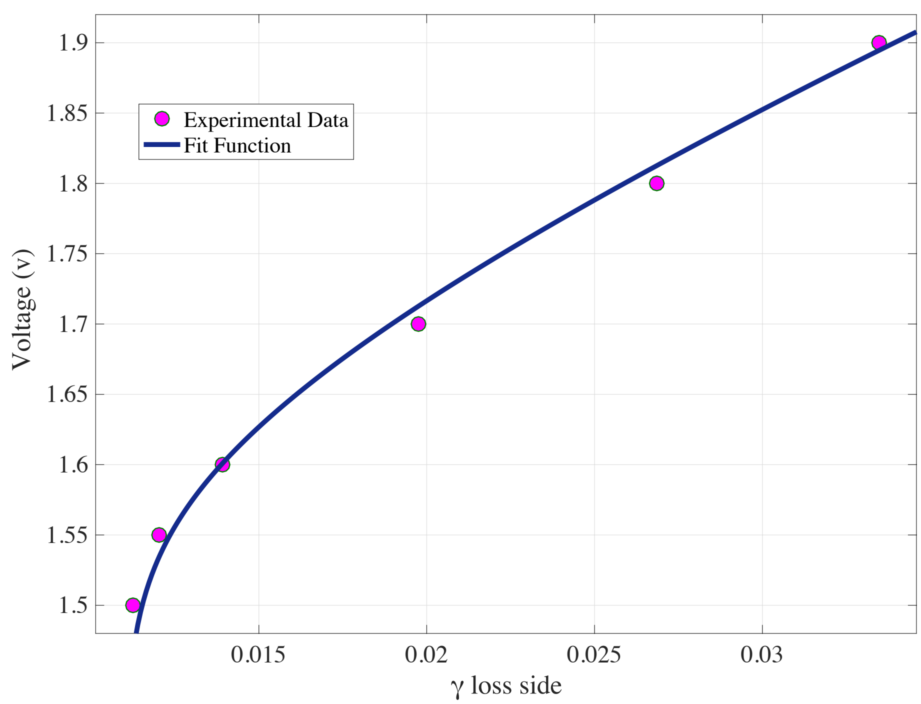

Figure 1.18: DAC2 voltage vs γ parameter in loss side. Experimental data points fitted to a function obtained by the Equations (1.4) to (1.6), Equation (1.9), and Equation (1.10).

Figure 1.18 shows the DAC voltage versus γ. Experimental data points are fitted to a function obtained by Equations (1.4) to (1.6), Equations (1.9), and (1.10). Experimental points are determined by using the phase comparison method.

1.1.3 Coupling Network

Two LC resonators which are the main blocks of the system are coupled capacitively. To have the full control on coupling, any mutual coupling between inductors should be avoided. This is achieved by placing an grounded isolating wall between the gain and loss sides. Theoretically, the driven capacitive coupling should be given as $c = C_c/C = c_0 + \varepsilon \cos(\omega_m \tau)$. The first term c_0, describes the constant background coupling, and the second term refers to the periodic driving part which changes as a function of time with amplitude ε and frequency of ω_m.

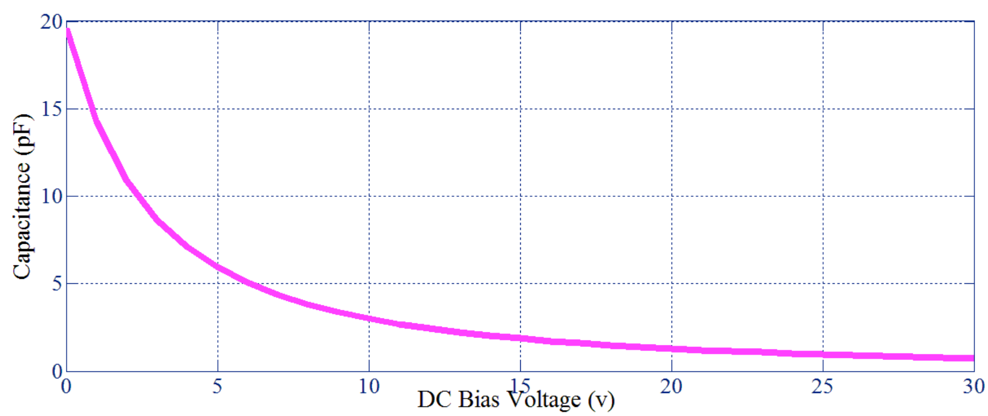

Figure 1.19: The capacitance of BB135 varactor diode as a function of DC biased voltage across it.

Varactors are the voltage-controlled capacitors. They are designed to exploit the voltage-dependent capacitance of reversed-biased p-n junction. The BB135 varactor diode with a capacitance varying between 1 and 19 pF is chosen to maintain the constant background coupling in the order of 1/10 of the resonator capacitance ($c_0 \sim 0.1$) and driving amplitude of about 1 percent of resonator capacitance ($\varepsilon \sim 0.01$). The BB135 varactor diode capacitance versus the biased voltage across it, is shown in Figure 1.19.

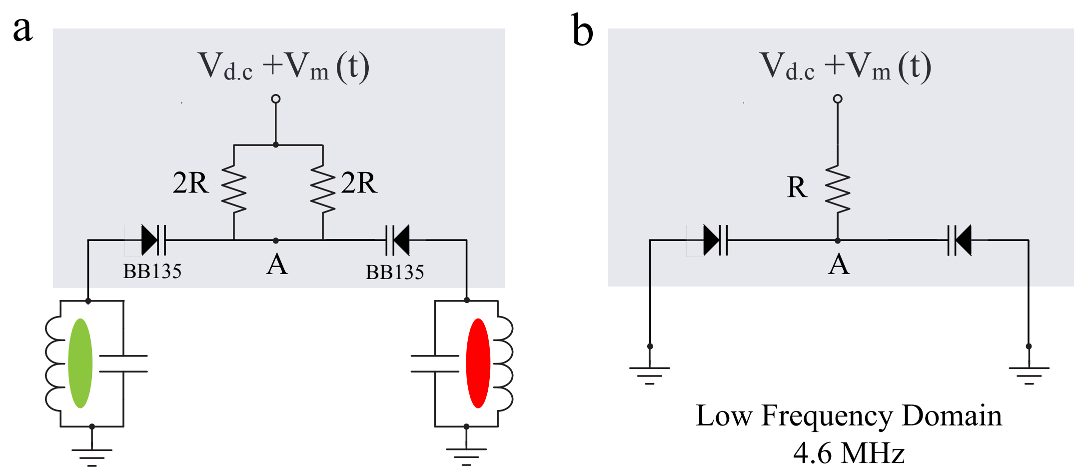

Figure 1.20: The coupling varactor network is shown in (a), and its equivalent at frequency of 4.6 MHz which is low frequency domain compared to 230 MHz is shown in (b).

The capacitive coupling network, implemented by these varactors, is optimized for application of a modulation frequency in the vicinity of 4.6 MHz while simultaneously providing the DC bias necessary for controlling the inter-resonator coupling C_c. The coupling varactor network is shown in Figure 1.20a. Two face-to-face BB135 diodes are joint though a 3 mm hole in the wall. To maintain the symmetry each varactor is connected to the bias supply with a 20 k resistor.

The network operating at frequency of 4.6 MHz (low frequency domain) is shown in Figure 1.20b. At this frequency, 32 nH inductors are equivalent to short circuits to

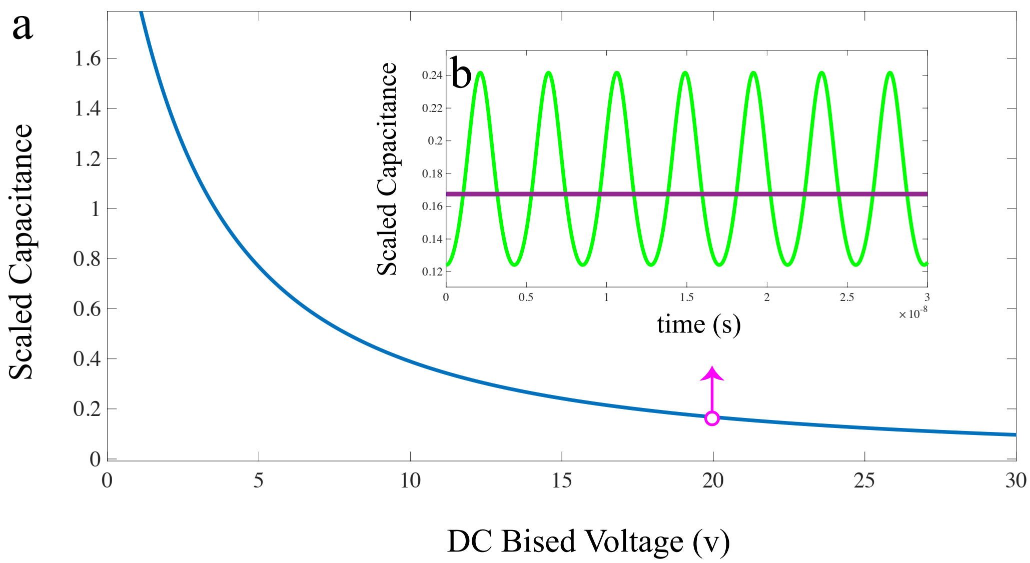

Figure 1.21: Scaled capacitance coupling $c = C_c/C$ ($C = 15.4$ pF is the resonator's capacitance) versus the DC biased voltage (a). The time dependent coupling between gain and loss side $c = c_0 + \varepsilon \cos(\omega_m \tau)$, where the purple constant line indicates c_0 and the green line shows the oscillatory part (b).

ground. Inductors act like ordinary connecting wires and their resistances are zero. Varactors behave like two parallel capacitances at the frequency of 4.6 MHz. The overall scaled capacitance of this network as a function of the DC voltage across that is shown in Figure 1.21a.

Resistance R plays a critical role here. The value of R needs to be large enough to avoid any big dissipation of energy from the resonators, because node “A” in Figure 1.20b may have an oscillating voltage at 230 MHz. On the other hand, the resistance needs to be small enough to minimize the attenuation of the 4.6 MHz signal from power supply to point A. Its value is chosen to be 10 k (2 parallel 20 k resistances) to optimize for these two cases. Figure 1.21b shows the capacitance of the network where a 20 Volts DC voltage and a 5 Volts AC voltage with frequency of 4.6 MHz is

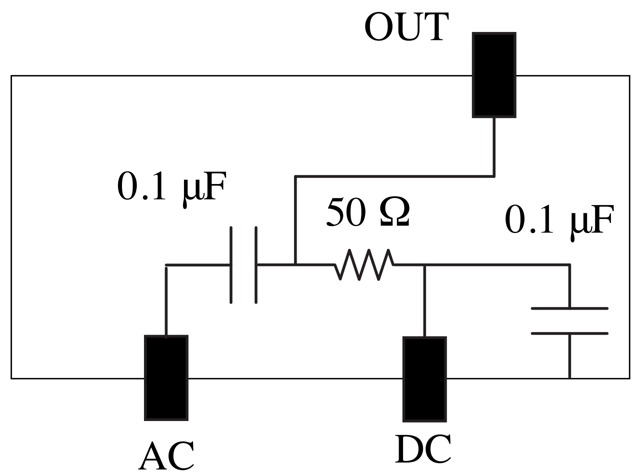

Figure 1.22: Mixing AC and DC voltages to be applied to the coupling network.

applied. The 4.6 MHz AC voltage coming from an HP3325A function generator is added with the DC voltage provided by DAC. DAC is multiplied by 3 in the 3X amplifying box and becomes 17 volt. This 17 Volts DC is then added to the 5 Volts peak to peak AC in the box, see Figure 1.22.

1.1.4 Tuning

It's been always essential to balance the frequencies and γs of coupled resonators in PT electronics set-ups, no matter how similar the individual oscillators are made. Coupling can always make oscillators to go out of balance. To slightly rebalance the frequency of LC resonators in gain and loss sides, different methods have been used in the past based on the accuracy and convenience of the method for a specific frequency range and apparatus [1-8], [10].

It's been convenient in some cases to change and adjust the inductance part of the resonator [10]). Ferrite beads (Figure 1.23a) are good choices where frequency needs

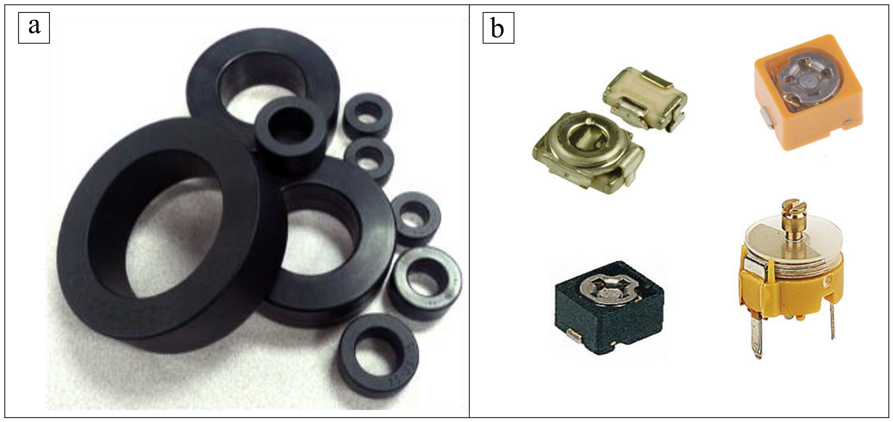

Figure 1.23: Ferrite beads (a) can be used as a frequency adjust. By choosing the right Ferrite bead with the right dimension and dissipation factor and putting it in the vicinity of inductor coil, the permittivity factor of the space changes and that directly has influences the effective inductance of the coil. Tuning capacitors (b) can be used to adjust the frequencies by changing the capacitance part of resonator.

to be adjusted just once, and we do not want to physically change C or L directly. By choosing the right Ferrite bead with the right dimension and dissipation factor and putting it in the vicinity of the inductor coil, the permittivity factor of the space changes and that directly influences the effective inductance of the coil.

Changing the capacitance part of the resonator is another option. Mechanical tuning capacitances have been used in several projects [10]. They are chosen based on the desired capacitance range (Figure 1.23b), and their capacitor needs to be adjusted by hand or using a screw driver.

The essential and critical role of tuning was predicted from the very beginning of the UHF project. However, for reasons explained below tuning UHF systems is much more challenging than low frequency set-ups.

1. As the gain of MOSFET varies, its capacitance shifts slightly, unbalancing the resonators. This is the most important drawback of BFF998 MOSFET and also the most important reason to have a very fine computer-based control tuning network in this project. Figure 1.24 shows the frequency of gain side as a function of the γ parameter. Calculating the γ parameter in this case is not trivial and can be tricky. Because applying higher voltages for the LED diode, not only changes the resistance of photocell but also varies the frequency and the characteristic impedance ($Z_0 = (L/C)^{1/2}$) of the resonator. The data in Figure 1.24 is obtained by the phase comparison method. In section 2.3, I explain how the frequency and γ are measured for the high values of gain. In the beginning by increasing γ, the frequency increases a little bit and then decreases. So,

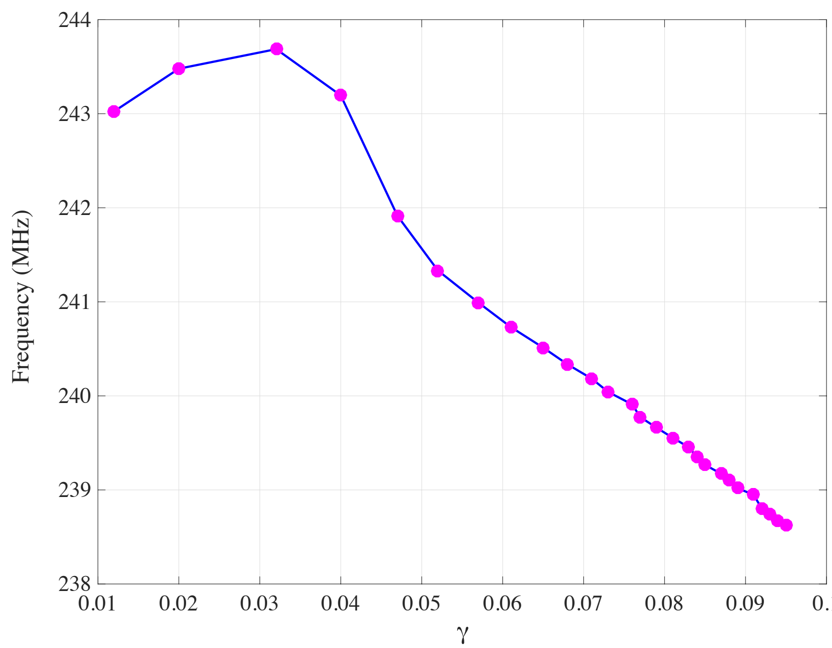

Figure 1.24 Frequency of a test gain side with a BF998 MOSFET vs γ parameter.

system needs to be retuned for every single value of γ and there should be a sensitive tuning capacitor to compensate for these changes.

2. At frequency of 230 MHz, existence of 0.5 centimeter wire or a small piece of copper tape can change the frequency of the LC oscillator by a significant amount. For example, a piece of copper tape with 1x2 mm dimension which is stuck to the copper board with a Kapton tape at the middle will create an extra capacitance of 1 to 2 pF to ground (the stickiness of both copper and Kapton tapes really depend on the temperature) and this capacitance change is enough to change the *LC* frequency by about 10 MHz.

3. Gain and loss side need to be isolated from each other and also from the outside world. The level of light in each side needs to be independent of anything but the voltage across the LED diode in that side. And also gain and loss sides need to be isolated from each other to prevent any type of mutual coupling between inductors in gain and loss side or any other frequency outside the box. The resonators are therefore kept in a box with metal walls and a wall between gain and loss. However, this closed box limits the use of balancing tools which need mechanical actions.

4. Even if elements in the box were accessible for mechanical tuning from outside the box, these mechanical actions could change other parameters in the system. For example, the LED diodes are kept in place to face the photoresistors by very thin wires. Any kind of mechanical action that could shake the box could change the direction of these LEDs and ruin the γ calibration.

5. Photoresistors and copper taped capacitances are the examples of two temperature dependent elements in the system. The capacitance of copper tapes can be slightly different in different temperatures because the thickness of Kapton tape at the middle will be different in those temperatures. The system needs to be recalibrated and retuned every time before doing the measurement.

For the reasons mentioned above I was not able to use mechanical adjusting in tuning the 230 MHz system. A BB135 varactor diode is used to compensate for all these effects. Figure 1.25 shows the schematic diagram of the tuning part. This part is located in the gain side, and "LC node" tag refers to the LC node in the gain side. The main purpose of this tuning network is to compensate for MOSFET capacitive effects at different gain values.

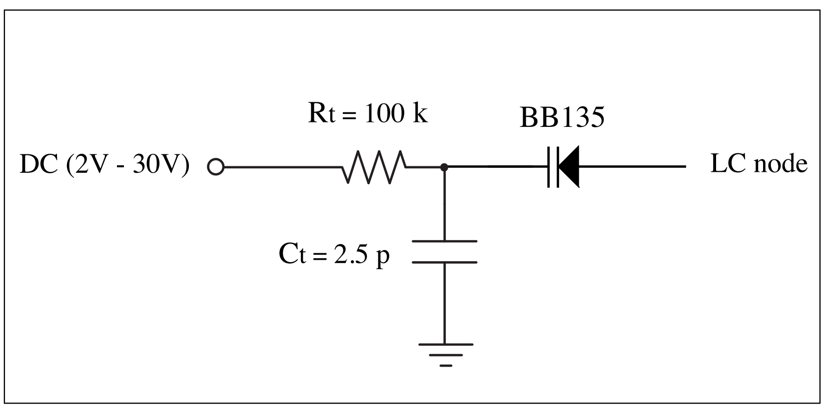

Figure 1.25: Schematic diagram of tuning part which is located in gain side.

C_t is chosen based on the required capacitance range. This range is predicted by analyzing experimental data shown in Figure 1.24. This capacitance is made from two 1x2 mm copper tapes with a piece of Kaptan tape at the middle. Its capacitance is measured by the vector impedance meter.

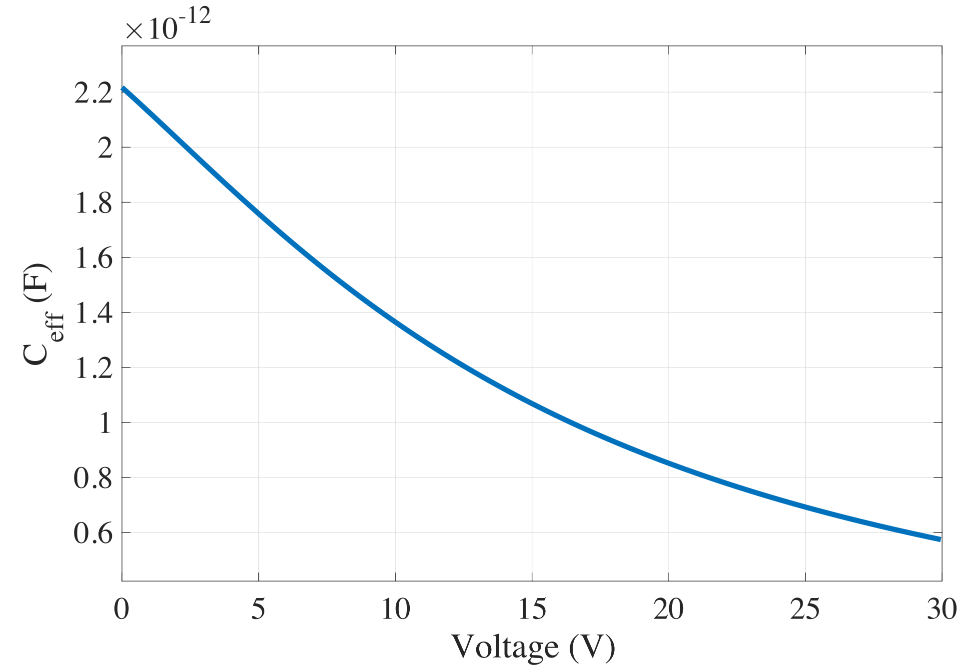

Figure 1.26: The effective capacitance of adjusting varactor circuit versus the DC voltage applied by lock-in amplifier.

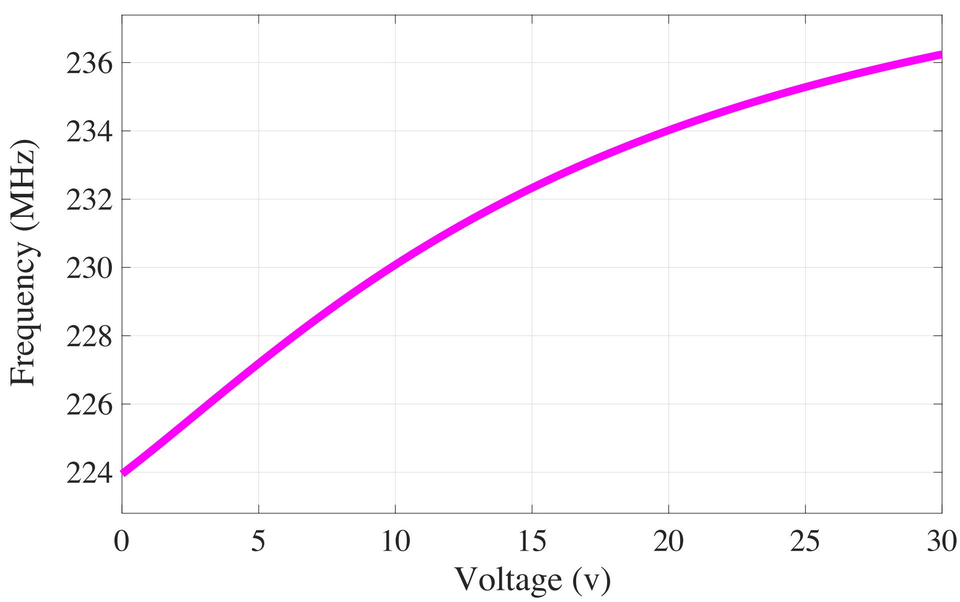

Figure 1.27: The effective frequency of gain side by having the tuning varactor.

Computer controlled DAC provides the DC voltage for the tuning varactor. However, the maximum voltage we get from these DACs is 10 Volts. This voltage goes through our 3X amplifying box, multiplied three times and then goes to the varactor.

Figure 1.26 shows the effective capacitance of adjusting circuit, shown in Figure 1.25, at different DAC voltages. By connecting one end of BB135 to the LC node, the effective capacitance of tuning network now becomes parallel with C (LC capacitance). The effective frequency of gain side is shown in Figure 1.27. Details about balancing the system will be discussed in Chapter 2, Balancing section.

Chapter 2

Technics and Methods

This chapter will summarize the methods and experimental techniques used to acquire the data reported in chapter 1 and chapter 3.

2.1 Pulsing Technic

To study the dynamics of the system, we need to be able to observe the system's output on the oscilloscope, capture it in the computer and finally analyze the transient part of the signal. We need the transient part of the signals to calculate the real and imaginary parts of eigenmodes.

There are nonlinear elements in the system such as MOSFET or amplifiers and oscilloscope in the acquisition set-up (for more details see the signal acquisition section). Amplifiers, in particular, are constrained by linearity limitations, especially around the exceptional points. All of these elements can saturate the output of the system after a very short amount of time. A saturated signal does not tell us anything

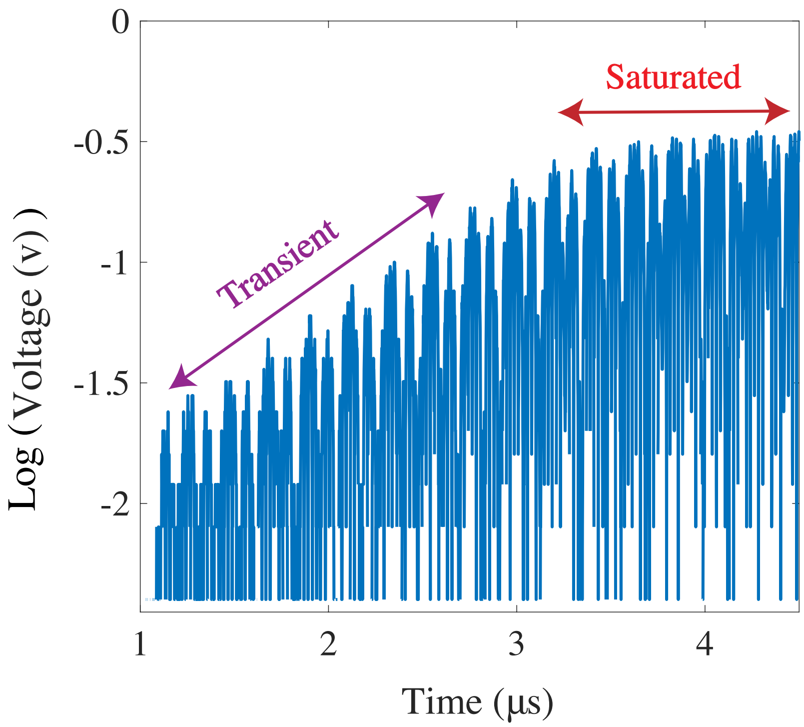

Figure 2.1: Output signal obtained from antenna located in the loss side for $\gamma = 0.0483$, with modulated coupling.

about the imaginary parts of eigenfrequencies (which are determined by the rate of growth and decay), and the real part of its eigenfrequency could also be affected by the nonlinearities.

Therefore, the only section of the output signal that is useful for us is the part which starts growing (decaying) from the beginning until right before it saturates (Figure 2.1). Depending on the growth/decay rate, there are several of microseconds before the growing signal saturates. For example, the signal shown in Figure 2.1 starts to saturate at about 3 μs.

Oscilloscope needs to be triggered properly, so that it starts capturing the data from the very first moment the signal starts growing/decaying. One possibility would be triggering the aux port of oscilloscope with the LED voltage. After all, the gain

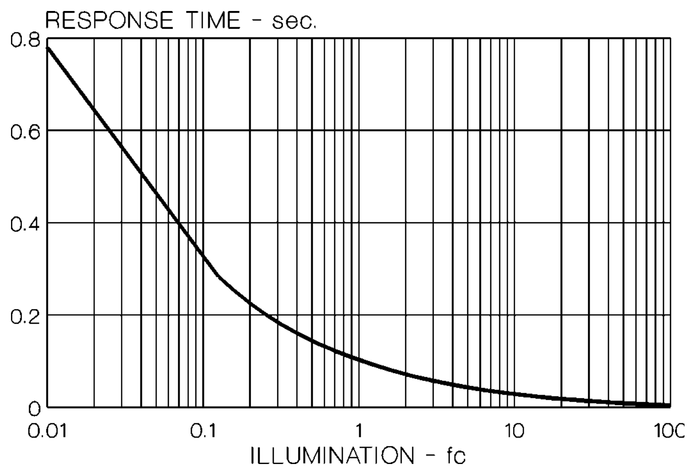

Figure 2.2: Perkin-Elmer photocell V90N3 response Time vs. Illumination (Rise Time). Figure is taken from manufacture's data sheet.

value determines the output amplitude. And the element which controls gain parameter in the system is photoresistor which itself is controlled by LED voltage. However, there is a problem in using the phororesistor as a reference. The response time of the photocell even for a very small amount of light change (ΔDAC = 0.00025 volt) is in the order of milliseconds. This response time would be impractical, because there are only a few microseconds to capture the signal before it saturates. Figure 2.2 shows the rising time of a typical Perkin-Elmer V90N3 photoresistor.

Another possibility would be triggering the aux port of oscilloscope with the MOSFET voltage. MOSFET is another element in the gain control set, the drain pin of MOSFET is run by a 12 Volts DC voltage. Running the drain with a square wave with 12 Volts amplitude which changes from 0 to 12 Volts with a rising time of a couple of nanoseconds can solve the problem. The HP3325A function generator can provide a square wave with rising time of 30 ns (Figure 2.3), and the maximum

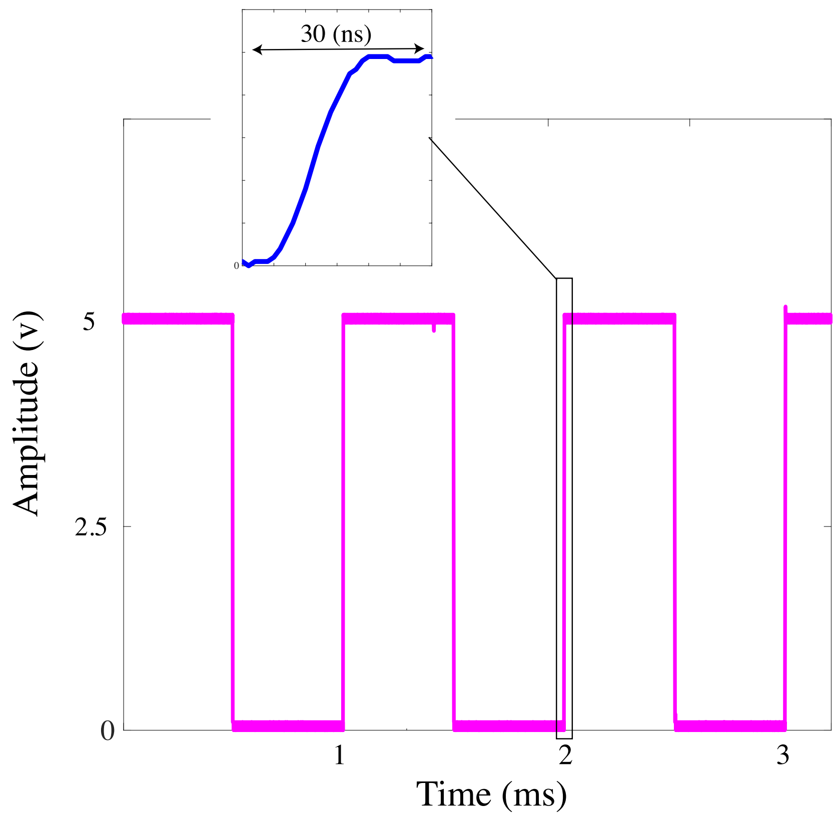

Figure 2.3: 3325A function generator provides a square wave with rising time of 30 ns and the maximum amplitude of 10 Volts.

amplitude is 5 Volts. A gate driver will be used to solve the amplitude problem and to decrease the rising time.

The FAN3111 1A gate driver is designed to drive an N-channel enhancement-mode MOSFET in low-side switching applications. It has several applications and can be used as switch-mode power supply, synchronous circuit rectifier, pulse transformer driver, logic to power buffer, and motor controller. Figure 2.4 shows the circuit digram of using FAN3111 as a logic to power buffer. This circuit provides a square wave signal with 12 Volts amplitude and the rising time of less than 10 ns by using the signal generator signal as an input (Figure 2.3).

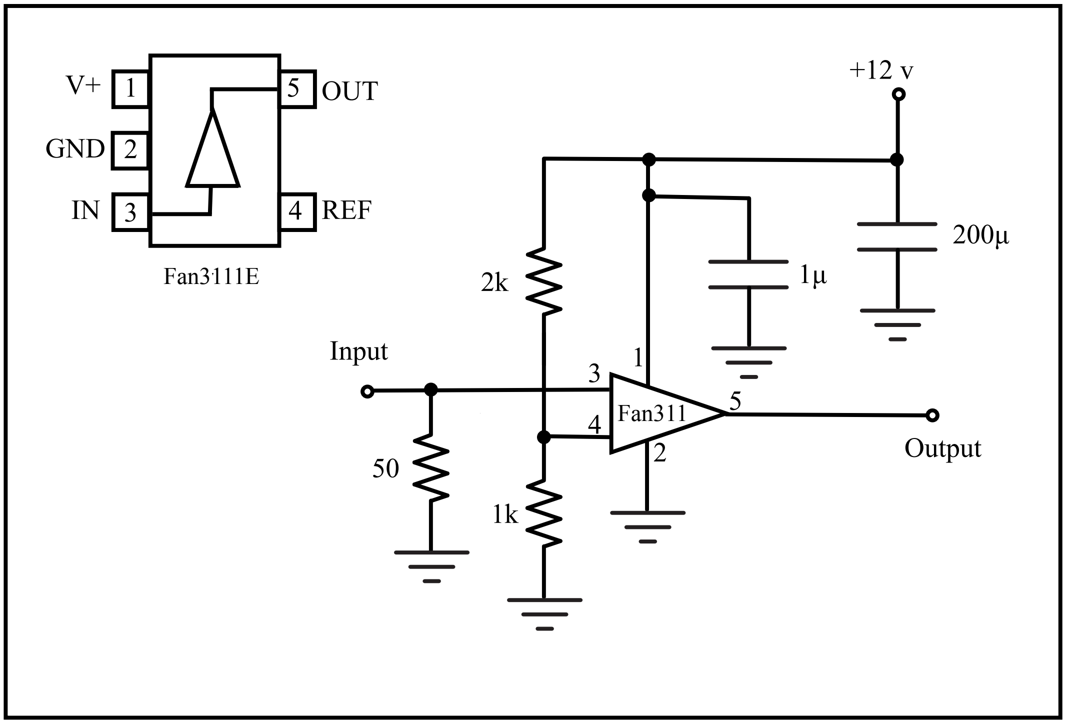

Figure 2.4: Circuit digram of drain-pulser box as a logic to power buffer .

For use with low-voltage controllers and input-signal sources that operate with a lower supply voltage than the driver, that supply voltage may also be used as the reference for the input thresholds of the FAN3111E. This driver has a single, non-inverting, low-voltage input plus a DC input V_{XREF} for an external reference voltage in the range of 2 to 5V.

The FAN3111 is especially useful for cleaning up and level-shifting trigger signals. In a non-inverting driver configuration, the IN- pin should be a logic low signal. When the IN- pin is connected to a logic high, a disable function is realized, and the driver output remains low regardless of the state of the IN+ pin.

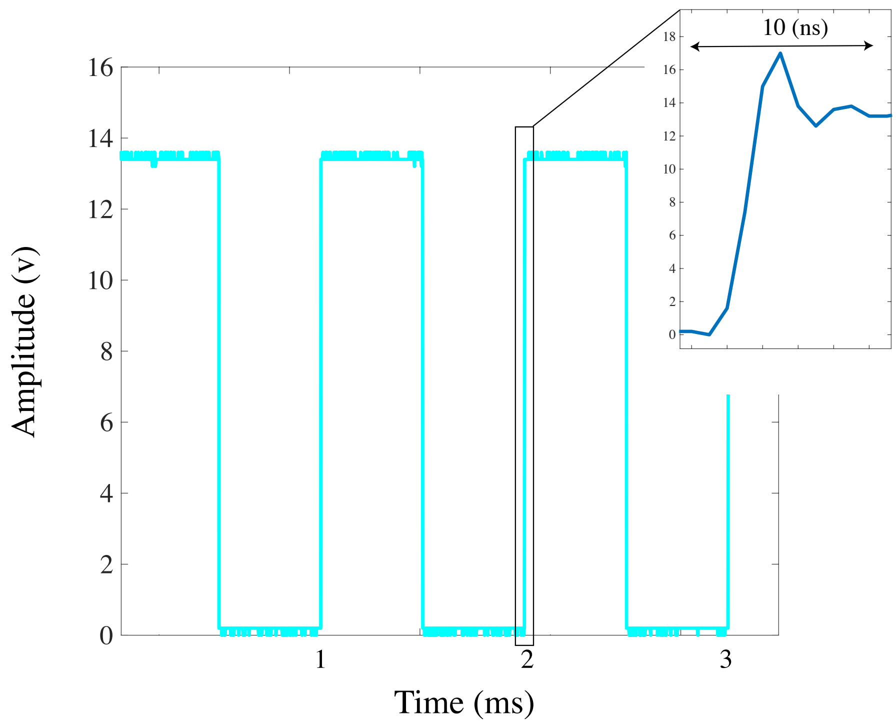

Figure 2.5: The output of drain-pulser box which is directly connected to MOSFET drain.

In the non-inverting driver configuration shown in Figure 2.4, the IN- pin is tied to the ground and the input signal is applied to the IN+ pin. The IN- pin can be connected to logic high to disable the driver and the output remains low, regardless of the state of the IN+ pin.

Practical Considerations

- The input needs a 50 Ohm termination.
- To allow this IC to turn on a power device quickly, a local, high-frequency, bypass capacitor should be connected between the V_{DD} and GND pins with minimal trace

length. In other words, 1μF bypass capacitance needs to be as close as possible to pin 1, 2.

- 1, 2 kOhm resistors are chosen to make a 3V to 5V reference voltage, they can be anything else as long as they make this range of voltage.

Figure 2.5 shows the output of drain-pulser Box which is directly connected to MOSFET drain. The input is shown in Figure 2.3.

2.2 Self-Balance and Calibrating Technic

In any experimental system, it needs to be considered that all physical electronic elements deviate from their ideal functions. This is what makes developing microwave electronics particularly challenging. In section 1.1.4, tuning section, we mentioned why a very accurate computer-based tuning and calibrating technique is required in the current project.

In the exact PT phase regime, for any value of γ, there are always two modes in the spectrum of the PT dimer. It means that moving along the green line in Figure 2.6a, and having the same frequencies for resonators, leads to a zero imaginary part and two eigenfrequencies in the spectrum of the system (Figure 2.6b). This characteristic behavior is the basis of our self-balancing method.

On the other hand, numerical analysis shows deviation in the frequencies of individual oscillators makes one of the modes dominant in the system. Figure 2.6c (2.6d) shows the dominant frequency in the spectrum when the capacitance of gain side is %0.2 to %1 larger (smaller) than the capacitance of loss side. From now on, the High mode refers to the frequencies in Figure 2.6d and Low mode denotes the

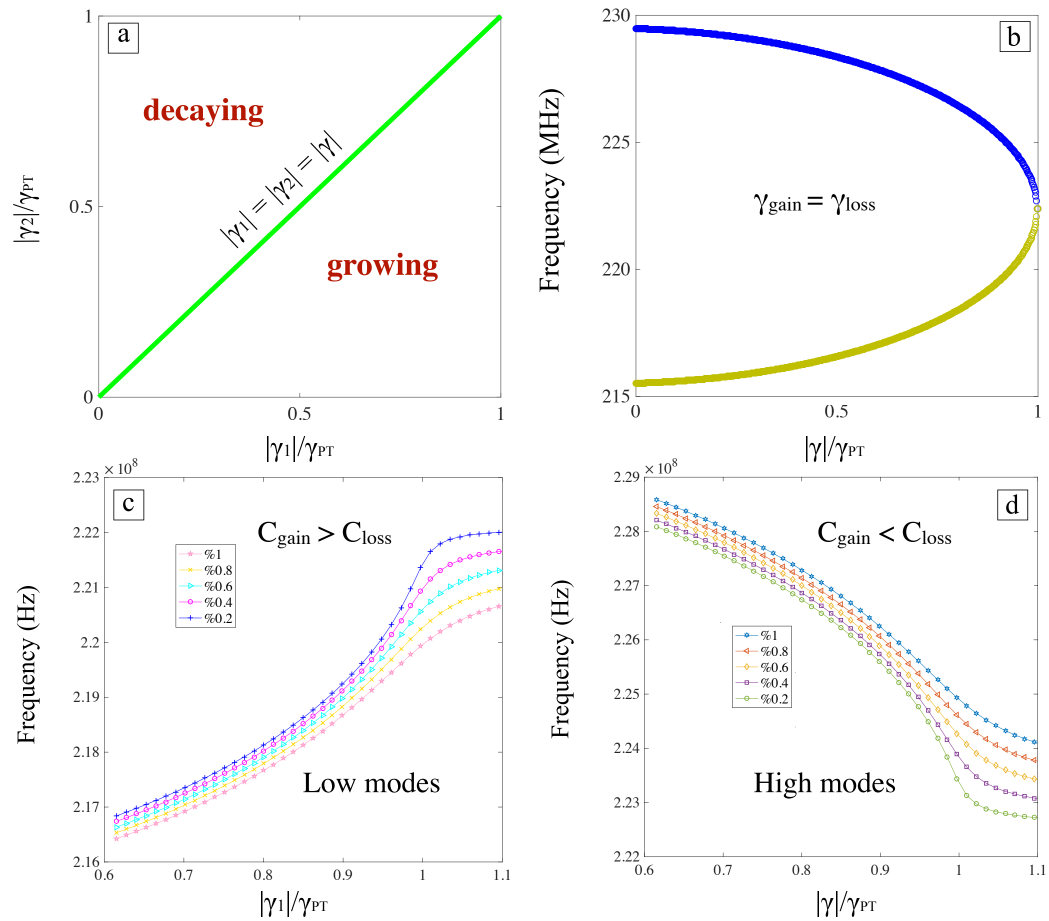

Figure 2.6: Exact phase regime in a PT dimer. When the frequencies of individual oscillators are the same and the amount of gain is exactly the same as the amount of loss -gain and loss are balanced- (a), there are two frequencies in the spectrum (b) and the imaginary part of spectrum is zero. When the frequencies of individual oscillators are not the same (c, d), either High or Low mode is dominant in the spectrum of the system. In Figure (c), capacitance of gain side is larger than the capacitance of loss side, while in Figure (d), capacitance of loss side is larger than the gain side. The legends in (c) and (d) show the relative difference in the capacitances of the gain and loss sides.

frequencies in Figure 2.6c. The reference for classifying a mode as ‘High’ or ‘Low’ is the merge frequency at PT point. Two modes merge at frequency of 223 MHz at PT point ($\frac{\gamma}{\gamma_{PT}} = 1$) in Figure 2.6b.

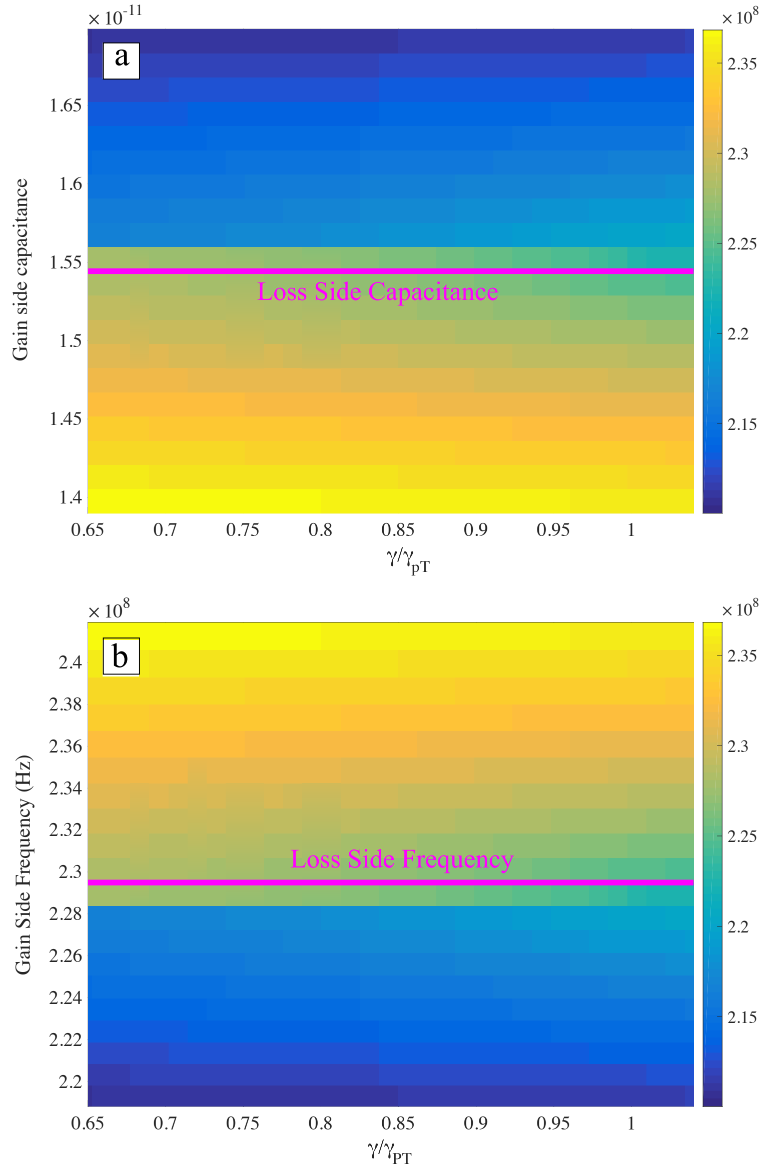

Figure 2.7: (numerical data) Spectral density plots for Re (ω). Pink solid line shows the capacitance (frequency) of loss side in a (b).

The density plots in Figure 2.7(a, b) show the dominant frequency in the dynamics of the system for each value of γ. In these figures, the inductors of gain and loss sides are the same but capacitances are different in (a). Having different capacitances leads to different frequencies (b). The pink solid line in both figures shows the PT condition, where the capacitance (frequency) of gain side is exactly the same as its pair in loss side. Figures 2.7a,b working like maps to tell us how far the system is from being a PT symmetric. For any value of γ, by measuring the dominant frequency in the spectrum of the system, one can tell what is the capacitance and frequency of the gain side and how far we are to get to the PT point.

Since there is no MOSFET in the loss side, calibrating γ before coupling can be used as a reference. In addition, soldering adds some loss to the calibration, but this extra loss appears as a constant and later during data fitting we will be able to find the extra loss constant. Figure 1.18 shows the relation between the computer-controlled voltage and the γ value in the loss side. Figure 2.8 shows frequency versus γ in the loss side. Although the frequency of loss side does not stay constant for different γ

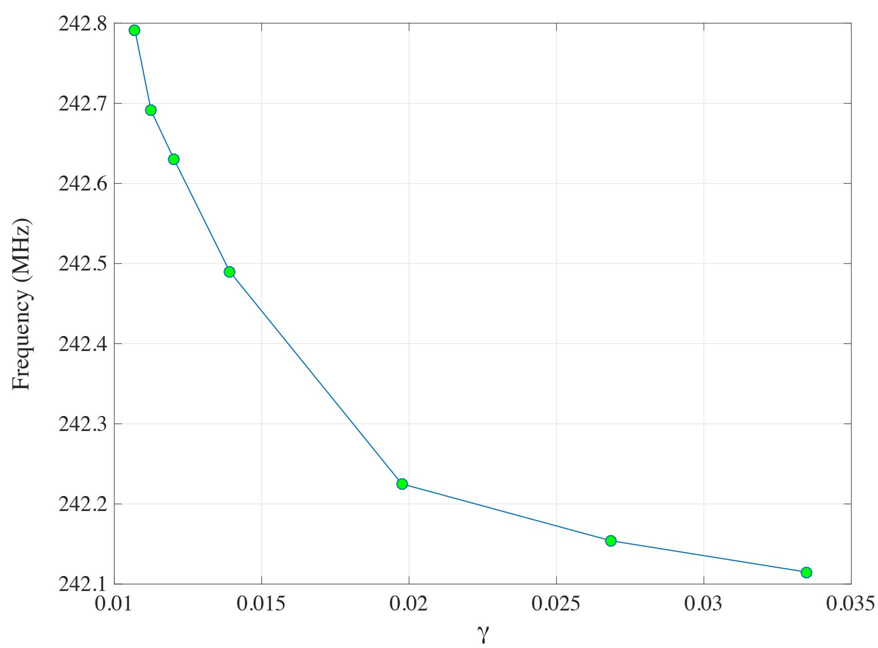

Figure 2.8: (Measure data) Frequency of loss side vs γ. Data are obtained by using the Phase-comparison method.

values (the rate of frequency change in the loss side is much smaller than the gain side, it changes by less than 0.7 MHz for the γ range shown in the figure), we do not need to know the exact frequency for each γ value. The Self-Balance technic compares the parameters in gain and loss side and without actually measuring them, makes them balanced.

In order to tune frequencies and γs in both sides, we have the freedom to change two parameters in the gain side. The first one is the voltage applied to LED which corresponds to the level of light and gain value. The second one is the voltage across the tuning varactor which corresponds to the capacitance of tuning varactor and frequency of gain side.

When the voltage across the tuning varactor is 30 Volts, it has its lowest capacitance (Figure 1.19), and the gain side has the highest possible frequency and vice versa, when the voltage is 3 Volts (we avoid running the varactor with voltages less than 3 volts to prevent any possible dissipation from the oscillator via tuning diode), the capacitor has the highest possible value and frequency of the resonator is the lowest.

Fine calibration between the two sides will be done with the computer by adjusting the γ and frequency parameters. However, before doing the fine calibration, we must make sure that for the γs in the desired range, when the voltage across the tuning varactor is 30 Volts, the dominant frequency in the dimer output is the high mode. Conversely, when the voltage is 3 Volts, the dominant frequency should be the low mode.

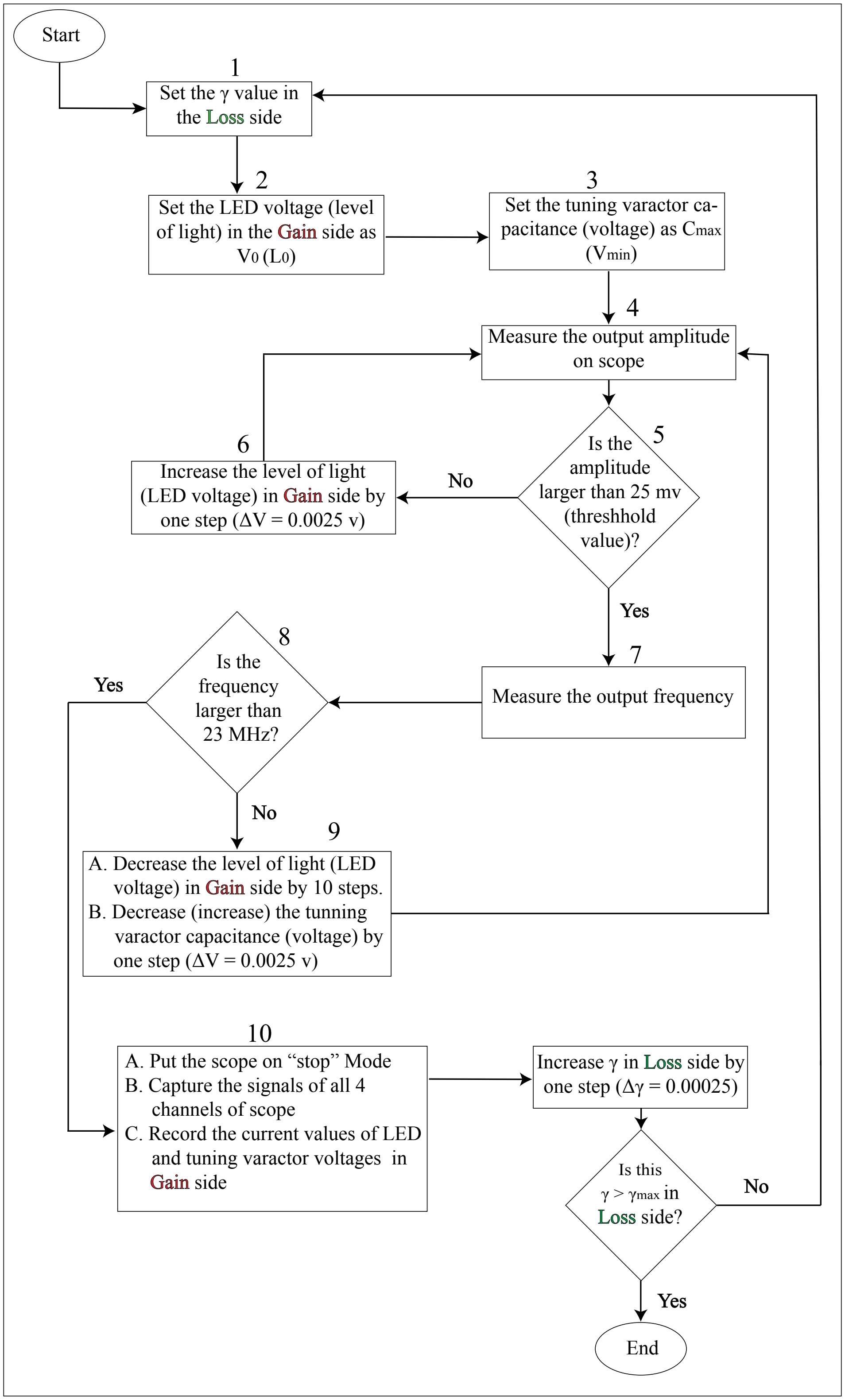

Figure 2.9: Computer-controlled Self-Balancing method flowchart.

Therefore, we know that there is always a point in the range of 3 to 30 Volts where both frequencies co-exist. Before this point, low mode is dominant and after that point high mode, and exactly at that point both frequencies co-exist. This identifies the perfectly balanced point in the exact phase for any γ_{loss}. Following this step, the rest of the calibration is done by computer for any γ value, as shown in a flowchart in Figure 2.9. The calibration steps are summarized here:

1- First step is to set γ in the loss side. For any γ value, program will calculate the suitable DAC voltage (Figure 1.18) and set the level of light in the loss side.

2, 3- The level of light in the gain side is set at a low level to keep the amplitude of the system under the threshold value of 25 mV (please see section 2.4 for details about the gain side detector). Usually at this point the voltage across the LED is set to 1.7 Volts. The voltage across the tuning diode is set to 3 Volts, so that the gain side has its lowest possible frequency. This frequency is less than the frequency in the loss side.

4, 5, 6- During the steps 4 and 5, the program keeps increasing the level of light in the gain side until the output voltage passes the threshold value. In each step the DAC voltage is increased by 0.0025 Volts.

7, 8, 9- At threshold, when finally there is a signal detected on the scope, its frequency is measured; if frequency is less than 23 MHz , it means that the low frequency is still dominant. Still, the frequency of gain side is lower than the frequency of loss side, and voltage across the tuning varactor bias needs to be increased. The merged frequency at $\gamma = \gamma_{PT}$ is 223 MHz, since the frequency is mixed down by 200 MHz (see section 2.4 for more details), the reference for having lower or higher mode is 23

MHz. Before increasing the diode voltage, signal needs to be killed (set under the threshold value) to avoid having any hysteresis effect in reading the frequency. The varactor bias voltage is then increased by 0.0025 Volts.

10- When finally the dominant frequency (the frequency which is read by the scope after signal passes the threshold) switches from low to high, we define where frequencies of gain and loss are the same and gain and loss parameters are equal as the PT point. The oscilloscope mode is set to 'Stop' mode. Now all the channels will stop at the same time. Channel one is connected to the gain channel, channel two is connected to the loss channel, and channel 3 is connected to the function generator which provides the time dependent function for the coupling network. After all the channels saved, scope changes to the 'run' mode and all of the above steps will be repeated for the next value of γ, until the last value of γ in the range has been measured.

An extrapolation method is used to measure the dynamics of points related to γ values out of the exact phase regime (broken phase regime). Figure 2.10a, b show the values of voltage across the LED in the gain side (a) and the voltage across the tuning diode (b) as a function of γ. In other words, moving from one gamma value to the next, these parameters need to be set as in Figure 2.10 in order to move on the PT line and have everything balanced. For this set of data γ_{PT} happens at 0.065. For points very close to and after this value, I linearly extrapolate in both diagrams.

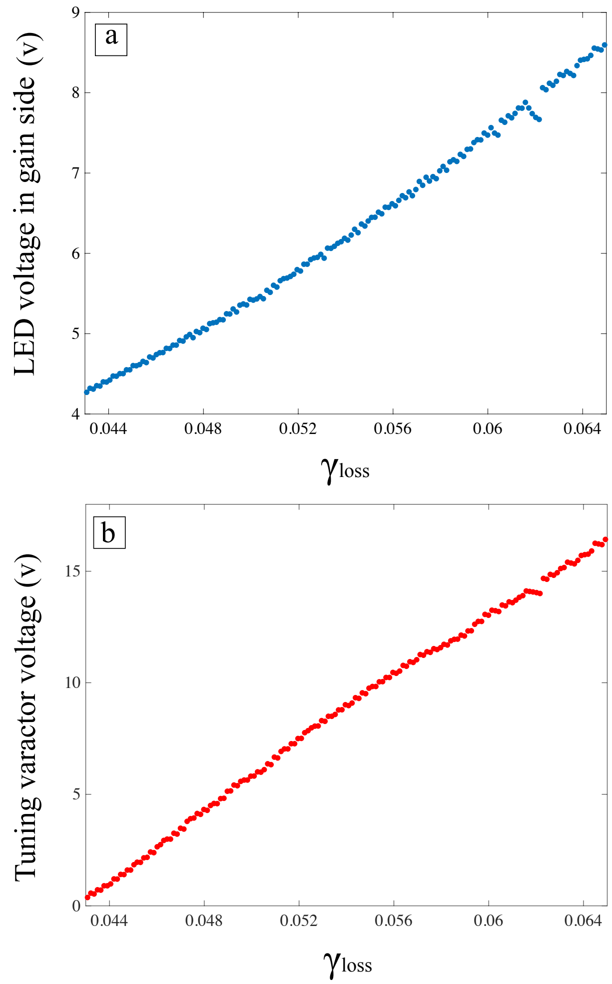

Figure 2.10: The tuned value of LED voltage located in gain side (a) and tuning varactor voltage for one set of data.

2.3 The Phase Comparison Method

The phase comparison method is used for measuring the frequency and γ value (decay rate) of individual oscillators and coupled frequencies of coupled resonators. A block diagram of the measurement set-up is shown in Figure 2.11.

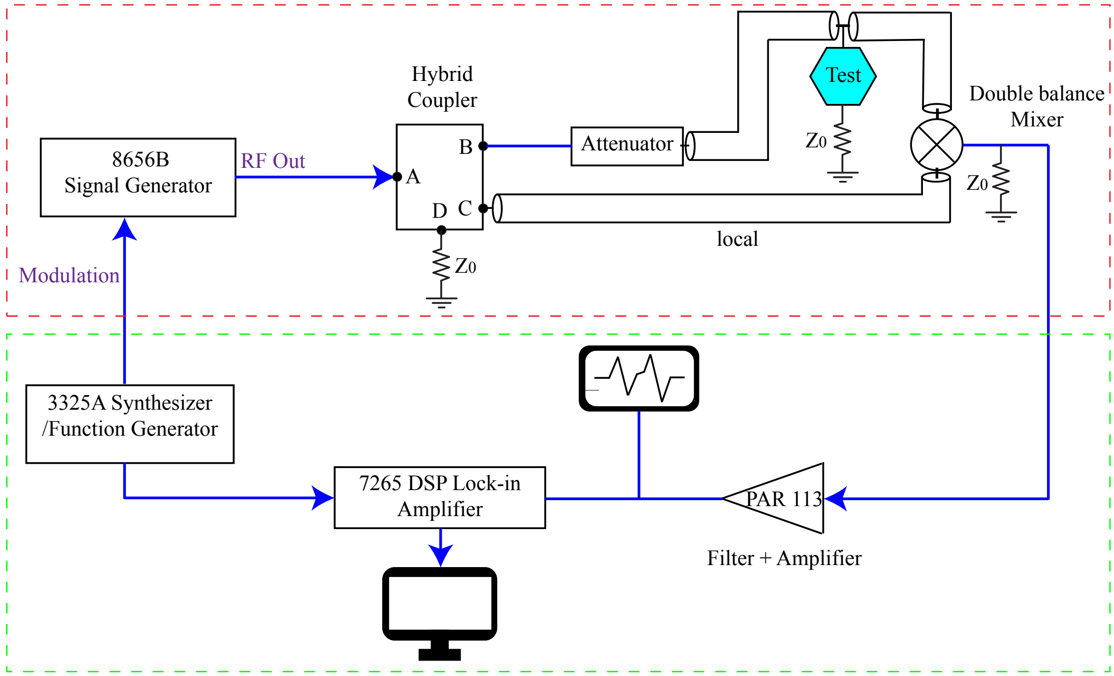

Figure 2.11: Block diagram of the phase-comparison method.

The whole procedure can be divided into two parts: The "lock-in detection" which includes the steps boxed by dashed green color, and the "phase difference modulation" which includes the steps in dashed red box.

The frequency of RF signal which is provided by the HP8556B signal generator is externally modulated up-and-down by 20 kHz (DC-FM Modulation). The frequency of this up-and-down modulation is provided by the HP3325 synthesizer set at 1 kHz. The resulting 7 dBm modulated output signal is split in two 3 dBm signals in a 90 degree splitter. The first signal (the signal exiting from port B) after going through the attenuator passes by and interacts with the test resonator. The attenuator blocks any reflected signal from going through the splitter and also attenuates the amplitude of the signal to keep it from saturating the resonator. The signal is induced in the inductor by a loop attached to the end of the coaxial cable located in the vicinity of the inductor (about 0.5 centimeter apart) and then will be picked up by another pick up loop attached to another coaxial cable near the other end of the inductor (about 0.5 centimeter apart).

In the double balance mixer, the local signal is multiplied by the signal received from the box (the "test" box with oscillator). The mixer is used here as a phase comparator. The output signal from the mixer has the frequencies at the sum and the difference of the local and the received signals; but only the frequency of difference gets amplified. On the other hand, since the local signal and the signal received from the box have the same frequencies, only their phase difference which is caused by the resonator in the box gets amplified. The frequency modulation results in a phase modulation of the RF signal, only near resonant with the "test" box.

The rest of the process is the "lock-in detection". A lock-in amplifier is referenced to the 3325A synthesizer and measures the amplitude and the phase of the difference signal. As the frequency of the HP8556B is scanned through the "test" resonator, the lock-in response records a signal encoding the resonance. The result which shows the derivative of the phase difference of the two signals with respect to the frequency, is fitted to obtain the frequency and γ of the "text" box.

Figure 2.12a, b show the results of phase comparison scanning of two different single oscillators, whereas Figure 2.13 shows the coupled frequencies of two LRC oscillators coupled together by a varactor network. The numbers written on top of each set of modes in Figure 2.13 indicate the DC voltage applied to the varactor

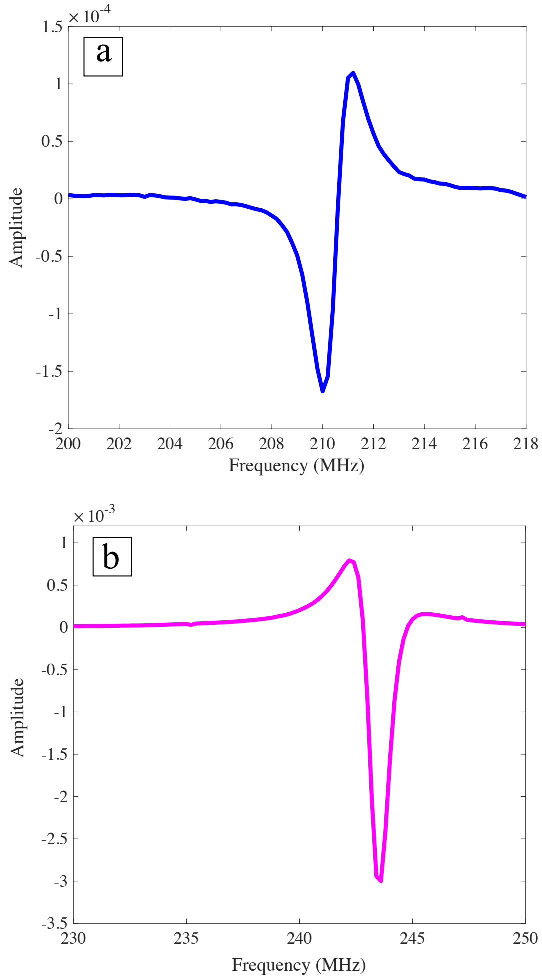

Figure 2.12: frequency scans of two different single LRC resonators by phase-comparison method.

network (AC voltage is off during these measurements). Figure 2.13 shows the effect of varying the coupling between oscillators on the coupling frequencies.

A number of things must be considered while using this method:

1. This method is only useful for scanning oscillators with loss. So, it can not be used for the gain side with gain. However, it can be used to measure the

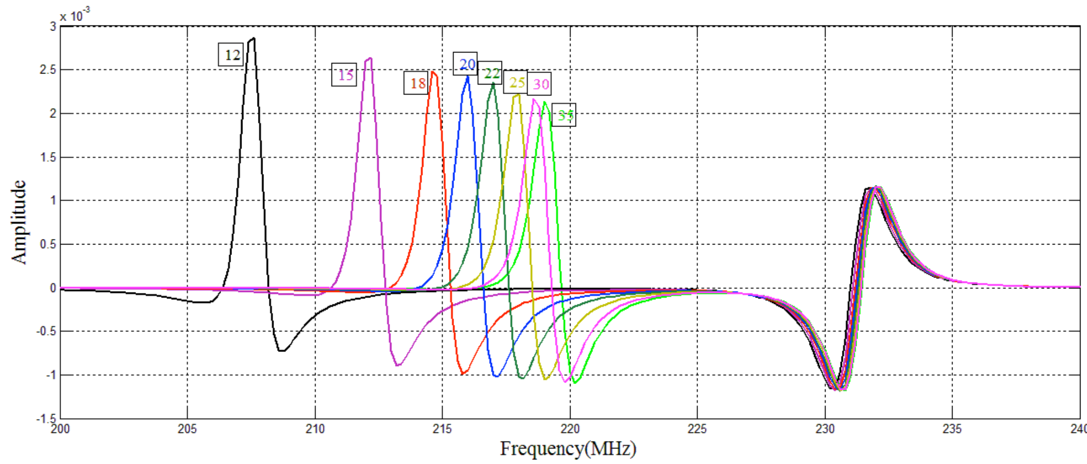

Figure 2.13:The scanned resonances by phase-comparison method for a coupled of oscillators.

frequency and γ in the gain side in the beginning to measure the natural loss and the natural frequency of oscillator.

2. The phase comparison method can not be used when the quality factor of the system is very low ($Q = 1/\gamma$). For a very lossy oscillator when the resonance amplitude gets close to the noise level of the set-up, the result is not trustable anymore. This method could not be used for oscillators with quality factor less than 20.

3. Also, the method is not useful and accurate, when there are extra modes in the vicinity of the main resonator mode (Figure 2.14). The only use of the phase comparison method in this situation is showing the existence of those additional frequencies. The source of those frequencies needs to be found and eliminated.

4. This method can be used for gain side after some modifications. As we go to higher γ values in the gain side, a parallel resistor (its corresponding γ value needs to be larger than the oscillator gain) is added to the oscillator. The oscillator

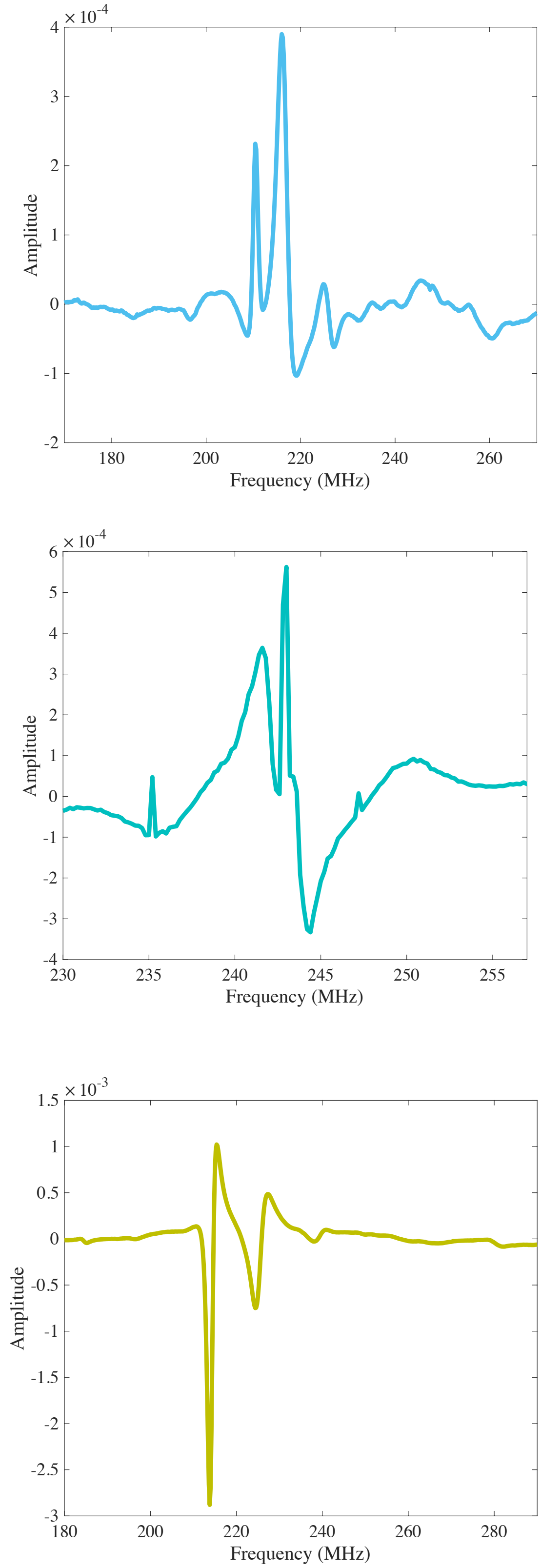

Fig 2.14: Scans obtained by using phase-comparison method which due to practical limitations can not be used.

becomes lossy, so this method can be used to measure the frequency and γ. The difference between the γ obtained from scanning and the γ related to the parallel resistor is the value of gain in the gain side. However, since this method requires using the soldering iron, attaching and removing the parallel resistor can create lots of errors.

5. The internal 20 MHz modulation frequency can be less than 20 MHz for smaller γ values (high quality factors).

Figure 2.14 shows several scans obtained by the phase comparison method, which cannot be used because of the above mentioned issues.

2.4 Signal acquisition

Figure 2.15 shows the remainder of the signal acquisition set-up.

The gain and loss sides are isolated from each other. The excitation in each resonator is sensed by a small pickup loop attached to the input of a Mini circuits ZPL-1000 low noise amplifier (this step denoted as number 1 in Figure 2.15).

The amplified signals leaving the dimer box have the frequencies of ≈230 MHz. Next, heterodyning technic (denoted as step 2 in Figure 2.15) is used to create ≈30 MHz signal from ≈230 MHz output . The 8656B signal generator produces a 200 MHz signal with amplitude of 10 dBm. The splitter divides the 200 MHz signal into two 7 dBm signals. Each of these signals is being used in the local port of the mixers.

Heterodyned signals contain ≈430 MHz and ≈30 MHz frequencies. The 430 MHz signal is filtered and the ≈30 MHz signals are captured by a Tektronix

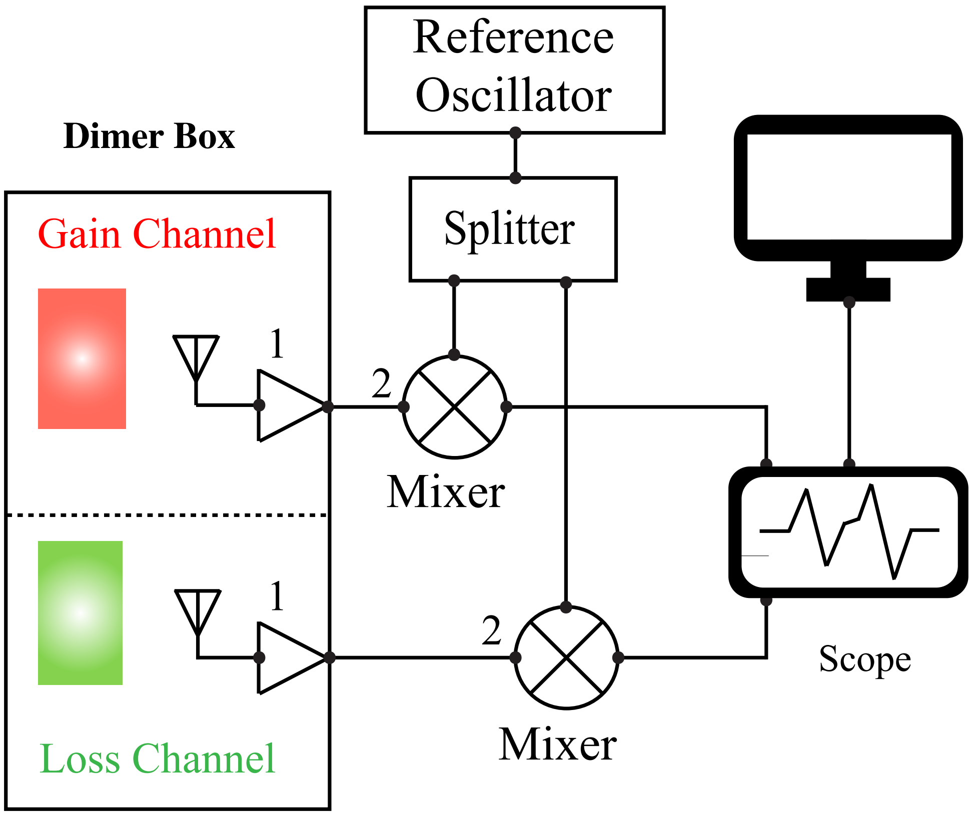

Figure 2.15: The remainder of the signal acquisition set-up

DPO2014 oscilloscope. The 30 MHz signals have all of the properties and sidebands of the original frequency, with fewer points and slightly smaller size. Figure 2.16 shows the mixers used in the gain and loss channels.

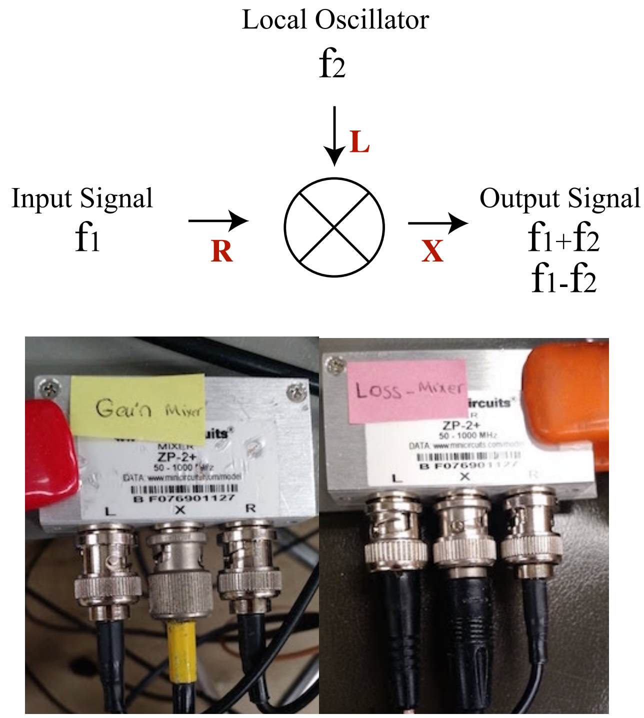

Figure 2.16: Heterodyning technic. Signals obtained from antennas in gain and loss sides are mixed with the 200 MHz signals coming from signal generator. Output signal X has all of the properties and side bands of the original signals with less number of points and smaller size.

Chapter 3

Results

This Chapter will summarize the experimental results for a periodically driven PT symmetric system.

3.1 Looking for "Bubbles"

Numerical and theoretical analysis had predicted the existence of localized islands of instability in the imaginary part of the spectrum of a driven PT system. The driven coupling is described as $c = c_0 + \varepsilon \cos(\omega_m\tau)$, where the first term c_0 describes the constant background coupling, and the second term refers to the periodic driving part which changes as a function of time with amplitude ε and frequency of ω_m.We have referred to these islands of instabilities as "the bubbles" from the very beginning of the project. Having these localized instabilities are very interesting, especially in the exact phase of the spectrum, where the imaginary parts of eigenfrequencies are zero in an undriven case (Figure 3.1).

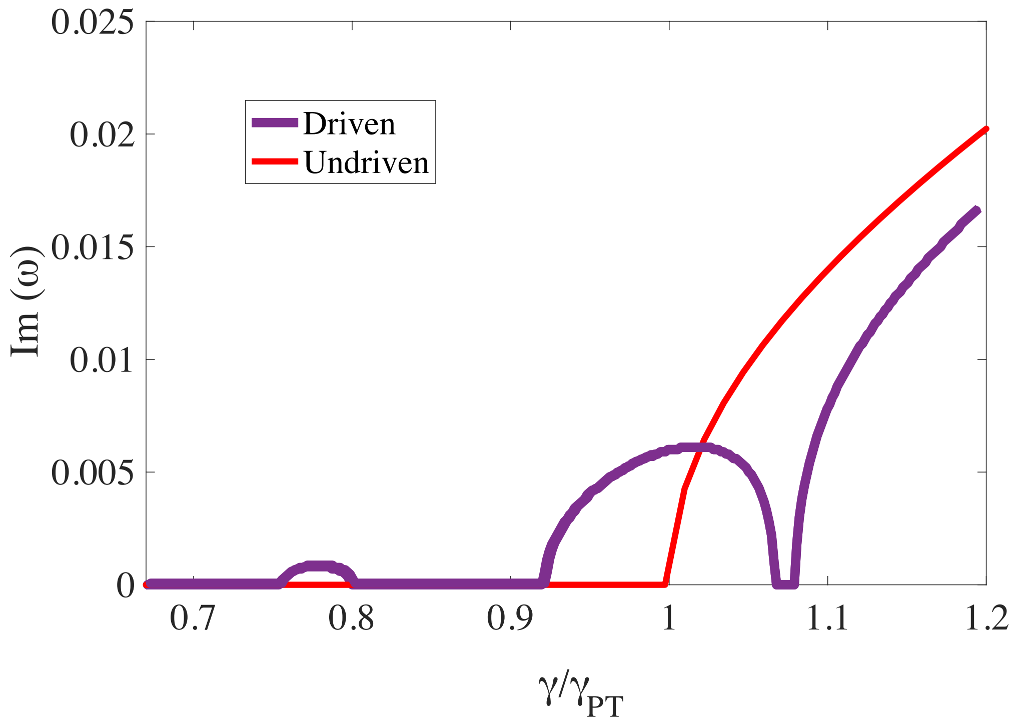

Figure 3.1: (Numerical data) localized islands of instabilities in the imaginary part of the spectrum of a driven PT system.

To investigate the size and the dynamics of these bubbles, first we need to localize them precisely. We need to be sure that based on the limitations we have in choosing the parameters such as the amplitude and the frequency of modulation drive, size of the bubbles are large enough to be observable by the resolution of our detection scheme.

In a brute-force way, we could perform all the 11 steps of calibration (see the calibration section) and take data for a wide range of γs, drive frequencies, drive amplitudes, coupling varactor voltages, etc. and then spend months on analyzing these signals (thousands of signals) to find the bubbles and their other

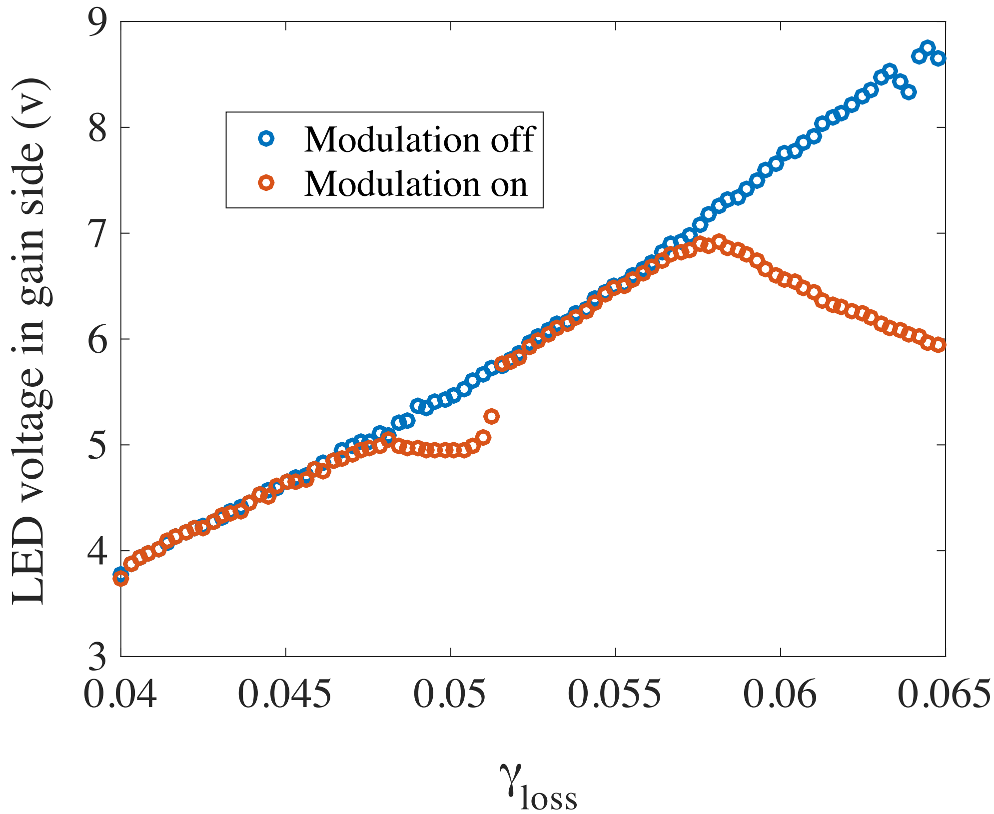

Figure 3.2: (Measured data) Proof of having islands of instabilities (extra gain) in the spectrum of a driven PT system. For ω_m = 4.6 MHz and amplitude of 0.1 pF. (see section 3.1.1 for the reasons behind choosing these numbers for the frequency and the amplitude)

characteristics; . However, a better way was to find the parameters and γ ranges which include observable bubbles and then capture the signals and perform all the analysis.

By choosing the second method, for each γ value the first 10 steps of calibration is done and when finally the dominant frequency (the frequency which is read by oscilloscope after amplitude of the output signal passes the threshold value) switches from low to high, we define that point as a PT point. At this point frequencies of gain and loss are the same and gain and loss parameters are equal, and the experiments

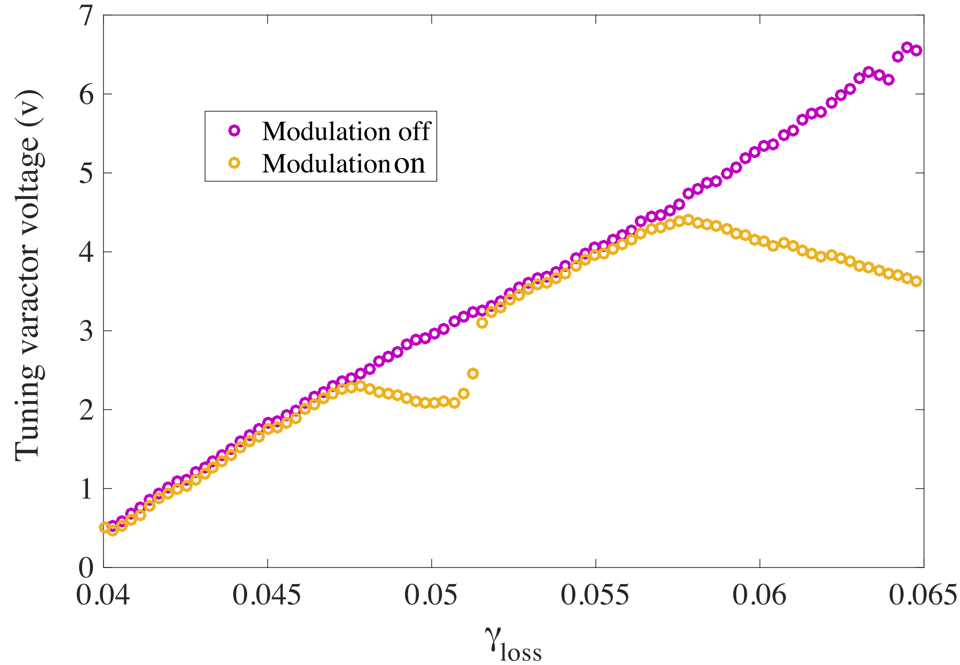

Figure 3.3: (Measured data) For the parameters $\omega_m = 4.6$ MHz and amplitude of 0.1 pF. Signal passes the threshold while gain side needs to provide less gain than non driven case. When gain value is different, tuning capacitance also would be different.

stopped. All the PT parameters such as tuning varactor voltage and LED voltage in the gain side will be recorded for the desired γ range.

These steps will be done once with the modulation and another time without it. And with no need for any further analysis, the calibrated value of LED voltages in the gain side will be compared in these two cases.

In the case of having islands of instability in the spectrum of a driven system, there should be localized islands of extra gain. So, to get to the threshold point, gain side needs to provide less gain than the non driven system. When gain side provides less gain, the tuning varactor voltage is also different. Figure 3.2 and Figure 3.3 show the existence of bubbles in the spectrum. This major breakthrough was observed the for the first time on April 10th 2016.

3.2 Experimental Results

This section will summarize the experimental results obtained for a periodically driven PT symmetric system. The results are also compared with the undriven case. [8]

3.2.1 Undriven system

The set-up is similar to Figure 1.2, it consists of two coupled LC resonators with balanced gain and loss. The capacitance that couples the two resonators can parametrically be modulated with a network of varactor diodes.

In order to compare our data with previously published theoretical and tested unmodulated results, and more importantly to balance and calibrate both the oscillation frequencies and the gain/loss values in the experimental set-up (it is discussed in details in section 2.2), the experimental undriven PT diagram will be investigated first.

With the modulation off, a pre-calibrated γ parameter (the loss value) on the loss side is set. The gain side γ parameter (the gain value) is then adjusted at each of these values for threshold, assuring PT-balance for each chosen gain/loss parameter value. A transient time-domain trace is then obtained simultaneously for both the gain and loss side LC nodes. The transient time-domain traces are obtained from antennas in the loss and gain sides for $\gamma = 0.0483$, are shown in Figure 3.4 (a, b) for 4 μs.

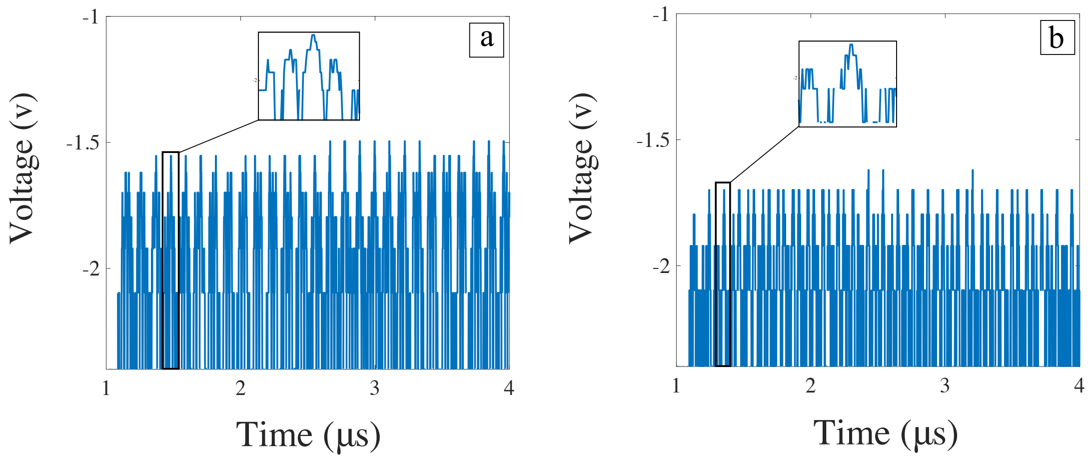

Figure 3.4: (Measured data) Voltage as a function of time in the unmodulated system for γ = 0.0483 is achieved from antenna in the (a) loss side and (b) gain side. (logarithmic y axis)

The real and imaginary parts of the eigenmodes are obtained and analyzed differently. The real parts of the frequencies in Figure 3.5 (a, b) are shown as density plots of the data in the frequency domain. The abscissa (γ/γ_{PT}) values were stepped with approximately 175 values across the range of γ = [0.042 0.068] (γ/γ_{PT} = [0.065 1.04]). These steps can be seen better later in Figure 3.8 as slight discontinuities in the brightest spectral components visible. Each of these steps corresponds to a captured trace.

The Fourier transform of each trace represents the spectral constituents of the transient response at the associated γ/γ_{PT} value. Dominated by the oscillatory response, the transform magnitude peaks indicate the real part of the constituent frequencies. This transform magnitude is plotted as a color-map with approximately 3000 points along the ordinate.

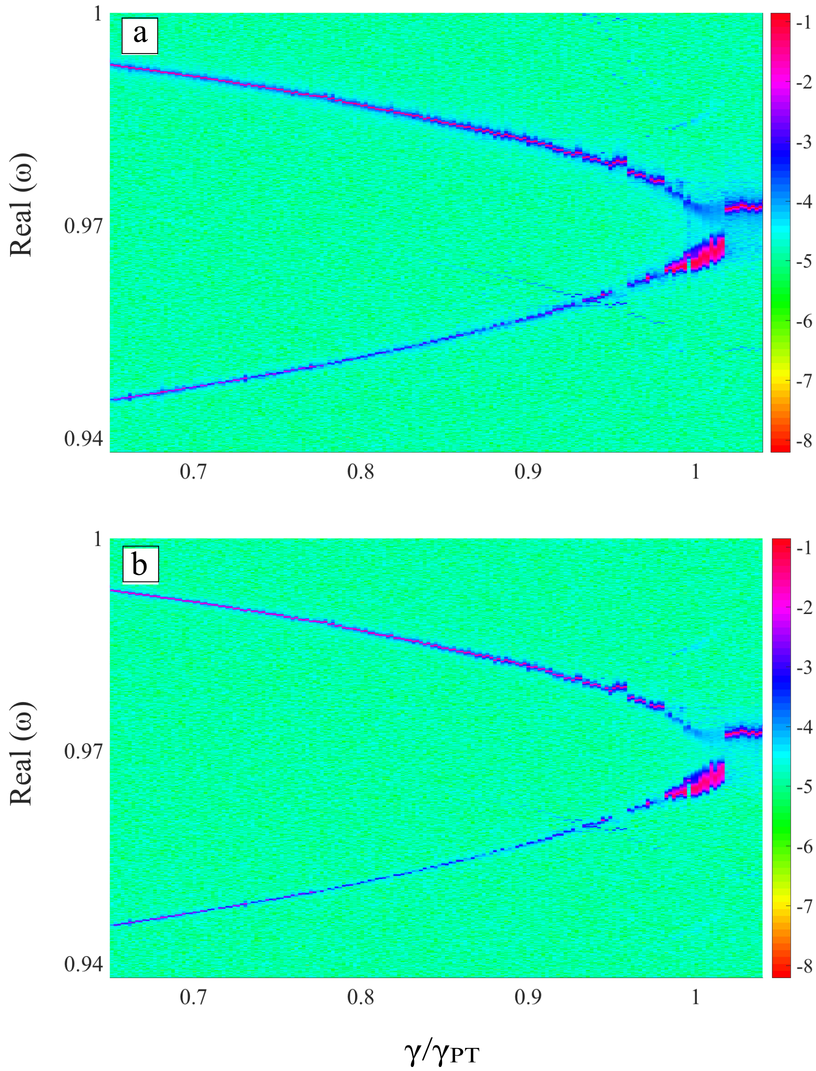

Figure 3.5: (Measured data) Spectral density plots for R$e(\omega)$ of an undriven PT-symmetric dimer, which are obtained by analyzing 175 transient traces corresponding to 175 scaled gamma parameters in the range of 0.65 to 1.04 achieved from antenna in the (a) loss side (b) gain side.

The color maps shown in Figure 3.5 (a, b) indicate the experimental results of the spectrum of the undriven dimmer. The spectrum is divided into two domains of exact ($\gamma < \gamma_{PT}$) and broken ($\gamma > \gamma_{PT}$) PT -symmetry phase.

Plots in Figure 3.5, Figure 3.7 , and Figure 3.8 therefore indicate a non-selected mapping of any frequencies present over all of the orders of magnitude in amplitude within the accompanying color-map scale. Plots have the color-map scales extending into the noise-floor, or “grass” of the transform.

The imaginary part of eigenfrequencies in the undriven system is presented later with the results of the driven case.

3.2.2 Driven system

For any specific gamma value, after capturing the traces, the coupling is then modulated, directly comparing each calibrated point with and without the modulation. Again the captured signals are frequency-analyzed to obtain the modulated (or unmodulated) spectrum, shown in Figure 3.7 (a, b).

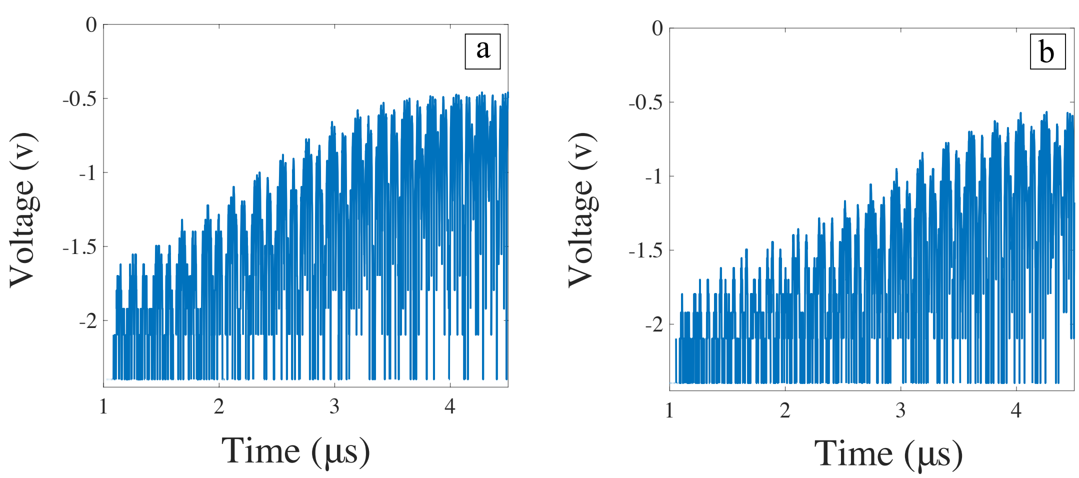

Figure 3.6: (Measured data) Voltage as a function of time for modulated system for $\gamma = 0.0483$ is achieved from antenna in the (a) loss side and (b) gain side. (logarithmic y axis)

The transient time-domain traces which are obtained from antennas in loss and gain side are shown in Figure 3.6 (a, b). These traces are captured right after the modulation is turned on following the data acquisition in the unmodulated system

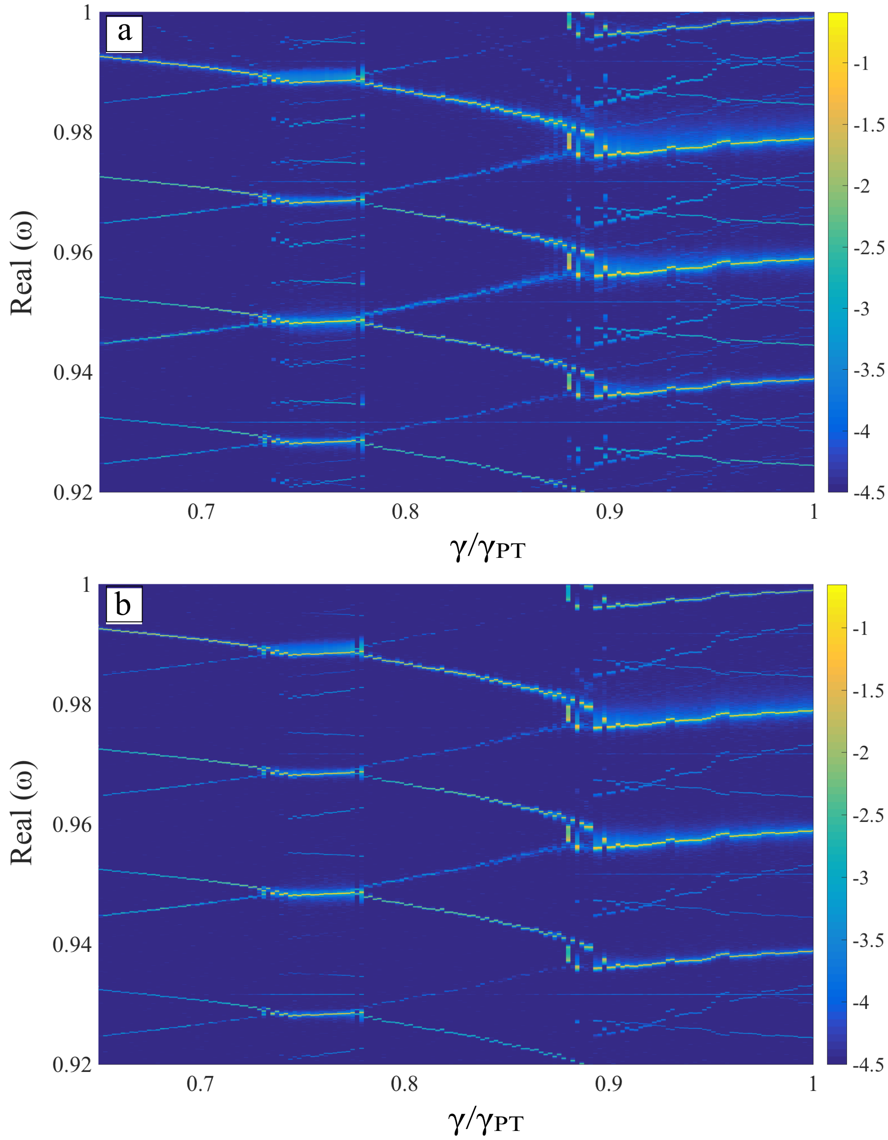

Figure 3.7: (Measured data) Spectral density plots for R$e(\omega)$ of driven PT - symmetric dimer with $c_0 = 0.0671$, $\varepsilon = 0.01$ and $\omega_m = 0.0198$. These plots are obtained by analyzing 175 transient traces achieved from antenna in the (a) loss side (b) gain side.

with the traces shown in Figure 3.4 (a, b). Modulated coupling with the amplitude of $\varepsilon = 0.01$ and frequency of $\omega_m = 0.0198$ will change the unmodulated system traces, shown in Figure 3.4 (a, b), to the traces shown in Figure 3.6 (a, b).

At about 3 μs, the voltages start to saturate. To analyze and calculate the imaginary parts of eigenfrequencies, only the transient section before the saturation is used. Analysis of the real parts of the frequencies is presented with the color-map in Figure 3.7 (a, b). To obtain these plots, 175 traces like the one shown in Figure 3.6 are processed. These traces have the same amplitude and frequency of modulation.

The color scheme of plots in Figure 3.7 are different from those in Figure 3.5, they are modified to enhance the contrast of the dominant frequencies present.

3.2.3 Comparison and new features

The numerical findings together with the experimentally measured real and imaginary parts of frequencies versus the gain/loss parameter are reported in Figure 3.8 (a-c) and Figure 3.9 (a-f).

In all cases in Figure 3.8, the white, open circles correspond to the eigenfrequencies obtained from the numerical simulation. The experimental eigenfrequencies (real part) are the corresponding most intense bands seen in the transform maps. The additional spurious bands, particularly visible in the broken-phase regions, are various sums and differences primarily introduced due to our frequency conversion detection scheme.

Single light-blue solid circles in Figure 3.9 (a-f) representing the exponential growth rate of the 29 captured transient traces of 29 specific gamma parameters, as

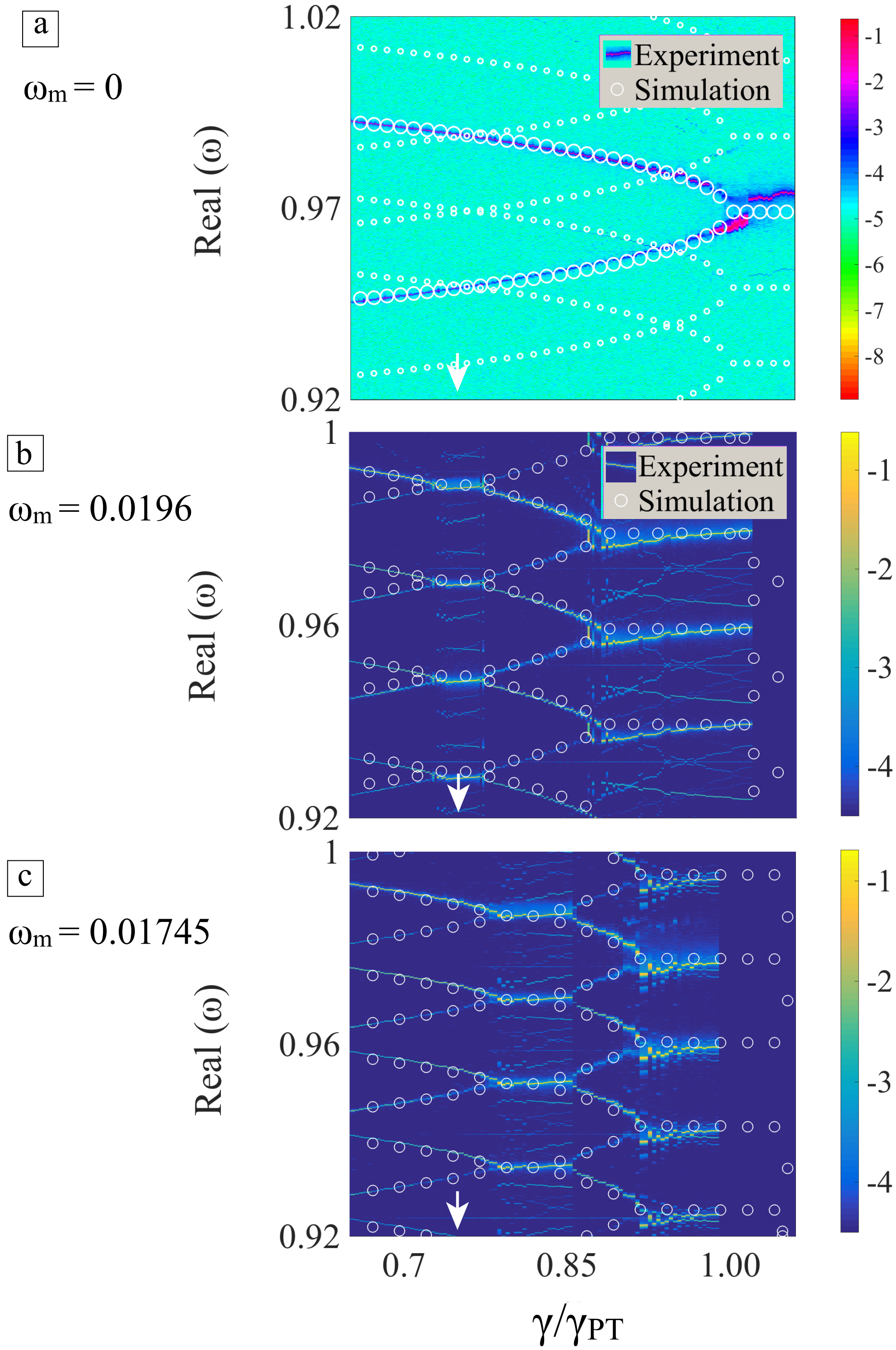

Figure 3.8: Spectral density plots for R$e(\omega)$ of a driven PT-symmetric dimer with c_0 = 0.0671 and ε = 0.01: (a) Undriven dimer ε = 0. numerical findings associated with the eigenfrequencies is indicated by the white circles (here $\omega_m = 0.0198$); (b) The crossing points "evolve" to flat regions when the system is driven; (c) Using a different driving frequency ω_m = 0.01745 leads to a shift of the flat regions to different γ-domains. The white circles in (b, c) indicate numerical data.

analyzed by direct fitting. In this case, only a sampling of the traces were analyzed, separately optimized to ensure the validity of the extracted growth rates well away from the detection system saturation.

The unmodulated situation is shown in Figures 3.8 a and 3.9 a, while Figures 3.8 b and 3.9 b show the behavior at modulation frequency $\omega_m = 0.0198$ and modulation amplitude $\varepsilon = 0.01$. Figures 3.8 c and 3.9 f show the evolution of the spectrum with a small change in modulation frequency $\omega_m = 0.01745$ for fixed $\varepsilon = 0.01$. In Figures 3.9c and e, the imaginary part of spectrum for two other modulation frequencies between 0.0198 and 0.01745 is plotted; Figures 3.9 (b-f) altogether show the evolution of the so-called unstable "bubbles" for fixed $\varepsilon = 0.01$ and fixed $\gamma = 0.0483$ (marked by black arrow).

There are several new features in the spectrum of the driven PT-symmetric systems. First we see that there exist a cascade of domains for which the driving system is in the broken PT-phase. These domains emerge as shown in Figures 3.8b and c where the real parts of eigenfrequencies have merged in the vicinity of the crossing points (indicated by the arrows) and in Figures 3.9 (a-e) the non-zero imaginary parts ("bubbles") appear. Both the size and position of the unstable "bubbles" can be controlled by the values of the driving amplitude ε (compare Figures 3.8a and 3.9a with Figure 3.8b and 3.9b), or by the driving frequency ω_m (compare Figures 3.8b and 3.9b with Figures 3.8c and 3.9e). Between the nearest bubbles, there exist γ-domains where the system is in the exact (stable) PT-phase. Through the typical EP degeneracy, the transition between stable and unstable

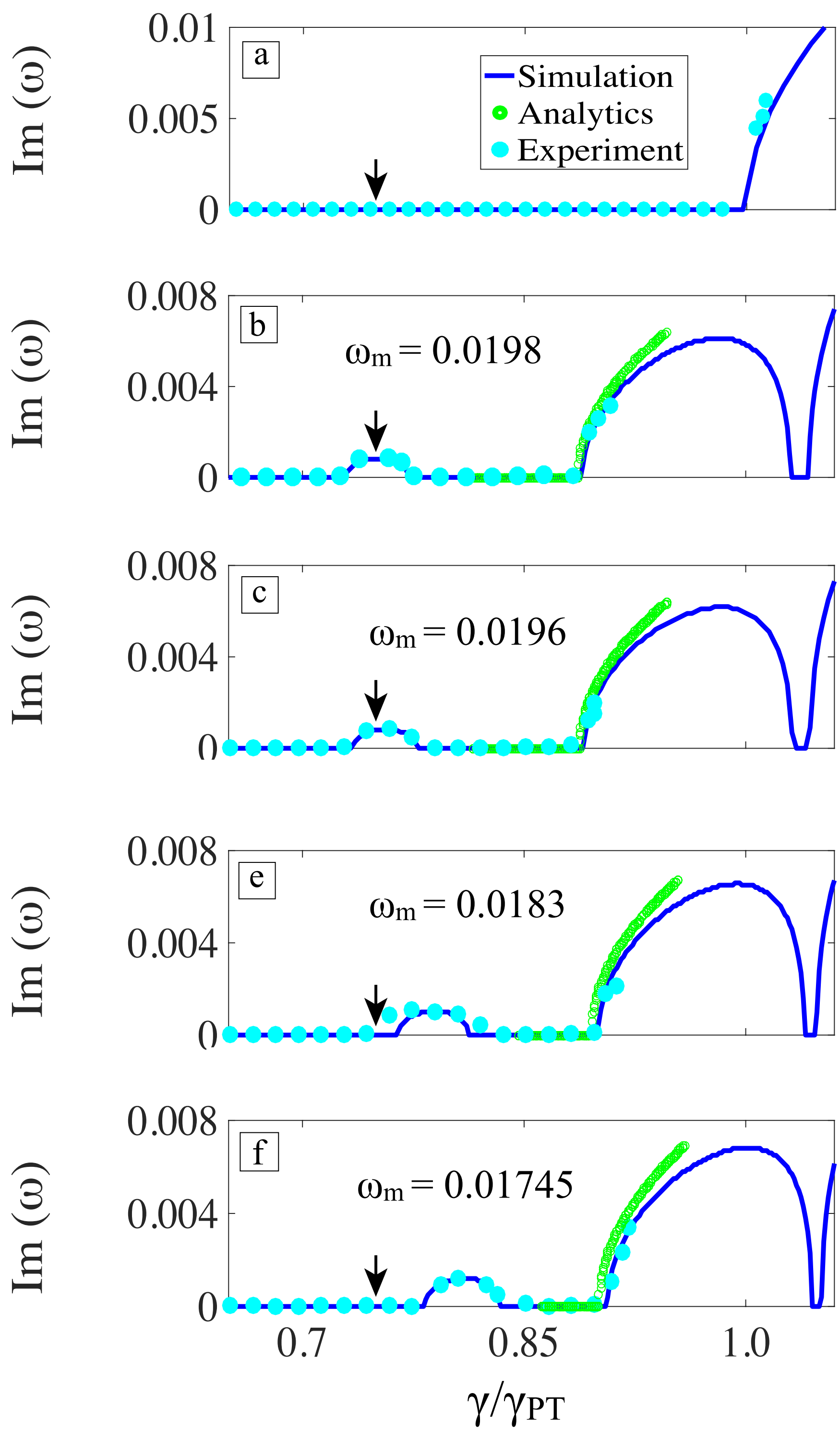

Figure 3.9: The imaginary part of the eigenfrequencies I*m*(ω)versus the rescaled gain/loss parameter for: (a) an undriven; and (b, c, e, f) driven dimers, with ω_m shown. The arrows corresponds to the fixed crossing points in Figure 3.8a for reference. The experimental data are shown as aqua circles, the numerics as blue lines.

domains occurs. Beyond some critical gain/loss value $\gamma_{\max}$, the system eventually becomes unstable. The $\gamma_{\max}$ is defined as the maximum value of the gain/loss parameter, above which there are no further stability domains. Generally $\gamma_{\max}$ depends on both ε and ω_m. However, in the limit of $\varepsilon = 0$, it becomes equal to γ_{PT} .

After we turn on the driving amplitude ε, the crossing points evolve to broken PT-symmetry regions with respect to gain/loss parameter γ. The centers of the instability bubbles are controlled by ω_m. In addition, the real part of the eigenfrequencies become degenerate for a range of γ-values, Figure 3.8b, while an instability bubble emerges for the imaginary part (Figure 3.9b) for numerical (blue solid lines) and experimental data (filled aqua circles). The transition points from stable to unstable regions have all the characteristic features of an EP.

We find that this driven PT system supports a sequence of spontaneous PT - symmetry broken domains bounded by exceptional point degeneracies. The latter has been analyzed and understood theoretically using an equivalent Floquet frequency lattice with local PT symmetry [8]. The position and size of these instability islands can be controlled through the amplitude and frequency of the driving and can be achieved, in principle, for arbitrary values of the gain or loss parameter.

It is interesting to observe the revival of the exact PT phase around $\gamma/\gamma_{PT} = 1.07$, see Figures. 3.9(b-e). To understand this phenomenon, we realize that for constant ω_m (determining the center of the bubble), the edges of the instability domain are pushed away when ε increases.

3.2.4 Phase diagram

In Figure 3.10, the numerically determined PT-exact (white) and broken (shaded) phases are reported, when γ is fixed at the position of the arrows in the Figure 3.8 and Figure 3.9 plots. In this figure we actually report a summary of PT-exact and broken domains in the parametric (ε, ω_m). It shows the theoretical (ε, ω_m) map of the PT-exact (white) and broken phase regions (shaded) for one value of the gain/loss parameter corresponding to the position of the arrow in the previous plots. The

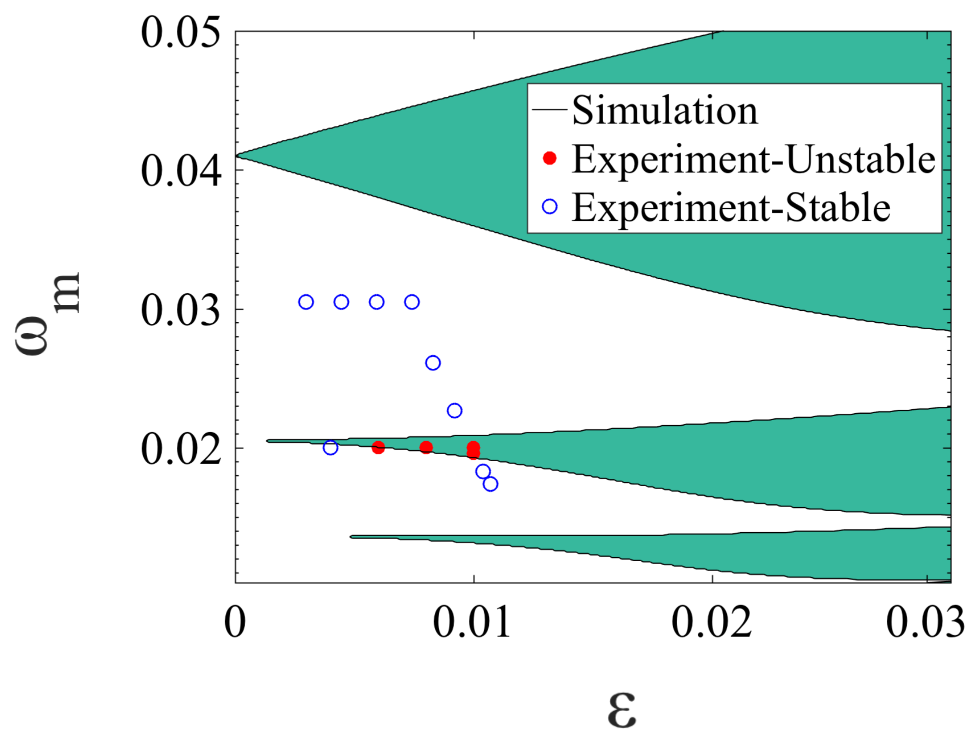

Figure 3.10: The (ε,ω_m) parameter space for fixed γ/γ_{PT} at the position of the arrows in Figure 3.8 and Figure 3.9. The domains where the system is in the exact PT- symmetric phase are indicated as white while the domains where the system is in the broken PT-symmetric phase are shaded.

broken phase is experimentally identified by the global instability growth of the system.

3.2.5 Dynamics

The management of the exact and broken PT symmetry phase, either via the driving amplitude ε or via the frequency ω_m, has direct implications on the dynamics of the system. In Figure 3.11, we report the total capacitance energy of the dimer for the same $\gamma = 0.0483$ and $\varepsilon = 0.01$ values but different driving frequencies $\omega_m = 0.01745$ (left) and $\omega_m = 0.0198$ (right). In the latter case the energy grows exponentially with

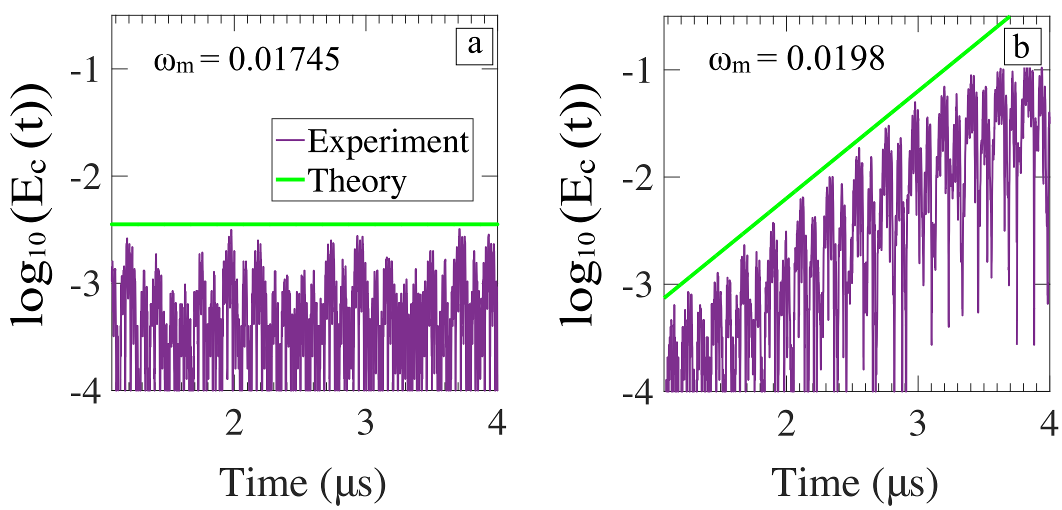

Figure 3.11: (Measured data) time-dependence of the total capacitance energy of the whole circuit $E_C(t) = V_1^2(t)+V_2^2(t)$ (in units of Volt^2) for driving frequencies (a) $\omega_m = 0.01745$ and (b) $\omega_m = 0.0198$, and for the same driving amplitude and gain/loss parameter γ (indicated by black arrow in Figure 3.9(b, c). The green lines indicate the theoretical predictions (from simulations) for the slope of the envelope of $E_c(t)$.

a rate given by the imaginary part of the eigenfrequencies (Figure 3.9b) while in the former case we have an oscillatory (stable) dynamics (see Figure 3.9f).

3.3 Initial Conditions

Theoretically, for a driven PT symmetric system (Figure 1.25), the dynamics for the voltages V_1 (V_2) of the gain (loss) side can be obtained by numerically solving the equations (1.1) and (1.2) while the driven capacitive coupling is given as $c = c_0 + \varepsilon \cos(\omega_m \tau)$. Solving the set of four differential equations requires initial conditions for the currents in the inductors I_{10} (I_{20}), and the voltages V_{10} (V_{20}) in the capacitors of the gain (loss) side. The choice of initial conditions has a direct impact on the dynamics of the voltages V_1 and V_2. Figure 3.12 shows the dynamics for the voltages V_1 and V_2 for two different sets of initial conditions.

However, experimentally we have no control over the initial conditions (I_{10}, I_{20} , V_{10}, V_{20}) for a driven PT system. As it was discussed in pulsing section, the voltage applied on the drain pin of MOSFET located in the gain side changes from 0 to 12 Volts in about 9 s and during this time, initial conditions (currents in inductors and voltages in capacitors) are randomly chosen by the system due to the timing uncertainty of pulsing.

To determine the initial conditions for each set of signals obtained from the antennas in the gain and loss sides, numerical solutions obtained by solving equations (1.1) and (1.2) are first post-processed by the same steps which are performed on the original experimental signal during the signal acquisition process, recall that this

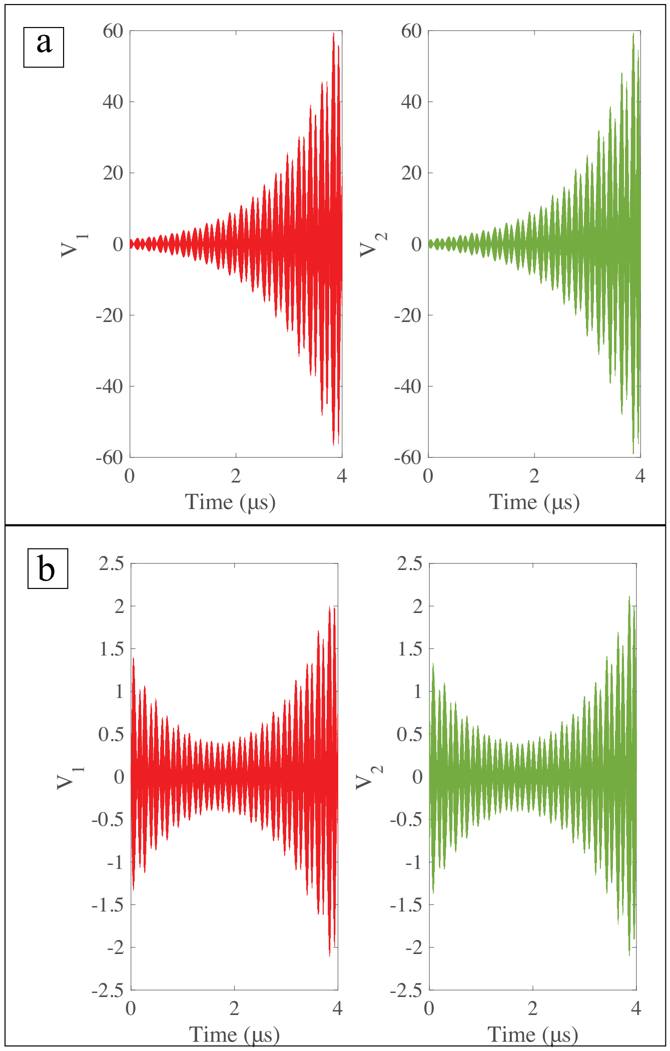

Figure 3.12: (Numerical data)The dynamics of the voltages V_1 (V_2) of the gain (loss) side where γ = 04897. (a) $I_{10} = 0$, $I_{20} = 0$, $V_{10} = 1$, $V_{20} = 0$. (b) $I_{10} = 0$, $I_{20} = 0$, $V_{10} = 0$, $V_{20} = 1$.

involves mixing down the signal to 30 MHz and the filtering (see section 2.4 for details). Figure 3.13 (b-f) show the numerical solutions, their heterodyned, and heterodyned filtered versions of $V_1(V_2)$ for a PT driven system.

Using the Downhill optimization method, the experimental gain and loss signals are fitted with the processed numerical solutions to optimize for the initial conditions

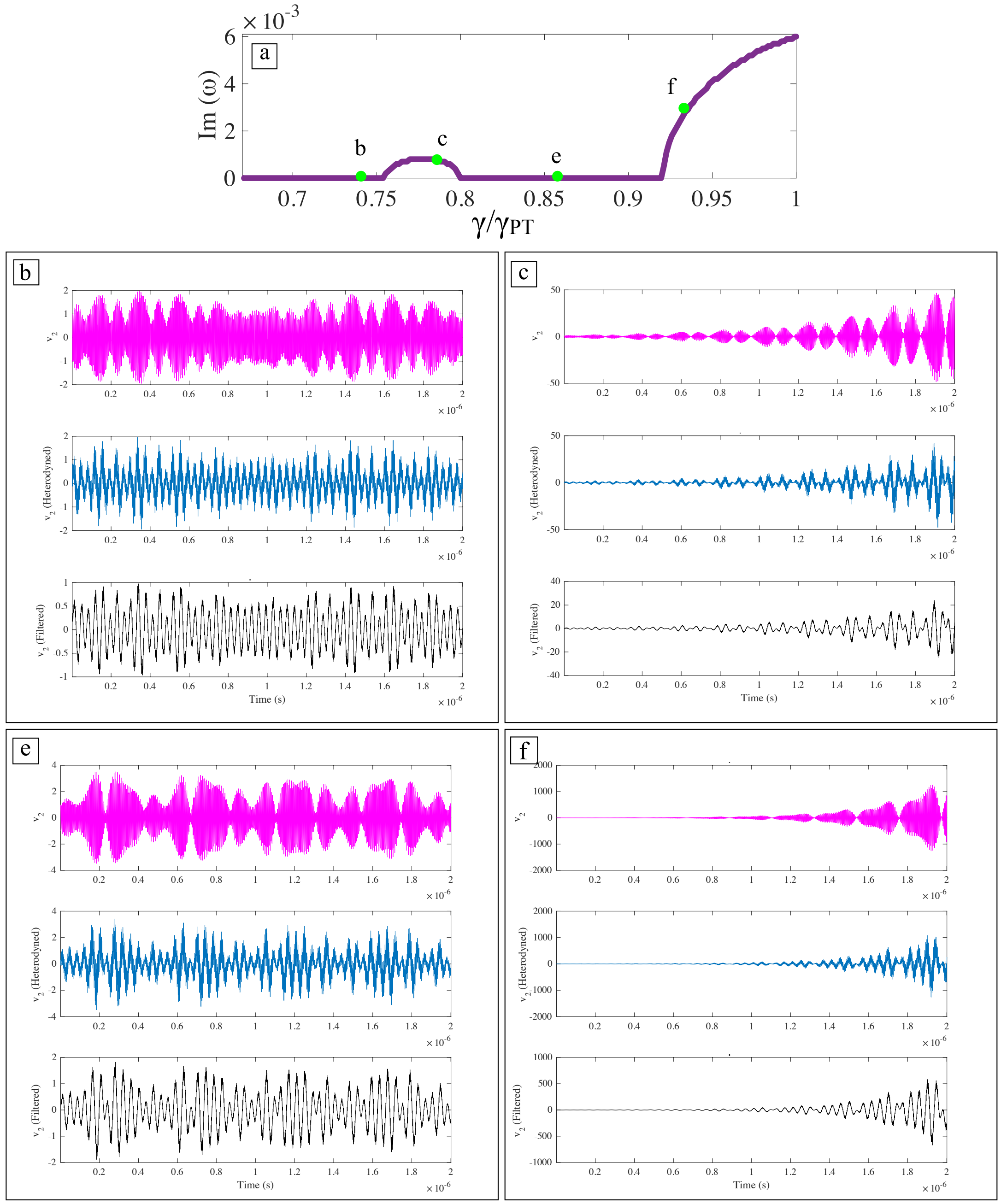

Figure 3.13:(Numerical data) First row in (b) , (c), (e), and (f) shows the numerical solution for the dynamics of the driven PT system obtained by solving Equations (1.1) and (1.2). The γ parameter for each solution and the position of that in the spectrum is shown in (a). Second, and third rows show the heterodyned and filtered heterodyned versions of each solution, respectively.

I_{10}, I_{20} , V_{10}, V_{20} and two additional factors corresponding to an arbitrary phase and

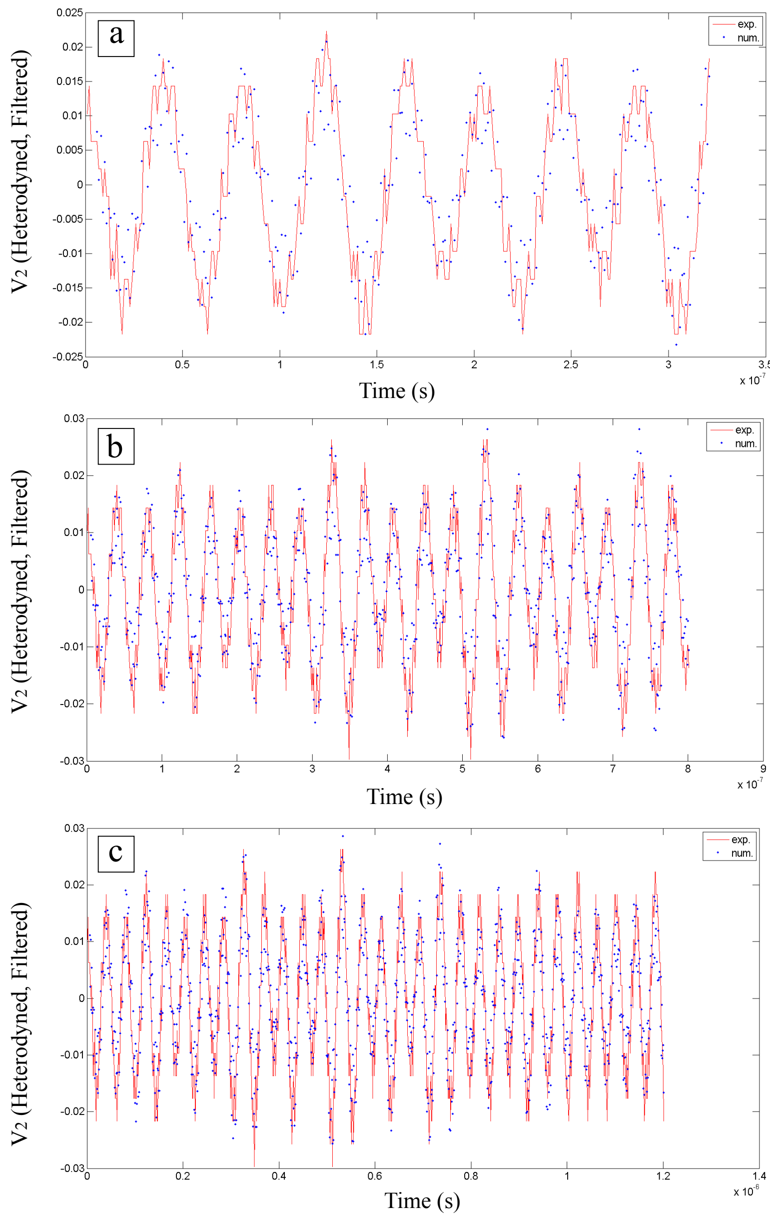

Figure 3.14: Experimental signals fitted with numerical solutions to obtain the initial conditions I_{10}, I_{20} , V_{10}, V_{20} for 8 periods of oscillation (a), 20 periods of oscillation (b), and 30 periods of oscillations (c) of mixed signal.

antenna balance adjustment due to the effect of amplifiers located in the gain and loss channels. This was done by defining a scaled sum of the squared errors between the experimental data and the corresponding numerical solution as a cost function. During the optimization process, each time the cost function is evaluated the numerical solution is recalculated and post-processed. Figure 3.14 (a-c) show the experimental data with the fitted numerical solutions for 8, 20, and 30 periods of oscillation of mixed signal. It is important to understand that each period of oscillation of mixed signal is about 10 periods of oscillation of original unmixed signal.

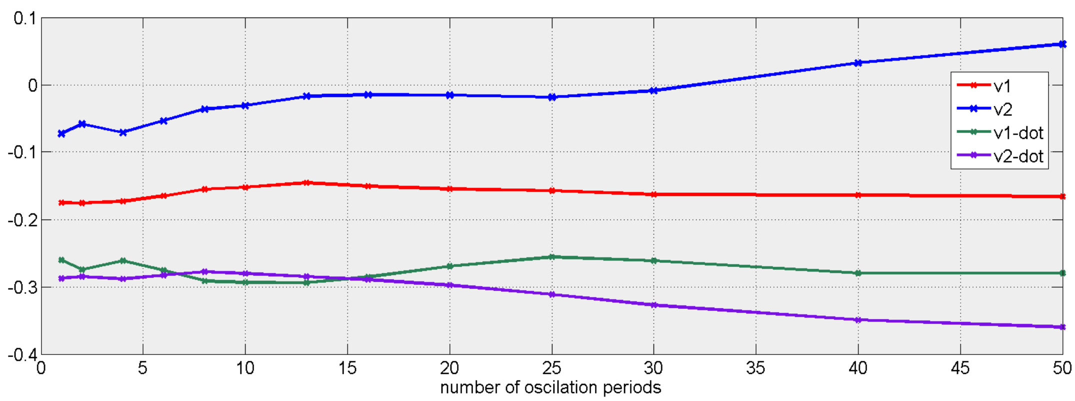

Figure 3.15: The results of initial conditions V_{10}, V_{20}, I_{10} , I_{20} optimized using numerical solutions for different periods of oscillation of mixed signal from 1 to 50.

The results of initial conditions V_{10}, V_{20}, I_{10} $(\dot{V}_{10})$, I_{20} $(\dot{V}_{20})$ optimized using numerical solutions for different periods of oscillation of mixed signal from 1 to 50 are reported in Figure 1.15. There is a lot of noise in the obtained initial conditions for smaller number of periods of oscillations. This is expected because there is not enough information to faithfully fit the experimental data. At the other end, close to 50 periods of oscillations, the results start to spread. This shows the differences between the data obtained from the real experimental system and a numerical solution. In the numerical simulation everything is perfect, whereas in the real system there are imbalances that make the signal grow or shrink after some time.

Chapter 4

Lasing Death Phenomenon

In this chapter, I present the experimental system of two coupled RLC circuits with active nonlinear conductances that determine gain parameters γ_1 and γ_2, and show that for specific pumping paths, the system experiences two threshold transitions from non-oscillatory (stable) to self-oscillatory (unstable) dynamics (associated with "lasing action" in the optics framework) despite the fact that the total gain $\gamma = \gamma_1 + \gamma_2$ continually increases along the path.

My main contribution to this work was building the initial condition circuit, performing the experimental measurements, and analyzing the data.

4.1 Stability Digram

Consider a coupled pair of oscillators with the same frequencies, each with their own gain or loss. Conductances of either sign placed in parallel with each LC resonator provide the gain parameters $\gamma_1 = \frac{1}{-R_1}\sqrt{\frac{L}{C}}$ and $\gamma_2 = \frac{1}{-R_2}\sqrt{\frac{L}{C}}$. In this chapter, positive γ refers to the gain and negative γ to the loss.

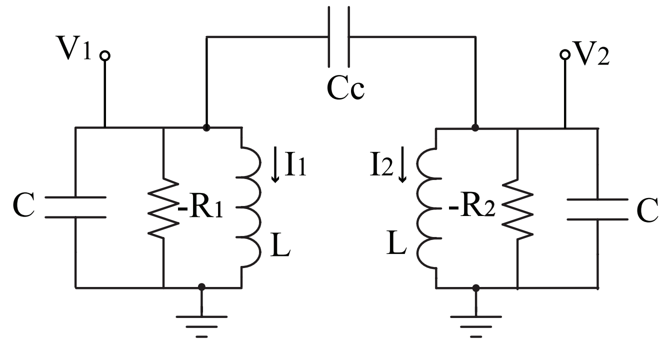

Figure 4.1: a coupled pair of oscillators with the same frequencies , each with their own gain or loss.

The active conductance of each LC unit is implemented with a parallel combination of a positive resistance with a variable negative resistance. This combination allows control of the total conductance over both positive and negative values, and thus exploration of the gain parameter space (γ_1 , γ_2) in all quadrants. We consider only capacitive coupling between the oscillator pair, and restrict the discussion to matched LC resonators.

Application of the first and second Kirchhoff's laws leads to the following set of equations for the LC node voltages V_n and inductor currents I_n, shown in the schematic Figure 4.1

$V_n = L\dot{I}_n$ $\qquad$ *n = 1, 2*

$$\frac{V_n}{R_n} + C\dot{V}_n + I_n + C_c(\dot{V}_n - \dot{V}_{3-n}) = 0 \tag{4.1}$$

We assume the frequency of ω' as the normal mode solution of the system, where all the time dependent quantities in Equation (4.1) oscillate as $e^{i\omega\varphi}$ if $\varphi = \omega_0 t$ and $\omega = \dfrac{\omega'}{\omega_0}$. Eliminating I_n, we get the following homogeneous equation:

$$\begin{bmatrix} \frac{1}{\omega} - \omega(1+c) - i\gamma_1 & \omega c \\ \omega c & \frac{1}{\omega} - \omega(1+c) - i\gamma_2 \end{bmatrix} \begin{bmatrix} V_1 \\ V_2 \end{bmatrix} = 0 \qquad (4.2)$$

where the parameters $\omega = \omega\sqrt{LC}$ and $c = Cc/C$ are a scaled frequency and coupling strength, and γ_1 and γ_2 are the gain parameters previously defined. The eigenfrequencies are found by setting the determinant of the coefficient matrix in Equation 4.2 equal to zero, and solving the characteristic polynomial.

The imaginary part of the eigenfrequencies ω of the system of Equations 4.2 dictate the stability of the system: the circuit is unstable if any of the modes have a positive imaginary part, otherwise it is stable. For a stable circuit all transient solutions are decaying, while for the unstable circuit, there is at least one exponentially growing solution corresponding to the electronic analog of “lasing” into the effective transmission lines.

The shaded domains in Figure 4.2 map the system stability in the γ parameter space. Unstable domains are indicated with red and are associated with an imaginary part of one of the eigenvalues being larger than zero. The stable domains are indicated with blue and they correspond to gain parameters γ_1, γ_2 for which $\mathrm{Im}(\omega) < 0$.

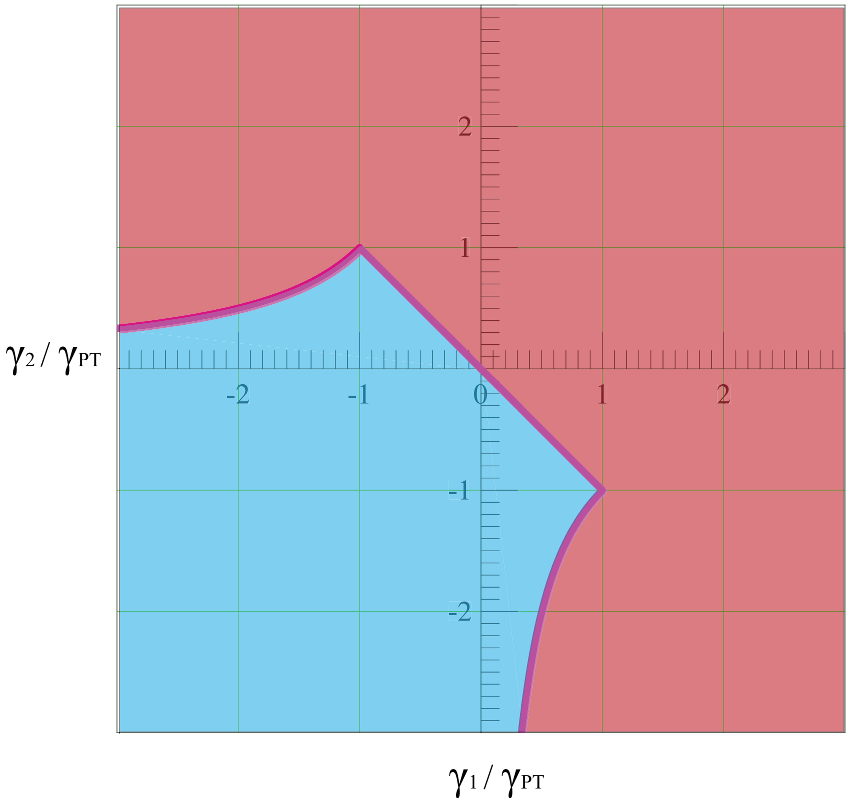

Figure 4.2: Stability diagram. Unstable domains are indicated with red and are associated with an imaginary part of one of the eigenvalues being larger than zero. Stable domains are indicated with blue and they correspond to gain parameters γ_1, γ_2 for which $\mathrm{Im}(\omega) < 0$.

It is therefore obvious that one can select pumping paths in the (γ_1, γ_2) plane which lead to transitions from stability to instability and back to stability while $\gamma_1 + \gamma_2$ is continuously increasing through the pumping process.

4.2 Experimental Set-Up

Figure 4.2 schematically illustrates the experimental circuit.

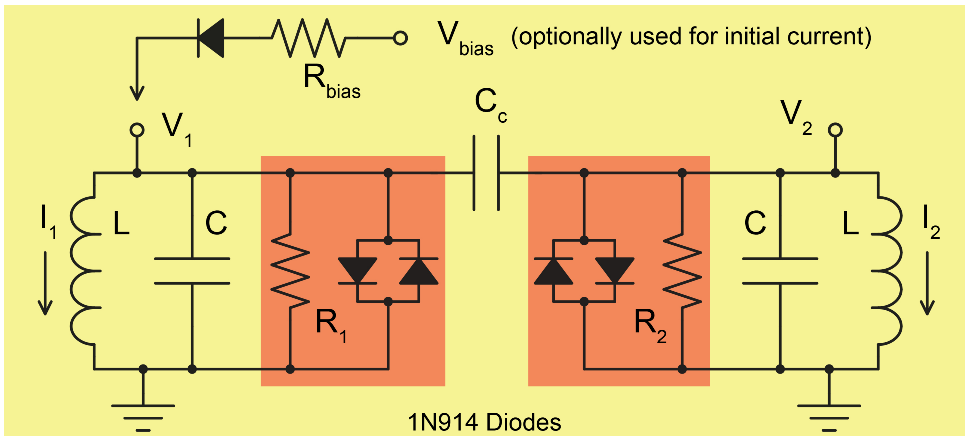

Figure 4.3: A pair of coupled LC resonators with parallel conductances (shaded) and coupling capacitance C_c. The conductance of each LC unit is equivalent to resistances R_1 and R_2 which can be of either sign, providing gain if negative, or loss if positive. The back-to-back diodes impose a lossy nonlinear contribution to conductance to assure a well-behaved limit cycle in the self oscillatory (unstable) regime. An initial current can be injected using the bias circuit at the top.

In order to make contact with saturable laser dynamics and ensure graceful behavior above threshold, a simple conductance nonlinearity is included by the addition of back-to-back 1N914 diodes, also in parallel with the LC resonators, as shown. This forces a dominant positive conductance (loss) at high voltage amplitudes, and assures a well behaved limit cycle when the system is unstable, above any oscillation threshold. The linear regime is below approximately 150 mV, where the diodes have negligible conductance.

Application of the first and second Kirchhoff's laws leads to the following set of equations for the LC node voltages V_n and inductor currents I_n, shown in the schematic Figure 4.3:

$$V_n = L\dot{I}_n$$
$$\frac{V_n}{R_n} + I_{sat}sinh(\frac{V_n}{V_t}) + C\dot{V}_n + I_n + C_c(\dot{V}_n - \dot{V}_{3-n}) = 0 \qquad (4.3)$$

4.2.1 Octoboard

Figure 4.4 shows our set-up and octoboard circuitry. The octoboard includes eight identical LRC oscillators each with fixed frequency (fixed L and C), and adjustable γ

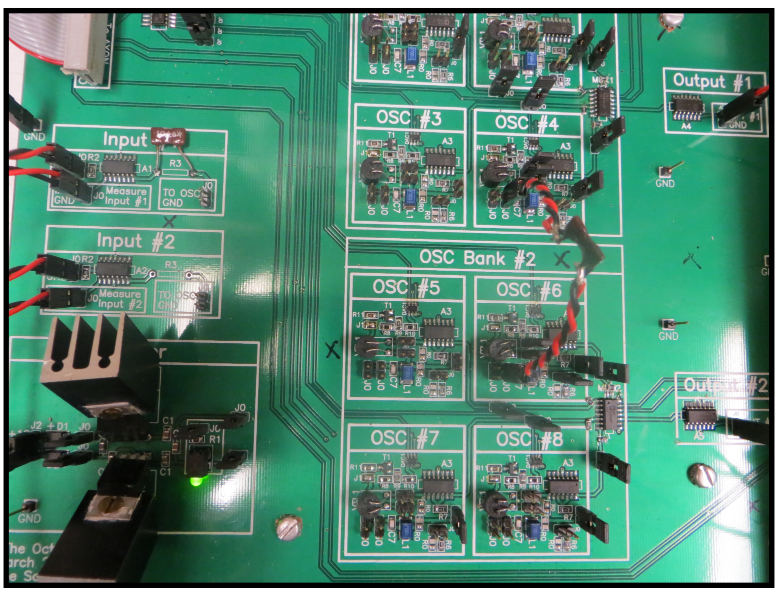

Figure 4.4: Experimental set-up and octoboard circuitry. The octoboard includes eight identical LRC oscillators each with fixed frequency (fixed L and C), and adjustable γ parameter for either gain or loss. Oscillator number 4 and 6 are coupled via a capacitor.

parameter for either gain or loss [10]. Oscillator number 4 and 6 are chosen as basis for Figure 4.3.

In this circuit, $L = 10\ \mu H$ and $C = 328$ pF as measured by the uncoupled frequencies $\omega / 2\pi = 2.78$ MHz after trimming the LC resonators to within 1% of each other. The coupling capacitance is $C_c = 56$ pF. The parameters $I_{sat} = 4.0$ nA and $V_t = 47$ mV are the reverse bias saturation current and the thermal voltage in the Shockley ideal diode used for the $sinh(\frac{V_n}{V_t})$ term in Equation 4.3. We note that the RLC pair can alternatively be considered as coupled to output leads connected to the LC nodes if the resistances R_1 and R_2 are re-interpreted as including the parallel characteristic impedance Z_0 of TEM transmission line leads. With Z_0 real and frequency independent, as is the case for TEM transmission lines, nonzero voltage V_1 or V_2 are then interpreted as coupling power into the corresponding transmission line (the analog of radiated optical power in a laser).

4.2.2 Initial Condition

Experimental frequencies are obtained by imposing an initial DC current (I_0) in side $n = 1$ through a forward biased 1N914 signal diode (Figure 4.4). I_0 is determined by R_0 ($R_0 = \frac{11.4V}{I_0}$). This pulsing circuit provides excellent initial conditions by (1) killing any oscillation caused by the gain, (2) setting $I_1(0) = I_0$, $I_1 = 0$, $V_1 = 0$, $V_2 = 0$, and, (3) synchronizing the initial conditions with the oscilloscope capture to measure complex ω by fitting the transient part of the output signal.

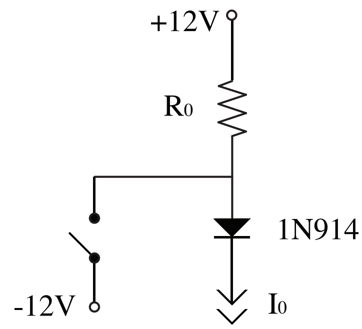

Figure 4.5: Schematic digram of the low capacitance DC current injector.

The bias voltage of the optional injection circuit of Figure 4.4 is then rapidly switched to a reverse-biased state, where the contribution to the circuit is the small ≈ 0.3 pF junction capacitance of the reverse biased diode.

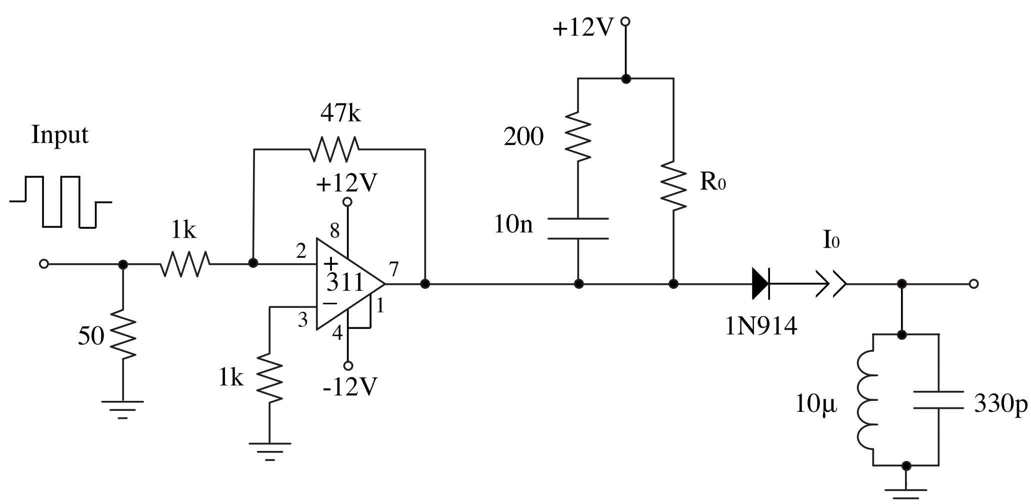

Figure 4.6: Schematic digram of switch, 'on' state damper, and 'off' state DC current injector.

The Schematic digram of the switch is shown in Figure 4.5 separately. Using a square wave input, the LM311 open collector switches very rapidly between -12 Volts and an open circuit. The input square wave amplitude is less than 1 Volts. When the

LM311 output voltage is -12, the switch of Figure 4.5 is 'on' .The series capacitor and resistor, in parallel with R_0 ($R_0 = \frac{11.4V}{I_0}$), acts as a damper (when the switch is on and diode is reversed biased) to kill any oscillation in the RLC circuit caused by the gain. When switch is off diode is forward biased and initial current injects to the LC rapidly setting into the initial current of the inductor.

4.3 Dynamics and Stability Analysis

The lasing death behavior for our electronic circuit can be experimentally confirmed via steady-state measurements of the RMS voltage V_{rms} of either node as we increase the overall gain of the system. Our system is considered stable when $V_{rms} = 0$. In contrast when the system is unstable, a nonzero value of V_{rms} is measured that is dictated by the circuit saturation dynamics, in this case the back-to-back signal diodes. Mathematically, the saturation dynamics is determined by the nonlinear $sinh(\frac{V_n}{V_t})$ term in the Equation (4.3).

We want to understand which pumping paths can result in lasing death. These paths are associated with the existence of reentrant stability domains in the (γ_1, γ_2) plane which are traversed by the specific pumping schemes (Figure 4.2). In this respect, every time that a path crosses a boundary between an unstable to stable domain we have a suppression of lasing action and thus the emergence of lasing death.

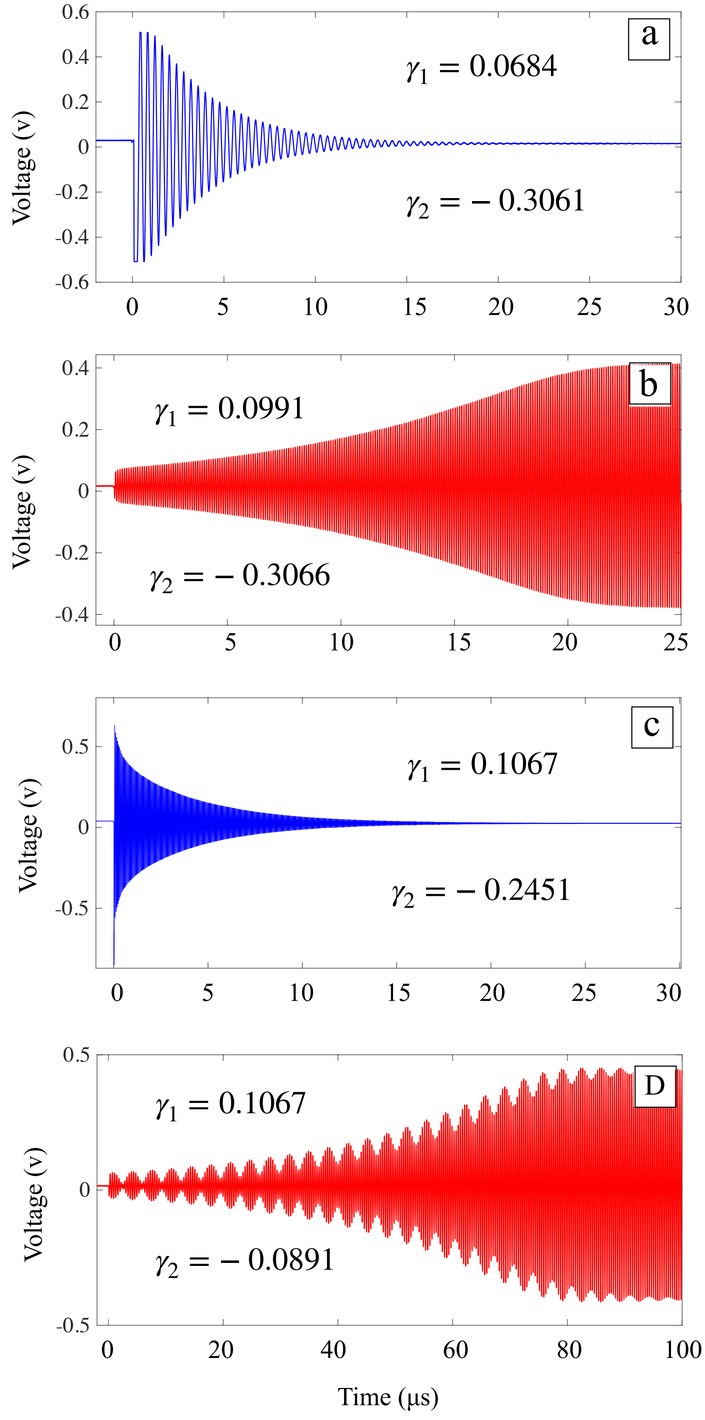

Figure 4.7: The subsequent voltage evolution recorded on node $n = 1$. The total gain $\gamma = \gamma_1 + \gamma_2$ increases from (a) to (d), while system experiences stable(a) unstable (b) stable (c) and Unstable (d) dynamics. Corresponding points can be followed in the inset of Figure 4.8. Initial conditions (corresponding R_0) in (a) and (c) are different from those in (b) and (d).

The subsequent voltage evolution on node $n = 1$ is recorded and fit to a generic double resonance transient to obtain the complex eigenfrequencies, from which the mode with the most positive imaginary part is identified. The imaginary part of the eigenfrequencies ω of the system dictate the stability of the system: the circuit is unstable if any of the modes have a positive imaginary part, otherwise it is stable. Figure 4.7 shows the voltage evolution on node $n = 1$ recorded for four different sets of γ values. While the total gain is increasing from Figure 4.7a to Figure 4.7d, system experiences several stable and unstable dynamics. The inset in Figure 4.8 shows the position of each set of γ on the stability diagram.

4.4 Results

The data in Figure 4.8 correspond to several paths of increasing γ_2, along the vertical lines shown in the inset, with γ_1 = const. In all cases the total gain $\gamma_1 + \gamma_2$ provided to the system is increased. We find that depending on the value of γ_1 the system either undergoes a transition from instability to stability or it remains unstable all the time. The former case corresponds to the phenomenon of lasing death and is achieved only for the leftmost three pumping paths shown in the inset of Figure 4.8.

The shaded domains in the inset of Figure 4.8 map the system stability in the gain parameter space with the unstable domain extending into the regions of large positive γ_n . The pumping path associated with the top data set corresponds to large enough γ_1 to completely miss the stable region as γ_2 is increased. Subsequent paths along increasing γ_2 with smaller values of γ_1 pass progressively deeper through the reentrant stability region, resulting in complete extinction of the oscillation followed

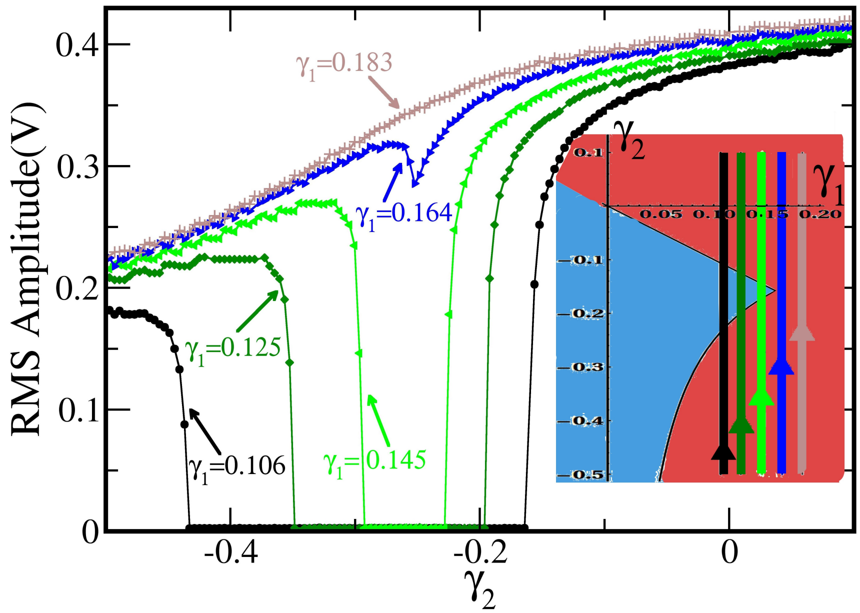

Figure 4.8: Experimental steady-state voltage for paths of increasing γ_2 at fixed γ_1 shown in the inset. The voltage was measured on the side-1 LC node. Note that the width of the "lasing death" response diminishes as the overall gain increases.

by a new threshold. The data sets illustrate how the linear stability map is directly related to the observed reentrant stability response of the nonlinear system.

Figure 4.9 shows the evolution of experimental values for $Im(\omega)$ as a function of total gain, defined as $\gamma_1 + \gamma_2$ obtained along the path in the (γ_1, γ_2) stability map shown in the inset. The color scheme used is the same as that of Figure 4.8.

Let us now compare the experimental stability diagram of Figure 4.9 with the experimental measured temporal dynamics of the RLC circuit shown in Figure 4.8. Starting along the horizontal path of Figure 4.9 (inset), the "lasing action" of our electronic system turns on at a first threshold of stability as γ_1 is increased for fixed γ_2 (correlate this path with the data shown with a black line in Figure 4.8) rising up through $Im(\omega) = 0$. Continuing along the vertical path in the inset, as γ_2 is increased

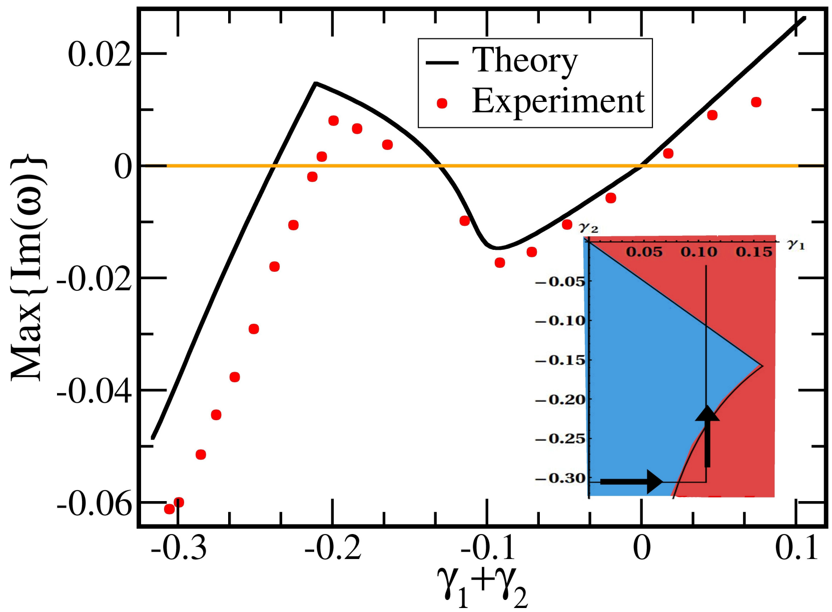

Figure 4.9: The theoretical and experimental maximum imaginary part of all eigenfrequencies is shown as total gain (horizontal axis) is increased. The pumping path is illustrated by the stability diagram (inset). The "lasing death" phenomenon occurs when the path traverses a protrusion in the stability map—the most positive imaginary part momentarily dips back into the negative region. The vertical path in the inset corresponds to the black curve of Figure 4.7 where the steady-state saturation amplitude was presented.

with γ_1 fixed, the lasing death (amplification death) is realized as the path cuts through the protruding section of the stability map. Along this path, the imaginary part of the eigenfrequency drops back into the stable regime with $Im(\omega) < 0$, then turns around and finally becomes permanently positive (unstable). Note that the complete path follows one of monotonically increasing total gain and experiences both turn-on thresholds.

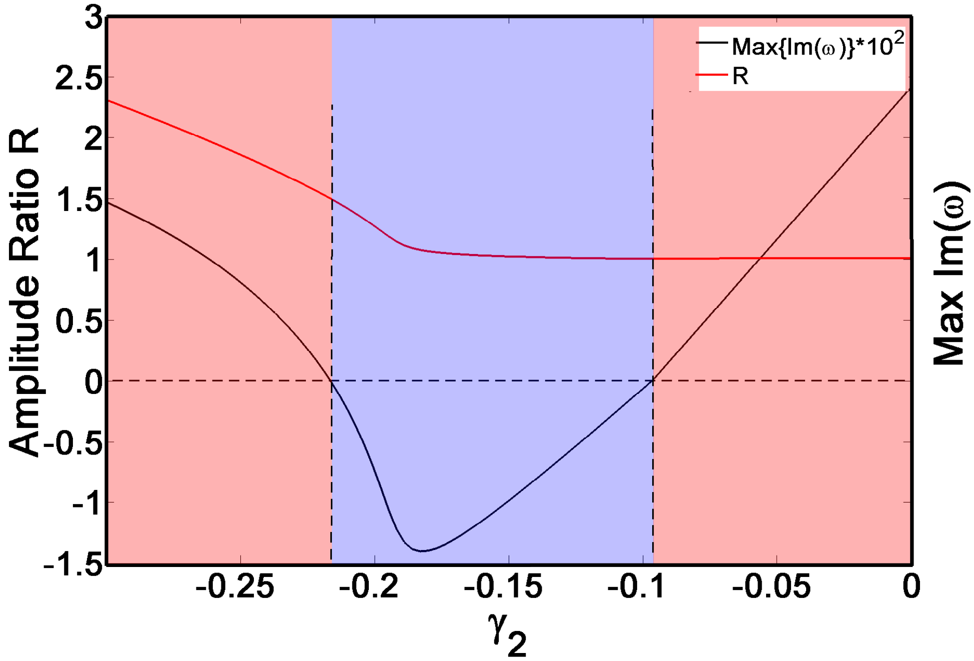

Figure 4.10: The parametric evolution of the ratio R between the two components of the most unstable linear mode (red line). For comparison we also report the Max Im(ω). Three domains are identified: The most left and the right domains are associated to R > 1 and R = 1 and correspond to unstable dynamics. The middle domain is associated with the LD phenomenon and it indicates stable dynamics.

The details of the lasing death are then revealed through Figure 4.10 where we show $\omega^{(1)}$ as well as the ratio $R = |\, V_1^{(1)}/V_2^{(1)} \,|$ along the reentrant portion of Figure 4.8, as a function of γ_2 with $\gamma_1 = 0.0967$ fixed. Starting from the left with large negative values of γ_2, we find the system in the unstable regime. How is this possible with negative total gain $\gamma_1 + \gamma_2$? The value of R indicates that the normal mode is dominated by oscillations of the mode with the positive gain. Why then does the lasing death happen in spite of the total gain being increased? As γ_2 increases, the mode shifts toward a balanced configuration with R ~ 1, exposing the system to a total accepted input power more closely reflecting the still negative total gain $\gamma_1 + \gamma_2$. Finally, as γ_2 continues to increase, with R ~ 1 confirming that the balanced mode configuration persists, the total input power once again overcomes the losses (including the output coupling) and the system crosses back above threshold.

From the above discussion we conclude that the stability of our system and the lasing death phenomenon are directly linked with the stability diagram and the parametric evolution of the complex eigenvalues ω. Specifically the sign of their imaginary part $Im(\omega)$ defines the stability $[Im(\omega) < 0]$ or instability $[Im(\omega) > 0]$ of the associated modes and therefore of the system itself.

4.5 Conclusion

To summarize, we have identified a generic link between spatially distributed gain and the phenomenon of lasing death. By using a system of two coupled RLC circuits with active nonlinear conductances that determine gain parameters γ_1 and γ_2 , we have shown that for specific pumping paths, the system experiences two threshold transitions from non-oscillatory (stable) to self-oscillatory (unstable) dynamics (associated with “lasing action” in the optics framework) despite the fact that the total gain $\gamma = \gamma_1 + \gamma_2$ continually increases along the path.

Chapter 5

Encircling the Exceptional Point

Exceptional points (EP) are associated with symmetry breaking for PT-symmetric Hamiltonians. The interesting nature of exceptional points in addition to their dramatic effects on instabilities, scattering problems, and phase transitions has been studied theoretically and experimentally in different areas of physics [43-47].

It has been predicted and demonstrated that topological operations in the vicinity of these points can lead to certain results without requiring to change the system local details [48-50]. Therefore, existence of EPs in the spectrum of any physical device can open up new directions in system control. For instance, it was predicted and then tested for optomechanical systems [51] and microwave cavities [52] that encircling the EPs can transfer the energy between different modes. It has been also demonstrated that this energy transfer is nonreciprocal and is independent of initial state. This work has not been done in electronics framework.

In my most recent project, I designed and implemented an ultra high frequency electronic system in the presence of exceptional point. The Exceptional point will be encircled in the parameter space in two different directions with different initial states.

5.1 Experimental set up

Here, I provide an experimental platform where the exceptional point (EP) is encircled in C and C_c parameter space. The experimental setup is explained in two subsections. First, the UHF system with the ability to provide a suitable parameter space will be explained. Second, the apparatus which makes the encircling path possible will be described.

5.1.1 UHF system

The experimental set-up of our coupled oscillators is similar to the UHF experimental set-up shown in Figure 1.2 of Chapter 1.. It consists of two coupled ~ 235 MHz LC resonators. However, the natural frequency of resonators and the amount of gain and loss are not necessarily balanced in this experiment. The capacitance that couples the two resonators is driven with a network of varactor diodes.

The fixed natural frequency $\omega_0/2\pi$ = 235 MHz was chosen as the frequency of the LC oscillator in the loss side. Frequency of the LC oscillator in the gain side is not fixed and changes by using the BB135 variable capacitor network shown in Figures 1.2 and 1.23. Gain and loss (corresponding to effective parallel resistances $\mp$ R) are

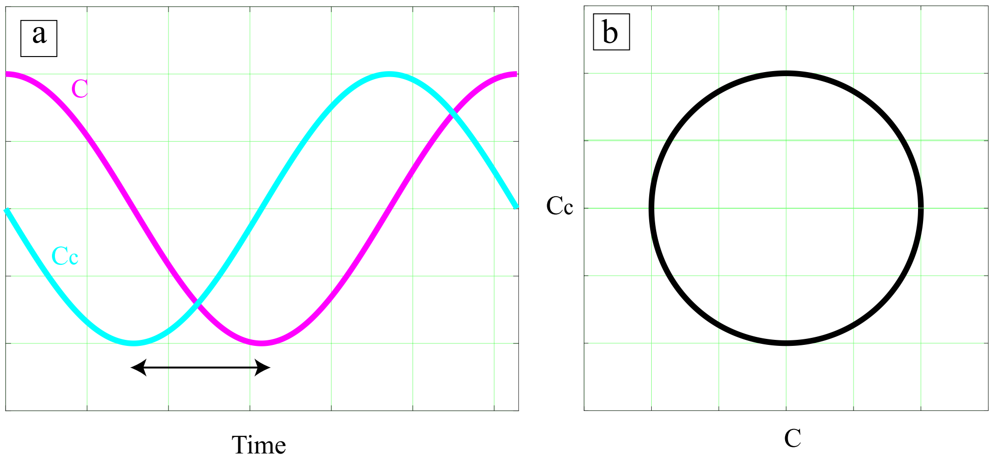

Figure 5.1 : (a) Parametric plot of coupling capacitance and gain side capacitance within a period of cycling. (b) C_c and C parameter space. C_c and C shown in (a) are plotted versus each other.

implemented via the optical isolators (please see Chapter 1 for more details). Using different DC voltages, the coupling network shown in Figure 1.18a provides the variable coupling between the oscillators.

As mentioned, in this experiment C_c and C corresponding to the coupling capacitor and LC capacitor in the gain side are variables and can provide the parameter space.

5.1.2 Encircling

To encircle the EP in C_c and C parameter space, a differentiator electronic circuit is required. C_c and C oscillate independently during one period of cycling but with 90 degrees phase difference. Figure 5.1a shows the parametric plot of coupling capacitance and gain-side capacitance within one period of cycling. These

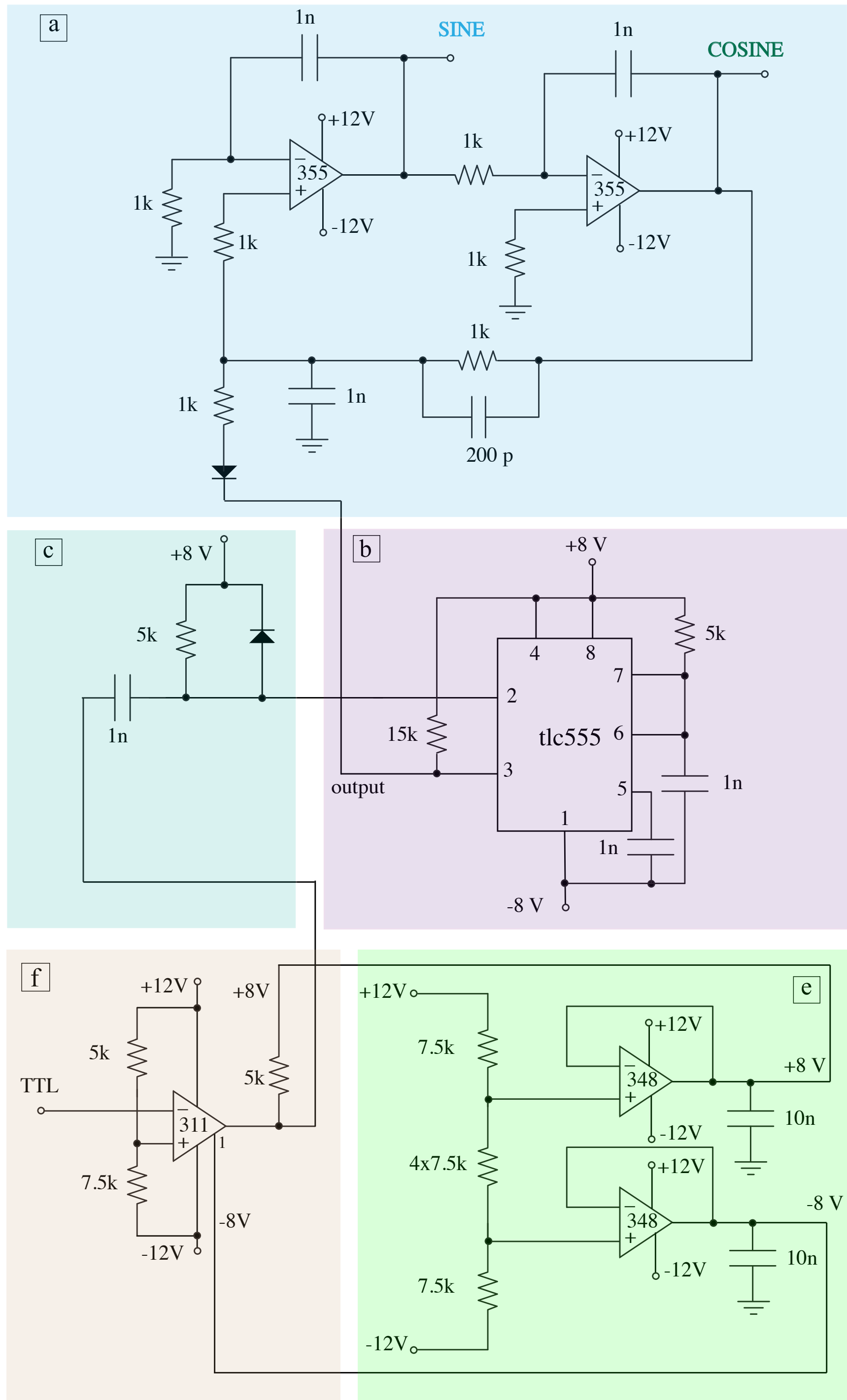

Figure 5.2: Schematic diagram of (a) the differentiator which provides the cycling in parameter space, (b) the timer monostable operation which provides the square wave pulse, (c) integrator which creates a short trigger for the timer, (f) the 311 op-ams which reverses the TTL, and (e) - and +8 source voltages.

capacitances vary sinusoidally with 90 degrees phase difference. Figure 5.1b shows a state space plot of C_c and C shown in Figure 5.1a.

Figure 5.2a shows the schematic diagram of the differentiator circuit. In this scheme, two 355 op-amps provide two sinusoidal outputs with 90 degrees phase difference. The cycling period is controlled by 1 nF capacitors, and its radius by the input 1k resistor. The pair of 1 kOhm resistor and 200 pF capacitor controls the instability (growth or decay) of the outputs. Sine and Cosine output voltages run the coupling and the gain-side tuning capacitors, respectively. The capacitance of BB13 varactor diode as a function of the biased voltage across the diode is shown in Figure 1.17. Although their relation is not linear for the whole range shown in Figure 1.17, a linear relation can be a good approximation for the desired small radius of cycling ($<$ 0.05 pF). Therefore, for small voltages, this scheme also makes a cycler in C_c and C parameter space.

To make the cycling happen just like a pulse (shot), a tlc555 timer in the monostable operation scheme is used. Figure 5.2b shows the schematic digram of the circuit which provides an square wave shot to run the input of the cycler. The tlc555 timer is usually used to get a long pulse from a short trigger. In this case since the timer input is a long square wave and a short pulse is the desired output, an integrator circuit (Figure 5.2c) is located before the timer to make a short trigger.

The function generator's TTL port is used for triggering. However, because of the diode in the cycler set-up (Figure 5.2a), the TTL square wave is reversed by using a 311 op-amps (Figure 5.2f) and then sent through the integrator, monostable timer and finally the cycler. Figure 5.2e shows the scheme which provides - and +8 source voltages for all the steps.

5.2 The Cycling Period

There are restrictions both experimentally and theoretically in determining the period and radius of cycling in the parameter space.

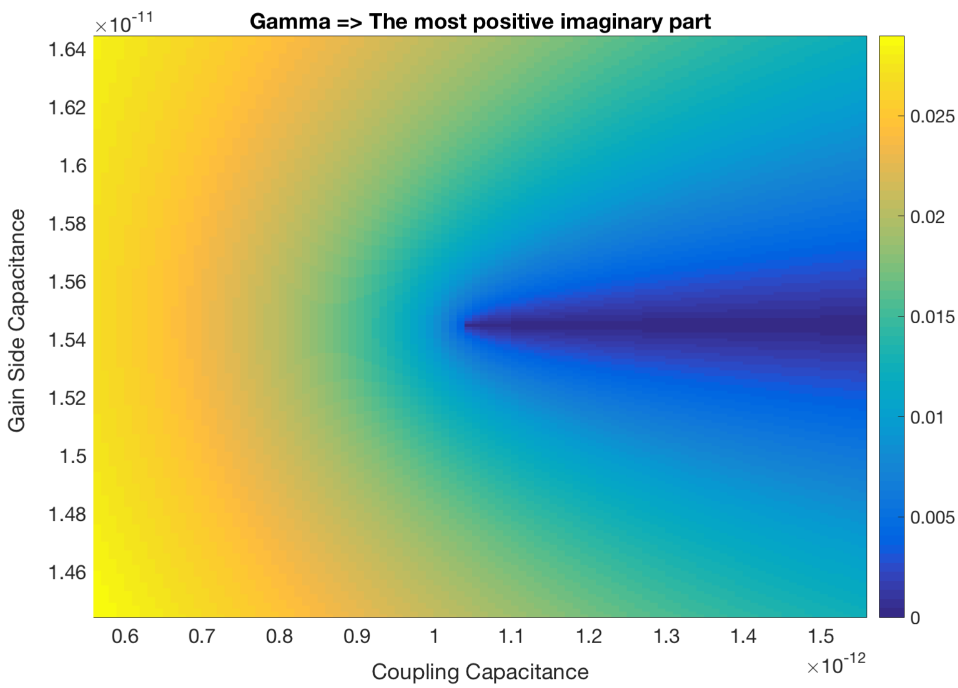

Figure 5.3: (numerical data) Vertical and horizontal axis together represent the parameter space and ranges that are experimentally accessible. Pseudo color indicates the imaginary part of eigenfrequency with the most positive imaginary part.

For better comparison with theory, the speed of cycling should be slow, much slower than the oscillation rate of resonators. However, experimentally the output signals saturate, see Chapter 2 for reasons behind signal saturation. Therefore, cycling period can not be very long. The output signals saturate eventually and all the cycling processes needs to be done before saturation.

The color map shown in Figure 5.3 indicates the numerical results of the parameter space. Vertical axis indicates the gain-side capacitance (corresponding to the gain side natural frequency) and horizontal axis represents the coupling capacitance. Pseudo color is the imaginary part of eigenfrequencies with the most positive imaginary part. Exceptional point happens where C = 15.54 pF and C_c = 1.03 pF.Data shown in

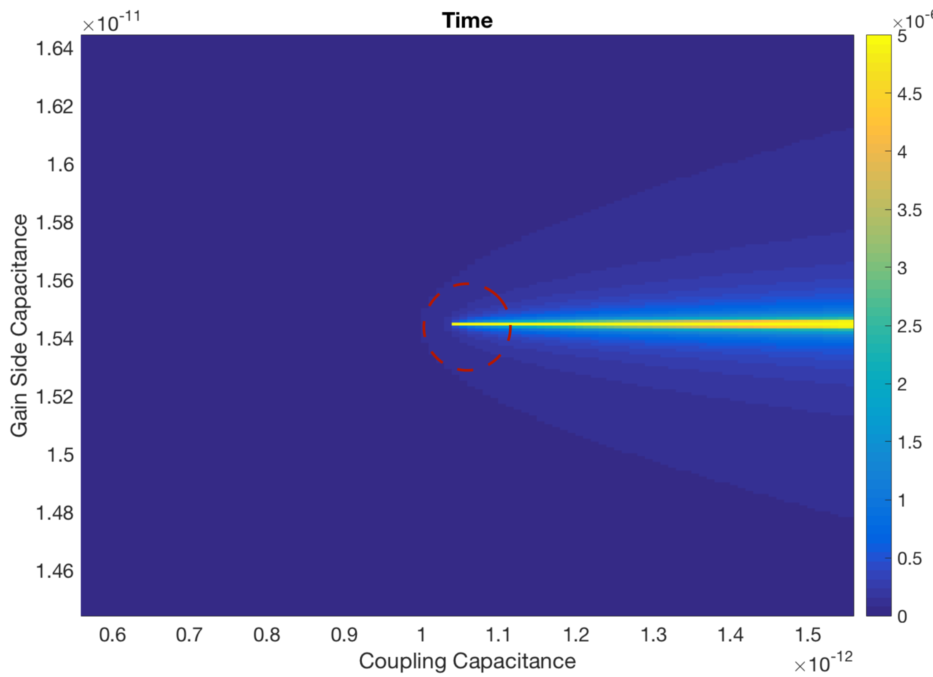

Figure 5.4 (numerical data) The color map indicates the approximate time we have experimentally before saturation occurs for the output signal.

Figure 5.3 is used to calculate the approximate time before saturation occurs for the output signal at each set of C and Cc.. The color map in Figure 5.4 indicates the transient time before the saturation.

Numerical data in Figure 5.4 shows that not all radiuses can be chosen to encircle the exceptional point ($C = 15.54$ pF and $C_c = 1.03$ pF). However, for a range of radiuses (< 0.05 pF) cycling can be done (shown with a red circle in Figure 5.4) and its period should be a few microseconds .

5.3 Measurement

The measurement process of this experiment consists of two main steps. The first step is finding the exceptional point in the parameter space, and the second one is sitting in a suitable distance from the point (cycling radius) and encircling that in a suitable time period.

5.3.1 Finding the EP

During the development process, I designed the system for the exceptional point to occur somewhere in the range of C and C_c which is experimentally achievable. Due to the minimum and maximum values of the BB135 variable capacitance in the coupling and gain side tuning networks, there are limitations on moving in C and C_c parameter space (please see Figures 1.19 and 1.24). In Chapter 1 section 1.1.4, several reasons were mentioned why the calibration of this system is subject to the day long drifting. Considering this issue, I set the capacitance ranges (C and C_c) such that the exceptional point happens at the middle of the parameters ranges shown in Figure 5.4. Therefore, the time drifting does not cause the EP position to fall out of the range. For the same reason, every time before encircling the EP, its exact position needs to be found.

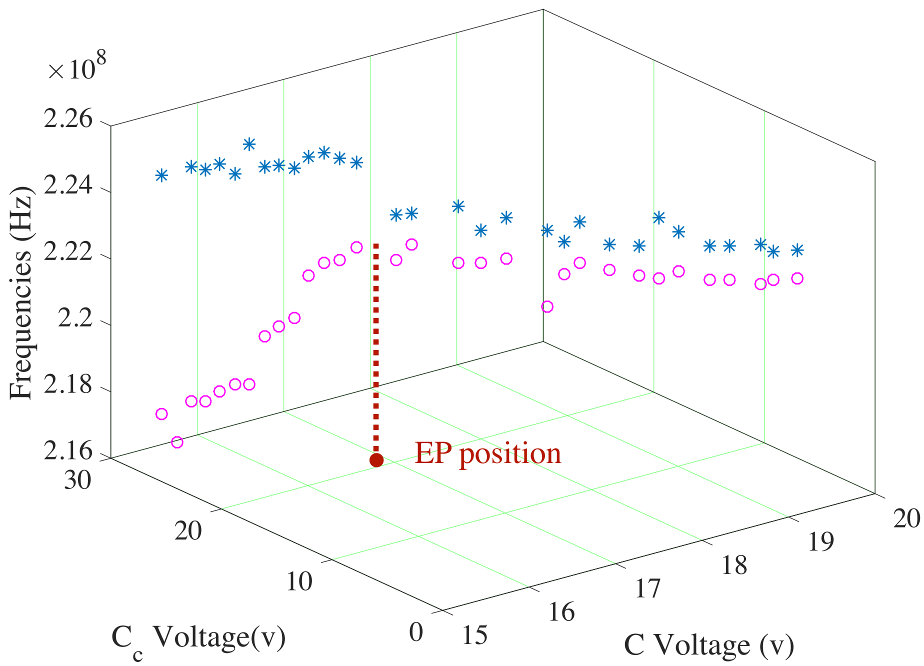

Figure 5.5: (Experimental data) x and y axes represent the voltage across the gain side and coupling variable capacitances, respectively. z axis (vertical) is the eigenfrequencies of the system. Exceptional point happens where the eigenfrequencies of the system merge together.

EPs are associated with symmetry breaking, where two eigenfrequencies of the system merge together and broken phase regime starts. By using the same method explained in Chapter 2 section 2.2, the EP position is found, except in this experiment loss side γ value is fixed ($\gamma_{loss} = 0.0675$) and instead the coupling capacitance changes in each step. The 3D plot in Figure 5.5 shows the eigenfrequencies of the system (z axis) in C and C_c parameter space. The x and y axes respectively represent the voltage across the gain side and coupling capacitance networks, and although they do not directly represent C and C_c corresponding to the parameter space (please see Figures 1.19 and 1.24). EP happens where the eigenfrequencies merge.

Figure 5.6 shows the gain voltage (z axis) needed for the output signal to get to the threshold value (25 mV) in the parameter space (x and y axes are the same as Figure 5.5). At the EP and after that, since the system experiences instabilities, gain value needed by the system to get to the threshold value starts to decrease. Comparing Figures 5.5 and 5.6 we see that this phenomenon and the merging of eigenfrequencies happen at the same point.

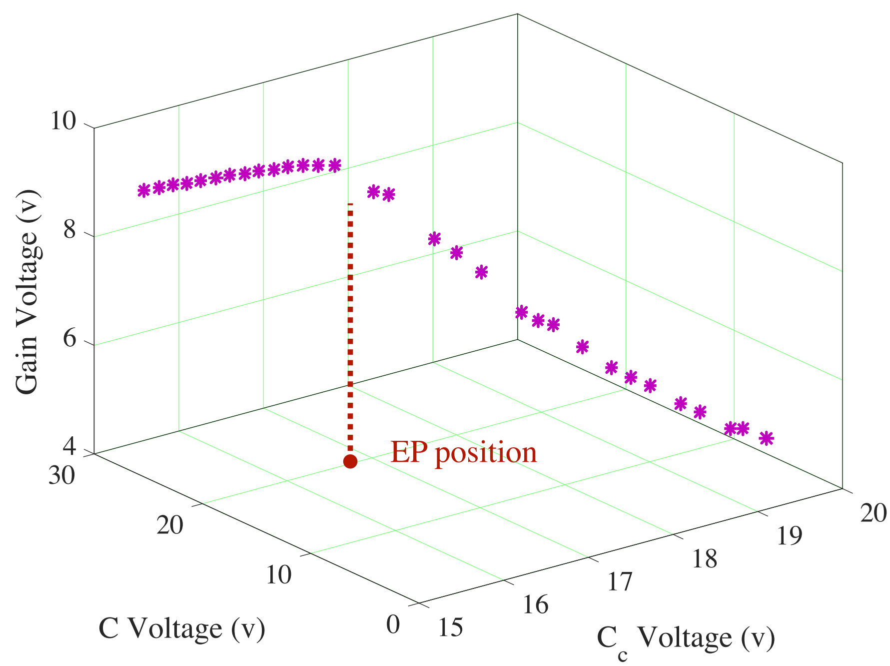

Figure 5.6: (Experimental data) Horizontal axes x and y respectively represent the voltage across the gain side and coupling variable capacitances. z axis is the gain needed by the system output to get to the threshold value. Exceptional point happens where gain needed by the system starts to decrease.

Points in parameter space corresponding to these phenomena are marked as the exceptional point. Figure 5.7 shows the parameter space and the place of EP corresponding to these changes. It is located at the center of the circles.

5.3.2 Future and Final part

After finding and marking the EP, the initial point (initial state) will be determined. Based on the desired cycling radius, program determines the suitable distance from EP in the exact phase regime and sets the parameter for that point. Cycler then will be

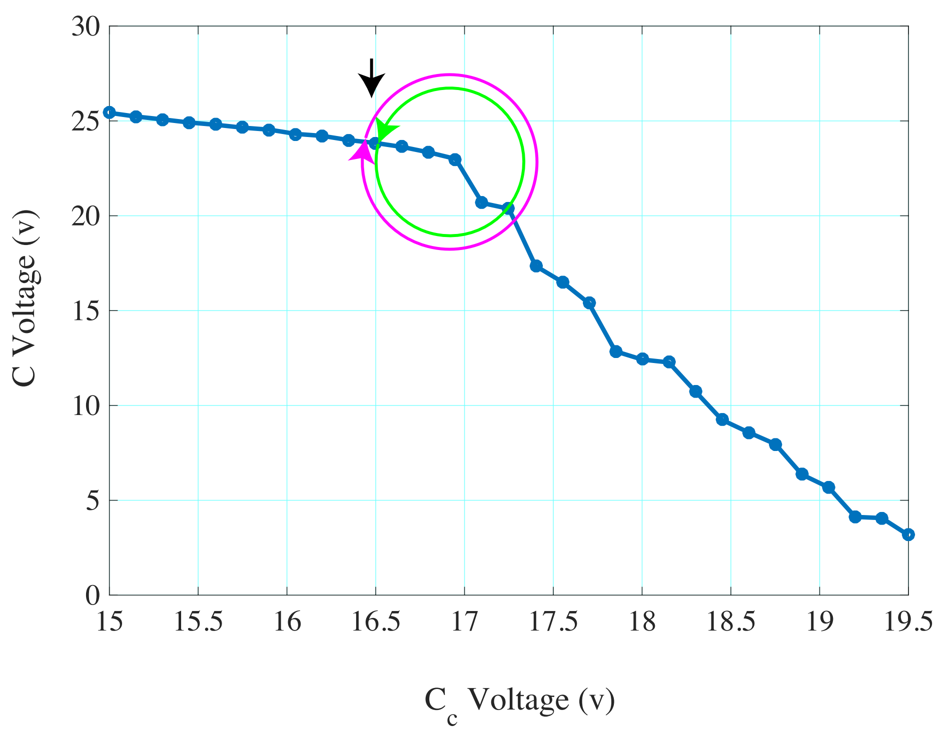

Figure 5.7: (Experimental data) Voltages across the capacitances which make the parameter space. EP is located at the center of the circles. Black arrow shows the position of initial state in the exact phase regime. The EP will be encircled in two different directions.

turned on, and the evolution of the output signal will be captured by computer. Encircling will be done in two different directions (Figure 5.7).

Summary

The major goal of my PhD research was the design and apparatus development of the ultra high frequency driven PT symmetric dimer, which was covered in a major portion of this dissertation. Chapters 1, 2, 3, and part of Chapter 5 described this subject in detail. In Chapter 1, the experimental set-up was introduced and a theoretical foundation was presented. Chapter 2 summarized the methods and experimental techniques used to acquire the data. Chapter 3 then completed this subject by presenting the experimental results obtained for a periodically driven PT symmetric system. We found that the UHF driven PT symmetric dimer supports a sequence of spontaneous PT-symmetry broken domains bounded by exceptional points in its spectrum. The position and size of these instability islands can be controlled through the amplitude and frequency of the driving. The results of this project, a UHF driven PT symmetric dimer working at frequency of 235 MHz, is published in [8].

Chapter 4 was allocated to the project of “Lasing Death” phenomenon in electronics framework. By presenting the experimental system of two 3 MHz coupled RLC circuits with active nonlinear conductances, it was demonstrated that amplification action can be tamed via asymmetric pumping. Under specific conditions

we observe the counterintuitive phenomenon of stabilization of the system even when the overall gain provided is increased. The key results of Chapter 4 are published in [7].

Finally, in Chapter 5 I talked about my ongoing project on “Encircling the Exceptional point”. The transition point γ_{PT} in the spectrum of a PT symmetric dimer shows all features of an exceptional point (EP) singularity where both eigenfunctions and eigenvalues merge. It is predicted that encircling the EPs can transfer the energy between different modes where this energy transfer is nonreciprocal and is independent of the initial state. This project was performed on the same experimental set-up as in Chapter 1. The latest results are reported in Chapter 5 as this is a work-in-progress project.

Bibliography

1. Joseph Schindler, Ang Li, Mei C Zheng, FM Ellis, and Tsampikos Kottos. Physical Review A, 84(4):040101 (2011).

2. Zin Lin, Joseph Schindler, Fred M Ellis, and Tsampikos Kottos. Physical Review A, 85(5):050101(2012).

3. Hamidreza Ramezani, J Schindler, FM Ellis, Uwe Gunther, and Tsampikos Kottos. Physical Review A, 85(6):062122 (2012).

4. J Schindler, Z Lin, JM Lee, H Ramezani, FM Ellis, and T Kottos. Journal of Physics A: Mathematical and Theoretical, 45(44):444029 (2012).

5. Nicholas Bender, Samuel Factor, Joshua D Bodyfelt, Hamidreza Ramezani, Demetrios N Christodoulides, Fred M Ellis, Tsampikos Kottos. Physical review letters 110 (23), 234101 (2013).

6. JM Lee, S Factor, Z Lin, I Vitebskiy, FM Ellis, T Kottos. Physical review letters 112 (25), 253902 (2014).

7. M Chitsazi, S Factor, J Schindler, H Ramezani, FM Ellis, T Kottos. Physical Review A 89 (4), 043842 (2014).

8. M Chitsazi, H Li, FM Ellis, T Kottos. Physical review letters 119 (9), 093901 (2017).

9. Carl M. Bender and Stefan Boettcher. Physical review letters, 80:5243, 6 (1998).

10. Joseph Caulfield Schindler, MSc degree, (2013).

11. C. M. Bender, S. Boettcher, and P. N. Meisinger, J. Math. Phys. 40, 2201 (1999).

12. C. M. Bender, D. C. Brody, and H. F. Jones, Phys. Rev. Lett. 89, 270401 (2002).

13. K. G. Makris, R. El-Ganainy, D. N. Christodoulides, and Z. H. Musslimani, Phys. Rev. Lett. 100, 103904 (2008).

14. A. Guo et al., Phys. Rev. Lett. 103, 093902 (2009).

15. C. E. Ruter et al., Nat. Phys. 6, 192 (2010).

16. H. Ramezani, T. Kottos, R. El-Ganainy, and D. N. Christodoulides, Phys. Rev. A 82, 043803 (2010).

17. M. C. Zheng, D. N. Christodoulides, R. Fleischmann, and T. Kottos, Phys. Rev. A 82, 010103 (2010).

18. S. Longhi, Phys. Rev. Lett. 103, 123601 (2009).

19. A. A. Sukhorukov, Z. Xu, and Y. S. Kivshar, Phys. Rev. A 82, 043818 (2010).

20. S. Longhi, Phys. Rev. A 82, 031801 (2010).

21. Z. Lin et al., Phys. Rev. Lett. 106, 213901 (2011).

22. E. M. Graefe, H. J. Korsch, and A. E. Niederle, Phys. Rev. Lett. 101, 150408 (2008).

23. D. Psiachos, N. Lazarides, and G. P. Tsironis, Appl. Physical Review A, 117, 663 (2014).

24. G. P. Tsironis and N. Lazarides, Appl. Physical Review A, 115, 449 (2014).

25. Y. D. Chong et. al, Phys. Rev. Lett. 105, 053901 (2010).

26. R. Fleury, D. L. Sounas, & A. Al´u, Nat. Commun. 6, 5905 (2015).

27. B. Peng, S. K. Ozdermir, M. Liertzer, W. Chen, J. Kramer, H. Yilmaz, J. Wiersig, S. Rotter, L. Yang, Proc. Natl. Acad. Sci. 113, 6845-6850 (2016).

28. F. J. Shu, C. L. Zou, X. B. Zou, & L. Yang, Phys. Rev. A 94, 013848 (2016).

29. W. Chen, S¸ . K. O¨ zdemir, G. Zhao, J. Wiersig & L. Yang, Nature 548, 192 (2017).

30. H. Hodaei, A. U. Hassan, S. Wittek, H. Garcia-Gracia, R. El-Ganainy, D. N. Christodoulides, M. Khajavikhan, Nature 548, 187-191 (2017).

31. J. Wiersig, Phys. Rev. Lett. 112, 203901 (2014).

32. N. Zhang, S. Liu, K. Y. Wang, Z. Y. Gu, M. Li, N. B. Yi, S. Xiao, & Q. Song, Sci. Rep. 5, 11912 (2015).

33. V. V. Konotop and D. A. Zezyulin. Opt. Lett. 39, 1223 (2014).

34. J. D'Ambroise, B. A. Malomed, and P. G. Kevrekidis. Chaos 24, 023136 (2014).

35. Y. N. Joglekar, R. Marathe, P. Durganandini, and R. Pathak. Physical Review A 90, 040101(R) (2014);

36. Y. Wu, B. Zhu, S.-F. Hu, Z. Zhou, and H. Zhong. Front. Phys. 12, 121102 (2017).

37. D. H. Dunlap and V. M. Kenkre. Physical Review B 34, 3625 (1986).

38. B. V. Chirikov, F.M. Izrailev, and D. L. Shepelyansky, Sov. Sci. Rev. C 2, 209 (1981).

39. G. Della Valle, M. Ornigotti, E. Cianci, V. Foglietti, P. Laporta, and S. Longhi, Physical review letters. 98, 263601 (2007).

40. N. H. Lindner, G. Rafael, and V. Galitski. Nature. Phys. 7, 490 (2011).

41. Y. H. Wang, H. Steinberg, P. Jarillo-Herrero, and N. Gedik. Science 342, 453 (2013).

42. M. Liertzer, Li Ge, A. Cerjan, A. D. Stone, H. E. T¨ureci, and S. Rotter, Physical review letters. 108, 173901 (2012).

43. H. Hodaei, M.-A. Miri, M. Heinrich, D. N. Christodoulides, and M. Khajavikhan. Science 346, 975 (2014).

44. N. Lazarides and G. P. Tsironis, Physical review letters. 110, 053901 (2013).

45. H. Ramezani, Z. Lin, S. Kalish, T. Kottos, V. Kovanis, and I. Vitebskiy, Opt. Express 20, 26200 (2012).

46. Z. P. Liu, J. Zhang, S. K. Özdemir, B. Peng, H. Jing, X. Y. Lü, C. W. Li, L. Yang, F. Nori, and Y.-X. Liu, Phys. Rev. Lett. 117, 110802 (2016).

47. B. Peng, S. K. Ozdemir, S. Rotter, H. Yilmaz, M. Liertzer, F. Monifi, C. M. Bender, F. Nori, and L. Yang. Science 346, 328 (2014).

48. Heiss, W. D. Phases of wave functions and level repulsion. Euro. Phys. J. D 7, 1–4 (1999).

49. Keck, F., Korsch, H. J. & Mossmann, S. J. Phys. A 36, 2125–2137 (2003).

50. Berry, M. V. Physics of nonhermitian degeneracies. Czech. J. Phys. 54, 1039–1047 (2004).

51. H. Xu, D. Mason, Luyao Jiang & J. G. E. Harris. Nature10.1038/18604 (2016).

52. C. Dembowski, B. Dietz, H.-D. Gräf, H. L. Harney, A. Heine, W. D. Heiss, and A. Richter. Physical Review E 69, 056216 (2004).